ADVERTIMENT. L'accés als continguts d'aquesta tesi doctoral i la seva utilització ha de respectar els drets de la persona autora. Pot ser utilitzada per a consulta o estudi personal, així com en activitats o materials d'investigació i docència en els termes establerts a l'art. 32 del Text Refós de la Llei de Propietat Intel·lectual (RDL 1/1996). Per altres utilitzacions es requereix l'autorització prèvia i expressa de la persona autora. En qualsevol cas, en la utilització dels seus continguts caldrà indicar de forma clara el nom i cognoms de la persona autora i el títol de la tesi doctoral. No s'autoritza la seva reproducció o altres formes d'explotació efectuades amb finalitats de lucre ni la seva comunicació pública des d'un lloc aliè al servei TDX. Tampoc s'autoritza la presentació del seu contingut en una finestra o marc aliè a TDX (framing). Aquesta reserva de drets afecta tant als continguts de la tesi com als seus resums i índexs.

ADVERTENCIA. El acceso a los contenidos de esta tesis doctoral y su utilización debe respetar los derechos de la persona autora. Puede ser utilizada para consulta o estudio personal, así como en actividades o materiales de investigación y docencia en los términos establecidos en el art. 32 del Texto Refundido de la Ley de Propiedad Intelectual (RDL 1/1996). Para otros usos se requiere la autorización previa y expresa de la persona autora. En cualquier caso, en la utilización de sus contenidos se deberá indicar de forma clara el nombre y apellidos de la persona autora y el título de la tesis doctoral. No se autoriza su reproducción u otras formas de explotación efectuadas con fines lucrativos ni su comunicación pública desde un sitio ajeno al servicio TDR. Tampoco se autoriza la presentación de su contenido en una ventana o marco ajeno a TDR (framing). Esta reserva de derechos afecta tanto al contenido de la tesis como a sus resúmenes e índices.

WARNING. Access to the contents of this doctoral thesis and its use must respect the rights of the author. It can be used for reference or private study, as well as research and learning activities or materials in the terms established by the 32nd article of the Spanish Consolidated Copyright Act (RDL 1/1996). Express and previous authorization of the author is required for any other uses. In any case, when using its content, full name of the author and title of the thesis must be clearly indicated. Reproduction or other forms of for profit use or public communication from outside TDX service is not allowed. Presentation of its content in a window or frame external to TDX (framing) is not authorized either. These rights affect both the content of the thesis and its abstracts and indexes.

ICFO-INSTITUTE DE CIÈNCIES FOTÒNIQUES

&

UPC-UNIVERSTITAT POLITÈCNICA DE CATALUNYA

Micro - nano structured Electro - Optic devices in $LiNbO_3$ for communication and sensing

DOMENICO TULLI

Thesis Advisor: Valerio Pruneri
Co-Advisor: Davide Janner

PhD Thesis - 2012

Alla mia famiglia

Stay foolish, Stay hungry

Abstract

A material that is enabling integrated optics is the ferroelectric crystal Lithium Niobate ($LiNbO_3$), which has excellent electro-optical, acousto-optical and nonlinear optical properties. Moreover, it can be doped with laser-active ions and allows for simple fabrication of low-loss optical waveguides.

The broad aim of this work is to develop and introduce advanced micro- and nano-fabrication techniques for $LiNbO_3$ and a new class of integrated based telecommunication and sensing devices. The techniques developed include precise micro-domain inversion, etching, bonding and thin film fabrication.

From a device point of view, domain inversion is used to improve the electro-optic response of $LiNbO_3$ waveguide modulators in terms of bandwidth and driving voltage. With respect to standard single-domain structures, larger bandwidths and lower driving voltages can be obtained, thus achieving figure of merits for the electro-optic response that are up to 50% larger. As a demonstration, a chirp-free modulator, having $\sim$2V switching voltage and bandwidth of 15 GHz, was fabricated by placing the waveguide arms of a Mach-Zehnder interferometer in opposite domain oriented regions. The modulator could be driven in a single-drive configuration with inexpensive low-voltage drivers, e.g. a SiGe based RF amplifier, typically used for electro-absorption devices.

A further aspect of this work focuses on the development of devices

for the precise measurement of strong electric fields, which are typically generated in power stations and transmission lines. Therefore, two new integrated electric field sensors are proposed, each of which exploits the aforementioned micro-fabrication techniques. The first device is based on a proton-exchange waveguide at cut-off, centered on a few microns wide domain-inverted region in a z-cut $LiNbO_3$ substrate. The sensor's performance is demonstrated by detecting DC fields up to 2.6 MV/m and high-frequency (1.1 GHz) fields ranging from 19 V/m to 23 kV/m. The second proposed device is fabricated by direct bonding a z-cut $LiNbO_3$ substrate on top of a cut-off proton-exchanged waveguide centered on the domain-inverted region. It is possible to detect electric fields as high as 2 MV/m at low frequency with improved sensitivity compared to the previous device. These features make the devices suitable for use in high electric field and harsh conditions without endangering the operator.

The conclusions section of the Thesis presents possible future developments which will contribute to increase the impact of the work in the optical telecommunication and sensing industries.

Resumen

Uno de los materiales que permite el avance de la tecnología de dispositivos ópticos integrados es el niobato de litio ($LiNbO_3$). Se trata de un cristal ferro-eléctrico, con excelentes propiedades electro-ópticas, acusto-ópticas y no lineales. Además, es posible fabricar guías de onda de bajas pérdidas mediante las técnicas de intercambio protónico (PE) y difusión de titanio.

El objetivo principal de este trabajo es el desarrollo y la introducción tanto de las técnicas avanzadas de micro-nano fabricación para el niobato de litio como de nuevos dispositivos ópticos integrados para las comunicaciones ópticas y la detección de campo eléctricos de alto voltaje. La técnicas de fabricación desarrolladas incluyen inversión de dominios mediante la técnica de poling de alto voltaje, grabado, bonding y capas delgadas.

Desde el punto de vista de los dispositivos, la inversión de dominios ha sido utilizada para mejorar la respuesta electro-óptica de los moduladores en $LiNbO_3$ en términos de ancho de banda (BW) y voltaje de control (V_π). En comparación con los moduladores comerciales actuales de un único dominio, con esta técnica es posible obtener mayores anchos de banda y menores voltajes de control resultando en un aumento del 50% del producto BW/V_π. Para demonstrar la eficacia de la técnica desarrollada, se ha fabricado un modulador Mach-Zehnder chirp-free poniendo los brazos del interferómetro en dos regiones de dominios opuestos. De las mediciones efectuadas se han obtenidos valores de voltaje de control de 2V y ancho de banda de 15 GHz. Estos resultados muestran que los dispostivos desarrollados pueden reducir el coste total de funcionamiento,

ya que permiten el uso de controladores económicos de Si-Ge que operan en el rango de los 2V.

Otro aspecto de este trabajo se enfoca en el desarrollo de dispositivos para medir, de forma exacta, altos campos eléctricos, que normalmente son generados en las centrales eléctricas y en las líneas de transmisión. Por este motivo, se han desarrollado dos sensores de campo eléctrico mediante las técnicas de micro-fabricación anteriormente mencionadas. El primer dispositivo está basado en una guía fabricada mediante intercambio protónico en $LiNbO_3$ *z*-cut, diseñada a la frecuencia de corte y centrada en una región de dominio invertido de 10 micras de ancho y 10mm de largo. El rendimiento del dispositivo se ha demostrado detectando campos a baja frecuencia con amplitudes de hasta 2.6MV/m y campos a la frecuencia de 1.1GHz con amplitudes desde 19V/m hasta 23kV/m. El segundo dispositivo se ha fabricado mediante bonding directo de un sustrato de $LiNbO_3$ encima de una guía PE diseñada a la frecuencia de corte y centrada en una región de dominio invertido de 10 micras de ancho y 10 mm de largo. El dispositivo se ha caracterizado a baja frecuencia y ha sido posible medir campos eléctricos de hasta 2MV/m con un aumento de sensibilidad comparado con el primer dispositivo fabricado sin la técnica del bonding. Estos resultados muestran que los dispositivos desarrollados pueden ser utilizados para mediciones de campos eléctricos intensos en condiciones peligrosas sin ningún riesgo para el operador.

Después de una breve introducción en el Capítulo 1 de esta Tesis, las propiedades del $LiNbO_3$ se discuten en el Capítulo 2, prestando especial atención a sus características ópticas y electro-ópticas. El Capítulo 3 presenta las técnicas de micro fabricación desarrolladas durante este trabajo sobre sustratos de 3 pulgadas. En particular, se presentan las técnicas de fabricación de guías mediante intercambio protónico, de inversión de dominios mediante poling de alto voltaje, de bonding de $LiNbO_3$ con diferentes sustratos ($LiNbO_3$, SiO_2, Si) y la fabricación de capas delgadas. El Capítulo 4 ofrece una introducción sobre los moduladores interferométricos Mach-Zehnder de onda propagada, presentando sus principales características. Además se presenta una nueva estructura de modulador basada sobre inversión de dominios y los resultados obtenidos. El

Capítulo 5 empieza con una introducción sobre los sensores de campo eléctrico y después se presentan dos nuevos sensores de campo eléctrico completamente ópticos fabricados en $LiNbO_3$ *z*-cut. Los dispositivos están basados en las técnicas de intercambio protónico, inversión de dominios y bonding directo. Finalmente, en el Capítulo 6 se presentan las conclusiones y posibles desarrollos futuros que pueden contribuir al aumento del impacto de este trabajo en las industrias de comunicaciones ópticas y de detección.

Acknowledgemnts

I would not have been able to complete this thesis without the support of numerous individuals.
First of all, I would like to thank my supervisor Prof. Valerio Pruneri, who gave me the opportunity to start my PhD and also for his confidence, his help and ideas, and for the support throughout this work.
I would also like to thank Dr. Davide Janner, for his help, the continuous support and the long discussions.
I wish to thank my colleagues and friends that I met during these last five years at ICFO, and who shared with me the time in the labs and clean rooms, many discussions, lunches and dinners: Marc, Daniel, Didit, Vittoria, Miguel, Sarah, Drithi, Albert, Nadia, Fabian, Carme, Arnaud, Robert.
I want also to thank the people from the mechanical workshop: Xavi, Juan, Jose and those from the documentation department: Ferran, Tania and Sergio. A special thank to my friends for their constant support and for all the happy times spent together: Andrea, Alberto, Laura, Mark, el ”Equipo Moorea” and my karate group.
Finally, I wish to thank my family, especially my parents, my sister and my grandmother for believing in me from the beginning, for their help, their support and for loving me no matter what.
Thank you all for making this possible.

Contents

List of Figures

List of Tables

Chapter 1

Introduction

This thesis is devoted to the design and fabrication of a new class of lithium niobate devices for optical communication and sensing.

1.1 Optical communication and sensing markets in brief

Optical communication market

In the past few years, the need for high-speed end-to-end communications is the principal factor driving photonics research forward. The global demand for bandwidth has been nearly doubling every year (Fig. 1.1). Several new applications are responsible for this remarkable growth in data transport, including video sharing sites, movie downloads, online gaming, streamed television, etc. The recent introduction of ”cloud computing” - delivering online computing services through remote data centers over Internet - or network-based operating systems, such as Gloogle Chrome OS, are examples of how innovation keeps increasing the data flowing across the globe.

These new bandwidth-hungry applications present the research community with new technological challenges. Even if the actual data trans-

port is performed optically, the switching logic is still implemented electronically. To compensate the high-speed data transmission, it is necessary to break streams of bits into lower speed electronic data-paths, working in parallel. This corresponds to an increase of power consumption and consequently to an increase of costs and emissions from electricity generation. It is thus essential to increase the spectral efficiency (bit/s/Hz) and the energy efficiency (bit/s/mW) of devices used in the optical communication systems. There is also an overall trend toward higher levels of integration and more functionality on a single chip, so that power consumption, size and cost can be decreased.

1.1.1 Optical sensing market

Market analysis indicates that optical sensing plays a critical role in niche applications such as industrial (e.g. temperature, current/voltage), energy and defense (e.g. gyro and acoustic sensors) as well as security, structural health monitoring and civil (Fig. 1.2). To take advantage of their

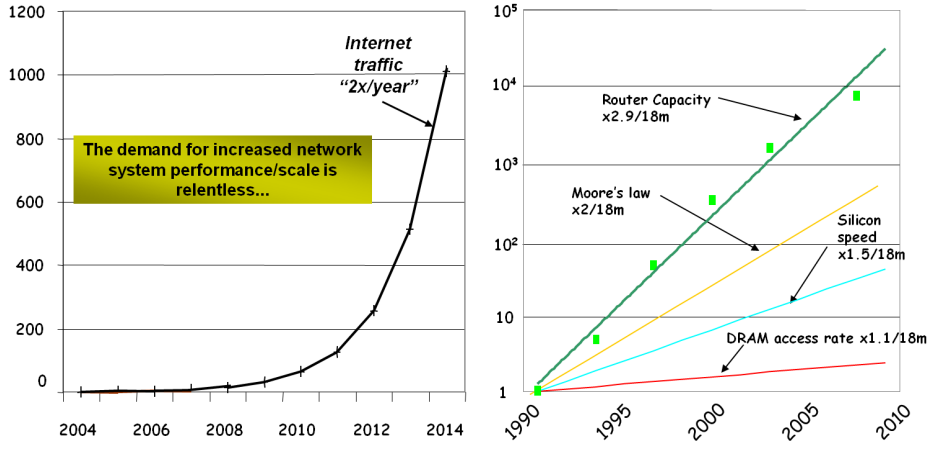

Figure 1.1: Router capacity nearly doubles every year. This rate of growth is greater than the rate of increase of components on a chip according to Moore's law [1].

overwhelming qualities and ensure widespread and commercial adoption, companies need to lower their sensor system costs which include the sensing elements, packaging, cabling and interrogation systems.

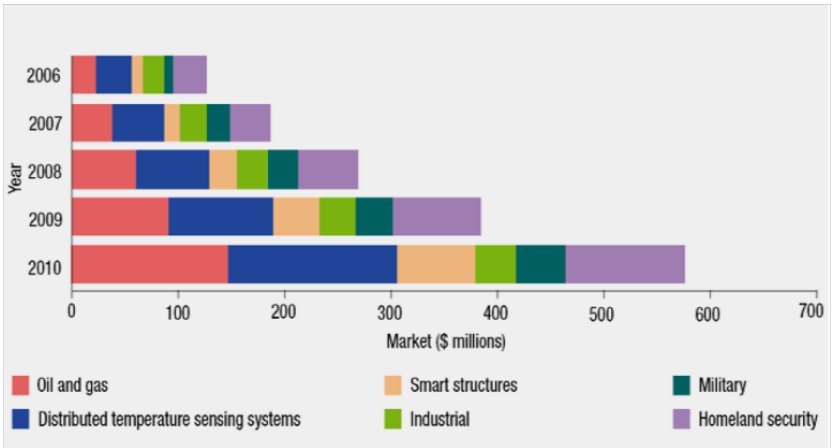

Figure 1.2: Optical Sensor Market [2].

It is clear that in this scenario the challenge for the next decade is not only to improve what are already high-quality and low-cost components, but above all develop fabrication techniques that will boost integration processes with respect to speed, power consumption and the number of basic building blocks it can support.

1.2 Integrated optics and micro-nano-structuring of $LiNbO_3$

The concept of integrated optics was first introduced in the late 1960's. It refers to the fabrication and integration of several components on a common planar substrate. These components include sources, detector, beam splitters, grating, couplers, polarizers, interferometers, among others. Consequently, these elements can be used as building blocks to fabricate more complex planar devices, which can perform a wide range of

applications in optical communications, instrumentation and sensing - in much the same way the electrical circuits form the backbone of integrated electronics Fig. 1.3. The integrated photonic technology can be considered as the confluence of several photonic fields (dealing with the control of light by electrons and vice versa) with waveguide technology. In fact, optical waveguides are the key element of integrated photonic devices that perform not only guiding, but also coupling, switching, splitting, multiplexing and demultiplexing of optical signals.

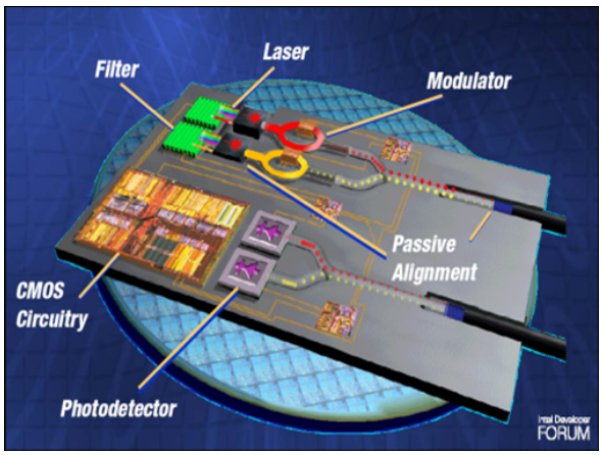

Figure 1.3: Integrated Optics as the result of the junction of various photonic disciplines and waveguide technology [3].

In the world of integrated optics for communications and sensing, different materials are used. Dielectric materials such as silicon oxide (SiO_2), glass or polymers can be used to fabricate waveguides and passive devices. Semiconductor compounds, such as GaAs, InP and Si, are used in active devices, like lasers, modulators or detectors. But there is also an important group of applications based on dielectric crystals: waveguides, electro-optical devices, acousto-optical devices, or even waveguide lasers and nonlinear frequency converters. Among them, the ferroelectric Lithium Niobate ($LiNbO_3$) crystal continues to be one of the premier materials for integrated optics. This is due to its wide availability in high

quality crystal wafers of several inches, relatively low manufacturing cost, low losses, good stability and its excellent electro-optical, acousto-optical and nonlinear properties. Moreover, mature technologies for the fabrication of optical waveguides in the material exist, namely titanium indiffusion and proton exchange. Being a ferroelectric crystal, $LiNbO_3$ can be micro-nano-engineered using electric field poling techniques, such as electric field poling, thin film polishing, bonding and etching [4, 5]. In that way unprecedented properties can be induced in the crystal structure, thus offering the possibility of innovative photonic device designs.

1.3 Aims of the thesis

In the telecommunications market $LiNbO_3$ is the material of choice for electro-optical modulators. These devices can transform the electrically generated data into light pulses, which can be sent into the optical network. Existing commercial $LiNbO_3$ modulators typically reach bandwidths of 10 to 40 GHz and use a driving voltage in the range of 4 to 6 V. Nevertheless, they can be further developed to enhance the performance of optical networks in terms of bandwidth, minimization of power consumption and price of the driving equipment. Therefore, modulators with very low driving voltages would allow using inexpensive control electronics, thus making them suitable for operation in future access networks - e.g. fiber to the home (FTTH). In addition, another challenge is to design and develop more complex structures based on cascaded interferometers that allow an increase in the spectral efficiency by using transmission techniques based on new modulation formats, utilizing not only amplitude modulation but also phase modulation schemes.

Optical current and voltage measurements are attractive alternatives to electronics counterparts especially in hazardous and harsh environments, for example the high voltage lines and transformers for electrical energy transport. An optical approach presents intrinsic advantages, such as electromagnetic interference immunity, feasibility of electrode-free operation

in an environment where there is a high probability of electrical breakdown. Several electro-optic crystals, such as bismuth germanium oxide (BGO), bismuth silicon oxide (BSO), lithium niobate ($LiNbO_3$), lithium tantalate ($LiTaO_3$) and potassium dihydrogen phosphate (KDP) have been used to this end. However there is a need to improve the performance (sensitivity, dynamic range and/or linearity) and integration or cost.

- The first task of this work is the development of advanced micro and nano fabrication techniques to realize a new class of integrated $LiNbO_3$ devices. To this end, a big effort is put into the development of electric field poling technique where the control of domain formation and spreading is essential for efficient non linear interaction in waveguides. A new proton exchange set-up for low-loss optical waveguide formation over a 3" substrate is presented. Moreover, a novel method for room temperature-bonding $LiNbO_3$ with different material substrate (e.g. Si, SiO_2) is established. Likewise, precise lapping and polishing techniques are developed. These techniques lead us to fabricate a bonded structure where the $LiNbO_3$ thickness is of the order of 10 μm.

- The second objective of the thesis is to use the advanced micro-nano-fabrication techniques developed to make new integrated electro-optic modulator designs possible in $LiNbO_3$, which are able to increase the performance significantly, in particular very low driving voltages and large bandwidths. Several experiments were carried out in collaboration with Avanex Corporation, now Oclaro Inc, which is a world leading supplier of integrated electro-optic modulators for the telecommunication industry.

- Another aim of the thesis is to introduce a new design of micro-nano-structured $LiNbO_3$ waveguides for electric field and voltage measurements not requiring the use of metallic electrodes. The work presented in the second part of this thesis was driven by a proposed application of measuring high electric fields generated in power plants and/or transmission lines. The group is collaborating

with ABB, a major supplier of current and voltage sensors solutions.

1.4 Thesis Outline

The **second chapter** describes the basic properties of the material used in the thesis work: Lithium Niobate ($LiNbO_3$). This includes the properties related to its ferroelectric crystal structure and the subsequent applications. **Chapter three** presents the micro-fabrication techniques, over 3 inch $LiNbO_3$ wafers, developed at ICFO during this work. The chapter begins with a description of waveguides fabrication by Annealed Proton Exchange (APE). The mid-part of the chapter outlines the fabrication procedure for domain inversion using electric field poling technique and liquid electrodes while the last part describes the bonding technique to permanently join $LiNbO_3$ with different substrates, namely Si, SiO_2 and another $LiNbO_3$. Moreover, lapping and polishing techniques for thin plate fabrication are presented. The **forth chapter** firstly introduces the fundamentals and main characteristics of travelling-wave $LiNbO_3$ Mach-Zehnder modulators. Secondly, a new modulator design is proposed. It is based on domain inverted $LiNbO_3$, with improved performance with respect to existing devices. The modulator characterization and the results obtained from the new design are presented. The **chapter five** begins with a literature review about DC and low frequency electric field optical sensors. Afterwards, two novel all-optical electric field sensors are presented. Both devices are based on a proton-exchange, domain inversion and bonding techniques. The sensors characterization, including the test set-up and the performance results are discussed. Finally, in **chapter six**, several conclusions on the thesis work and possible future work directions are presented.

Chapter 2

Lithium Niobate

2.1 Overview

Lithium Niobate ($LiNbO_3$) is one of the most popular materials used in Integrated Optics and it is the material of choice for the work contained in this Thesis. It is an artificial material which was first synthesized in 1949 [6], which has an attractive combination of properties. It exhibits enhanced surface acoustic capabilities, low optical propagation losses at the telecommunication wavelengths, high non linear optical coefficients, which allow efficient frequency conversion, and high electro-optical coefficients allowing fabrication of Mach-Zender modulators, electric field sensors and other integrated optical circuits. For these reasons around 80 tons of $LiNbO_3$ are produced every year, of which about 80% is used in the industry of acoustics and the rest is mainly used in optics [7]. The main properties of $LiNbO_3$ are presented in the following sections, with particular focus on those exploited in the present thesis work.

2.2 Growth of Lithium Niobate

The most common way for industrial growth of $LiNbO_3$ crystals is the Czochralski technique (Fig. 2.1a) in which a monocrystaline seed is im-

mersed into a crucible containing a melt of lithium and niobium oxides (Li_2O and Nb_2O_5). The seed is stirred and removed slowly from the melt and the material solidifies, due to the cooling, on the seed following its original crystal structure. The molten Li_2O:Nb_2O_5 system has the phase diagram shown in Fig. 2.1b. In the diagram, there is a region in which a unique phase of $LiNbO_3$ exists ranging from a Li_2O poor area (temperature dependent) to a Li_2O rich area near the stoichiometric composition. For this reason, $LiNbO_3$ is not completely described by its chemical formula but it depends on the fabrication parameters. Then, it is possible to find two main types of $LiNbO_3$: stoichiometric, which is represented by its chemical formula; and congruent, which grows in the same composition as the melt, containing 48.45% mol Li_2O and51.55% mol Nb_2O_5. In the fabrication of waveguides by proton exchange or Ti in-diffusion, the congruent constitution is widely used.

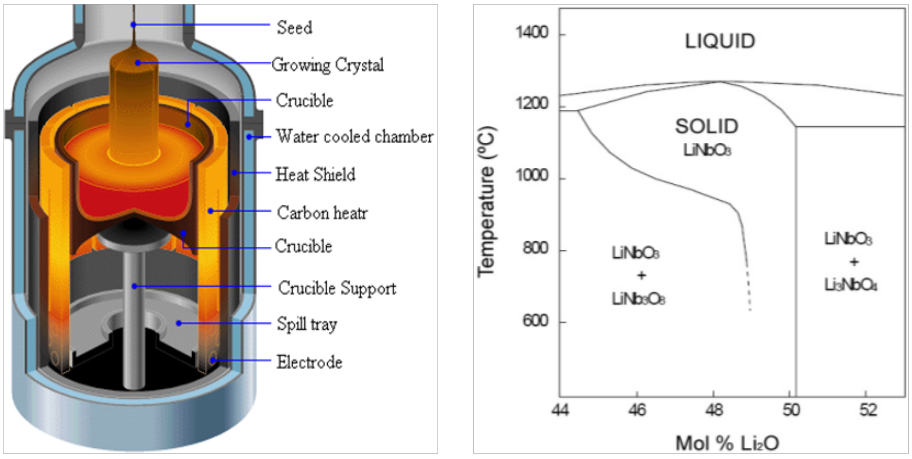

a) b)

Figure 2.1: (a) Schematic of a Czochralski crystal grow system, (b) Phase diagram of the Li_2O: Nb_2O_5 used to fabricate the $LiNbO_3$.

2.3 Crystal Structure

$LiNbO_3$ has a trigonal structure, given by three-fold rotation symmetry about its c axis and belongs to the point group $3\overline{m}$, as it shows mirror symmetry about three planes that are 60° apart from each other. The atomic arrangement within the stoichiometric hexagonal unit cell, as it is shown in Fig. 2.2a, consists of six formula weights with Li and Nb ions located on the polar c-axis (crystal axis also indicated with z) and the O atoms in general positions. Li occupies oxygen atom octahedra that shares faces with adjacent similar octahedra on either side along the trigonal axis. One of those octahedra is empty and the other one is occupied by Nb. The triple octahedron is repeated, with alternating sequences having identical orientation, along the polar axis. The spacing between corresponding atoms in alternate sequences forms the c-axis repeat [7]. At room temperature the Nb ion is shifted 0.28 Å with relation to its octahedron center and the Li ion is 0.67 Å shifted from its central position. This shifting, in the same direction for both atoms, is responsible for the dipoles which produce the macroscopic spontaneous polarization $\overrightarrow{P_s}$ of $LiNbO_3$. There are two equilibrium configurations for these shifted ions: either above or below the octahedron center, which determines the polarization direction. If this orientation is removed, the polarization disappears and the crystal becomes paraelectric.

This happens above the Curie temperature which is, approximately, 1142°C [9]. In a similar way, the inversion of the atom displacements produces the inversion of the spontaneous polarization (Fig. 2.2b). The physical tensor properties are described by Cartesian *x,y,z* coordinate system. The convention that relates these coordinates to the hexagonal axis is that the *z*-axis is chosen to be parallel to the *c*-axis. The *x*-axis is chosen to coincide with any of the equivalent *a*-axes. The *y*-axes is then chosen so that a right-handed system is specified, therefore it must lie in a plane of mirror symmetry. The standard method of determining the direction of the *c*-axis is to apply strain along the crystal the *c*-axis direction. The $+c$-axis is defined as being directed out of the *c* face that becomes negative upon compression. In a similar way, the direction of the *y* axis is

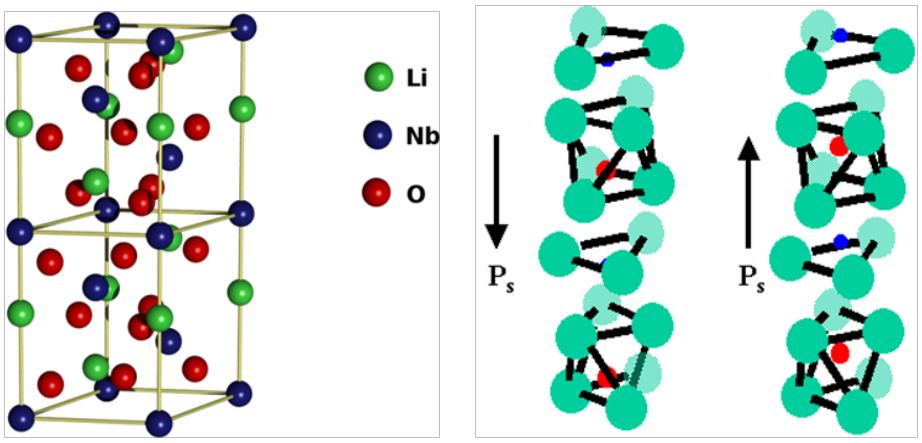

a) b)

Figure 2.2: (a) $LiNbO_3$ unit cell, (b) Ferroelectric state of $LiNbO_3$ [8], where the position on the atoms of Li (red) and Nb (blue) are shown with respect to the oxygen (green) planes. The resulting spontaneous polarization $\overrightarrow{P_s}$ is also indicated.

determined. Upon compression the $+y$ face becomes negatively charged. The sense of the x direction, however, cannot be determined in this way because it is perpendicular to a mirror plane. Any charge movement on one side of the plane is ”mirrored” on the opposite side, hence the x faces do not become charged. This is important when working with $LiNbO_3$ as the z-cut samples (whose surface is perpendicular to the z axis) show a spontaneous charge and frequently attract dust and light particles. With x-cut samples, though, this effect does not occur and there is limited surface charge.

2.4 Ferroelectricity, pyroelectricity and piezoelectricity

As it was previously mentioned, the ferroelectric behavior of $LiNbO_3$ depends on the crystal structure. This means that the material exhibits an inherent electrical polarization without any external field being applied. This polarization can be not homogeneous, and the material can display different states of polarization in different regions. Each one of these regions of uniform polarization is called ferroelectric domain. To obtain single domain crystal, the so-called poling process is used. It consists on the application of an electric field (E) greater than a certain threshold (coercive field E_c) across the crystal. This has the effect of forcing the polarization into the direction of the applied electric field and therefore forcing the crystal into a single domain structure. Typical values of P and E_c for $LiNbO_3$ at room temperature are of the order $\sim 0.72\mu Cmm^{-2}$ and $\sim 21kVmm^{-1}$ respectively. $LiNbO_3$ also belongs to a group of crystals that include ferroelectrics. These materials are called pyroelectrics and they exhibit a change in the spontaneous polarization as a function of temperature. The relationship between the change in temperature, ΔT, and the change in spontaneous polarization, $\Delta \overrightarrow{P}$, is linear and can be written as shown in equation 2.1 where p is the pyroelectric tensor. This effect is due to the movement of the lithium and niobium ions relative to the oxygen layers.

$$\Delta P_i = p_i \Delta T \qquad p = \begin{pmatrix} 0 \\ 0 \\ p_3 \end{pmatrix} \tag{2.1}$$

Since this movement is only along the direction parallel to the c axis, the tensor p has only one non-zero component. Moreover, pyroelectric solids also belong to the larger group of the piezoelectric materials. A piezoelectric solid exhibits an induced polarization with applied stress. The relationship between polarization and stress is also linear and may be written as function of the applied stress tensor *d* and the piezoelectric tensor d as in equation 2.2, where *i, j, k* can be the coordinates *x, y, z*.

$$P_i = \sum_{j,k} d_{j,k}\sigma_{j,k} \qquad i,j,k = 1,2,3 \tag{2.2}$$

All tensors describing the physical properties of a crystalline material must have, at least, the same symmetry as the material. This usually helps to reduce the number of different terms in the tensors. In particular, the piezoelectric tensor in $LiNbO_3$ has only four independent coefficients.

2.5 Optical Properties

From the optical point of view, $LiNbO_3$ is an anisotropic uniaxial crystal. The relation between the electric displacement field $\overrightarrow{D}$ and the applied electric field $\overrightarrow{E}$ is expressed as shown in equation 2.3.

$$D_i = \varepsilon_0 \sum_j (\varepsilon_r)_{ij} E_j \qquad i,j = x,y,z \tag{2.3}$$

Due to the crystal symmetries the relative permittivity dielectric tensor $\overline{\overline{\varepsilon}}$ written with respect to a Cartesian frame presents non zero terms only on the main diagonal and two of them are equal:

$$\overline{\overline{\varepsilon}} = \varepsilon_0 \begin{bmatrix} \varepsilon_{11} & 0 & 0 \\ 0 & \varepsilon_{22} & 0 \\ 0 & 0 & \varepsilon_{33} \end{bmatrix} \tag{2.4}$$

with

$$n_o^2 = \varepsilon_{11} = \varepsilon_{22} \qquad n_e^2 = \varepsilon_{33} \tag{2.5}$$

There are two main ways to measure the dielectric constant of a material. On the one hand, we have the free (unclamped), measurement in which the stress of the crystal is zero. In this case, low electrical frequencies are used, below the mechanical resonance frequency, as the strain can follow the oscillation of the electric field. This is usually measured in the range of 100 kHz. On the other hand, we find the clamped measurement, for which the strain is zero. In terms of electric field, this happens

if the frequency is above the resonance and the structure cannot follow the electric field oscillation. This is the interesting range if we consider microwave applications. When optical frequencies are taken into account, the permittivity tensor has the same structure although, in this case, the most used physical magnitude is the refractive index.

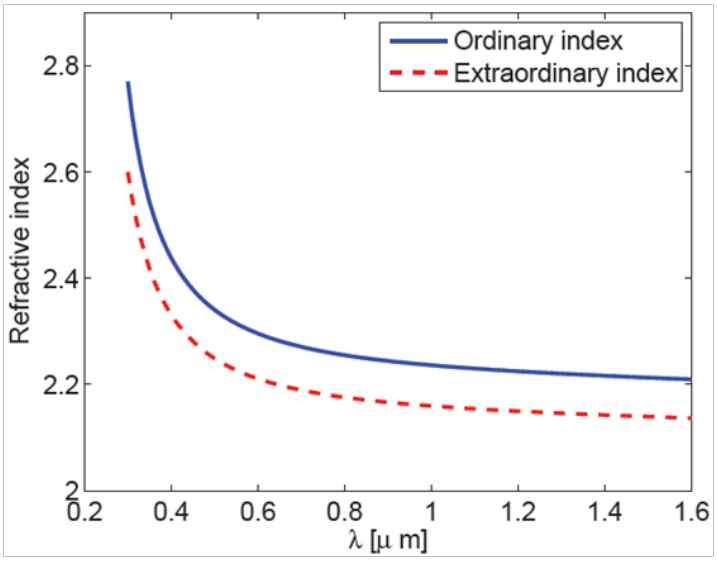

Figure 2.3: Extraordinary and ordinary refractive index of the $LiNbO_3$ crystal as a function of the wavelength for T = 25°C.

Nevertheless, the refractive index for the microwaves (GHz range) and for the optical frequencies (100 THz range) obviously differs due to the material dispersion. For optical waves propagating through the medium, the refractive index to be used is given by the polarization of the optical field. In that case, the light polarized in the direction of the c axis (called for this case optical axis) shows a different refractive index than the light polarized in the directions perpendicular to the c axis. These refractive indices are called, respectively, extraordinary (ne) and ordinary (no) indices. The birefringence of the material is defined as $n_e - n_o$ and for the $LiNbO_3$ it takes a negative value, as the ordinary index is larger than the

extraordinary index. The extraordinary and ordinary refractive indices of the $LiNbO_3$ massive crystals are well approximated, in their wavelength (chromatic dispersion) and temperature dependencies, by the Sellmeier relations [10]. The extraordinary and ordinary indices are plotted in Fig. 2.3 as a function of the wavelength for T = 25°C in the interval of interest.

2.6 Linear Electro-optic effect

The integrated optical devices studied in this thesis exploit the Pockel's effect. In non-centrosymmetric crystals, such $LiNbO_3$, the refractive index varies linearly with the applied electric field, with the constant of proportionality depending on the orientation of the electric field with respect to the crystallographic axes. The resulting change in the optical path length of the light passing through the crystal is proportional to the voltage applied to a set of electrodes. Over a fixed physical length of crystal, this converts to a phase shift of the light passing through it, which can be converted into intensity modulation in a Mach-Zehnder interferometer. A convenient way to visualize the electro-optic effect is to use the index ellipsoid of the crystal [11]. The linear change in the coefficients of the index ellipsoid due to an applied electric field E_j along the principal crystal axis is [12]:

$$\Delta\left(\frac{1}{n_i^2}\right) = \sum_{j=1}^{3} r_{ij}E_j, \tag{2.6}$$

or

$$(\Delta n)_i = -\frac{n^3}{2}\sum_{j=1}^{3} r_{ij}E_j \tag{2.7}$$

where $i = 1, 2, \cdots 6$ and r_{ij} is the 6×3 electro-optic tensor. By inserting the electro-optic tensor r_{ij}, the six values of Δn can be written as the elements of a symmetric 3×3 matrix. Due to the symmetry of $LiNbO_3$ only four of the eighteen coefficients of r_{ij} tensor are independent. These

coefficients are: $r_{13} = 8.6pm/V$; $r_{22} = 3.4pm/V$, $r_{33} = 30.8pm/V$, $r_{51} = 21.8pm/V$. Therefore we have:

$$\Delta n_{ij} = -\frac{n^3}{2}\begin{pmatrix} -r_{22}E_y + r_{13}E_z & -r_{22}E_x & r_{51}E_x \\ -r_{22}E_x & r_{22}E_y + r_{13}E_z & r_{51}E_y \\ r_{51}E_x & r_{51}E_y & r_{33}E_z \end{pmatrix} \tag{2.8}$$

where n is either the ordinary (n_o) or extraordinary (n_e) value. An applied electric field along the crystallographic *x, y* and *z* axes produces an index change and, therefore, a phase change for an incident optical field polarized along such axis through the diagonal elements of the matrix. Using equation 2.8 we can finally obtain the relations:

$$\Delta n_e = \Delta n_{33} - \frac{n^3}{2} r_{33} E_z \tag{2.9}$$

$$\Delta n_o = \Delta n_{11} = \Delta n_{22} = -\frac{n^3}{2} r_{13} E_z \tag{2.10}$$

The off-diagonal elements of matrix 2.8, on the other hand, represent electro-optically induced conversion or mixing between orthogonal polarization components.

Since r_{33} is the largest EO coefficient, it is desirable to exploit it for EO modulation and sensing. This means that the electric field is applied along the *z*-direction. The electrode configuration needed to generate E_z depends on the orientation of the crystal cut. For *x*-cut $LiNbO_3$ crystal, an electric field along the *z*-direction means a horizontal electric field. The electrode configuration is shown in Fig. 2.4a. In this case the optical waveguide has to be along the *y*-axis (because the *x*-axis is vertical to the sample surface, and the *z*-axis is the direction of the electric field) and the TE optical mode is much more efficiently modulated than the TM optical mode, as the $r_{33} >> r_{13}$. If *z*-cut $LiNbO_3$ is chosen, electrodes are placed on top of the waveguide and the optical mode must be TM (Fig. 2.4b).

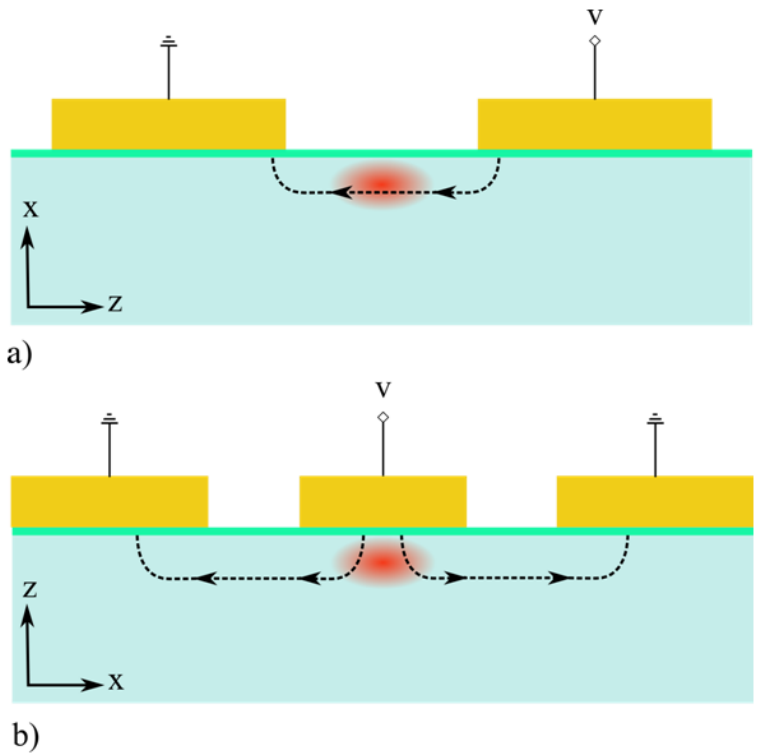

Figure 2.4: Electrode configurations for optical phase modulation with (a) *x*-cut and (b) *z*-cut crystals.

2.7 Optical waveguides fabrication in $LiNbO_3$

Optical waveguide devices based upon $LiNbO_3$ substrates are presently in an advanced state. A large variety of devices have shown improved performance as, for example, external modulators in long-distance high bit-rate systems. Nowadays, the technology for $LiNbO_3$ devices is well developed, leading to fabricate "good" waveguides in order to achieve satisfactory overall device performance with respect to loss, driving voltage and modulation bandwidth. Many techniques have been used to form waveguides in $LiNbO_3$. Initially waveguides were formed by thermal outdiffusion of Li_2O which results in an increased extraordinary refractive

index [13]. In-diffusion of a dopant - almost exclusively titanium - is generally preferred to raise the refractive index [14] and it is the most common technique used for general device development. Ti has been proven to be a specially attractive dopant for several reasons such as (a) the possibility to be patterned into any desired two dimensional geometries using standard photolithography, (b) the formation of high and nearly equal index change for both polarizations, (c) the negligible absorption in IR, visible or near IR and (d) the possibility to fabricate waveguides in relative modest diffusion time and temperature (typically 1000 °C, 6-9 h). More recently, proton exchange using benzoic acid [15] and other acids has become popular to make waveguides. This is an ion-exchange process where lithium ions in $LiNbO_3$ are substituted by protons H+, from appropriate melt of solution. The main difference between waveguides fabricated through proton exchange and those fabricated through titanium in-diffusion is that the former only guide light of extraordinary polarization, whereas the latter guide both polarizations. Further, proton exchange guides are less susceptible to optical damage [16] and it is possible to fabricate waveguide at much lower temperature (typically 200°C - 250°C) compared to Ti-diffusion process [17]. Due to these advantages and to its easy implementation we have chosen proton exchange as waveguide fabrication method. When we have needed Ti in-difussed waveguides for specific applications, we have found suppliers, for example through external collaborations, such as that with Avanex Corporation (now Oclaro Inc.).

Chapter 3

Micro-engineering fabrication techniques

In this chapter, the micro-structuring techniques developed at ICFO and employed to realize the new device configurations are presented.

3.1 Annealed Proton Exchange (APE)

The proton exchange (PE) process involves basically a chemical reaction between the substrate and the proton source at temperatures in the range from 150°C to 249°C [18]. It consists in the replacement of lithium ions (Li^+) from the crystal surface with protons (H^+), which are in the source. The two factors affecting the proton-exchange process are the temperature of the melt and the availability of protons for exchange in the melt. A variety of compounds can be used as proton source and the main requirement is an equilibrium in which a significant concentration of solvated protons is present in the exchange medium [19]. The chemical reaction can be represented as [20]:

$$LiNbO_3 + xH^+ \rightarrow H_xLi_{1-x}NbO_3 + xLi^+ \tag{3.1}$$

where *x* represents the normalized proton concentration. The strains

induced by this substitution can substantially modify the crystal structure of the substrate surface [21] leading to an increment of the extraordinary refractive index ($\sim$0.12 at 633 nm) and a decrement of the ordinary index ($\sim$ 0.04) relative to the values of $LiNbO_3$ substrate; consequently, only TM guided mode exist in *z*-cut substrates, and TE mode in *x*-cut and *y*-cut substrates. The proton source chosen in this work consists of benzoic acid (C_6H_5COOH) buffered with 1% of Lithium Benzoate (LB) [22]. The reasons for using benzoic acid are: (a) the convenient working range (melting point =122 °C, boiling point = 249 °C), (b) the low toxicity, (c) it is relatively easy to handle at room temperature and in its molten state, and (d) it is inexpensive. Fabrication of guides in pure benzoic acid is not convenient because the effective indices are unstable, the propagation losses are high and the electro-optic characteristics are degraded [18]. The proton exchange can be modeled by an inter-diffusion process of ions represented by a nonlinear diffusion equation [23]. To overcome the problems due to the proton exchange, a subsequent thermal annealing is added [24, 25]. This step leads to diffusion broadening of the hydrogen-enriched layer towards the substrate bulk. At the same time the material undergoes to a structural phase transitions as a result of the reduction in local ion concentration (Fig. 3.1) [26, 27]. The fabricated Annealed Proton Exchange (APE) waveguides present low-losses, good stability and restored EO coefficient. Preliminary detailed studies on the formation of APE waveguides concern planar waveguides and examine the refractive index profiles and proton concentration in the waveguide layer. The reasons to start this work, by studying planar waveguides, are simple and practical. A planar waveguide has a one-dimensional (1D) cross-sectional structure, which can be easily analyzed through theoretical models. This allows for accurately evaluating the index profile and the thickness.

Moreover, prism coupling technique for index profile measurements is a well established technique and it does not require any cut or lapping of the sample's end-faces. However, in practical applications the use of channel waveguides is required. Therefore, theoretical analysis requires precise 2-D modelling and optimization of the fabrication process is key

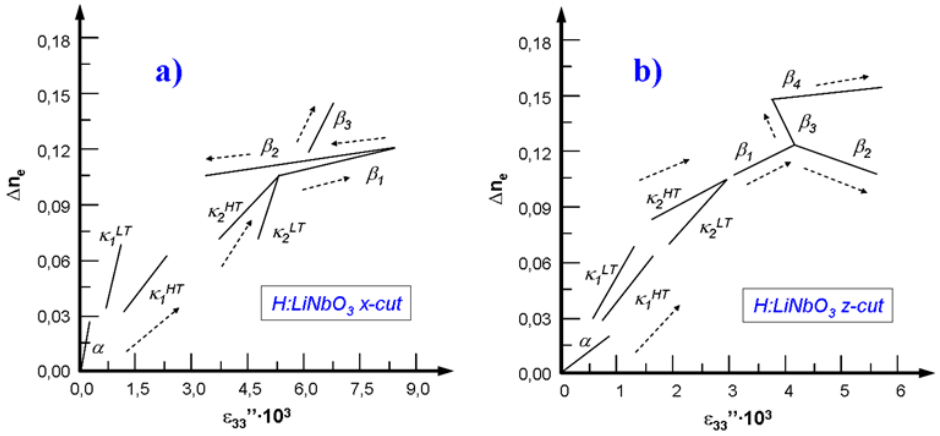

Figure 3.1: Structural phase diagrams of $H_xLi_{1-x}NbO_3$ on z-cut (a) and x-cut (b) substrates [28]. They give the dependence of the extraordinary index variation Δn_e measured at $\lambda = 633nm$ versus the surface value of deformation ε_3'' normal to surface plane. The arrows show the directions in which proton concentration increases.

fundamental for high performances of integrated devices [29, 30].

3.1.1 Fabrication Procedure

The substrates used in the experiments are double polished z-cut $LiNbO_3$ of dimensions ranging from 1 to 3 inches. The samples are thoroughly cleaned by immersing them in a series of electronic-grade solvents placed in an ultrasonic bath for at least 15 minutes. The apparatus used to fabricate PE $LiNbO_3$ waveguides is shown in Fig.3.2. It consists of a thermal reactor with a temperature control of 0.5°C accuracy. The benzoic acid powder compound is put into an iron container while the cleaned $LiNbO_3$ substrate is placed in a holder and kept distant from the proton source. Thereafter, the container is tightly sealed to avoid any unwanted reaction during the process between the acid and the air. In order to heat and maintain the temperature of the molten acid as stable and homogeneous as

possible, the thermal reactor is filled with silicon oil and the iron container is subsequently partially immersed in the oil bath. The thermal reactor is then covered to provide a well isolated, temperature stable environment. In the implemented system it is possible to measure both the oil and the acid temperature; a systematic difference of 5°C has been verified. The values indicated in this work for the fabrication temperature are those of the acid temperature. The benzoic acid is heated at a specific temperature (200-220°C) for 2 hours, in order to reach thermal equilibrium. Moreover, in order to guarantee fresh and homogeneous proton source, the molten mixture is magnetic stirred. Therefore, the substrate is slowly put into the molten mixture to prevent thermal shock. After 5 minutes the substrate is completely immersed in the solution. The exchange time is measured from the time the sample gets in contact with the proton source. When the desire exchange time (10 -75 min) is reached, the sample is slowly removed from the acid and let it to cool down to room temperature inside the iron container to avoid any possible thermal shock. To maintain the acid purity, each load of acid is used to fabricate only two samples [31]. The substrate is then removed and washed in a sequence of acetone, ethanol and DI water in an ultrasonic bath to remove the excess of acid on the surfaces. The subsequent annealing procedure is carried out in air in an oven at a temperature ranging from 300 to 360°C. To avoid thermal shock of the sample, the temperature is slowly increased up to the set point. For that, the annealing time is defined from the time the oven reaches the desired temperature. In [32] was demonstrated that the slow cooling of the samples after the thermal process results in long-term waveguide stability. Therefore, the samples are left to cool down to room temperature inside the oven while switching the latter off.

3.1.2 Optical characterization of fabricated waveguides

Two optical techniques are used to characterize planar waveguide samples: waveguide-mode spectrum measurement via prism coupling and X-ray diffraction analysis. The same techniques are used subsequently for process control during channel waveguides fabrication.

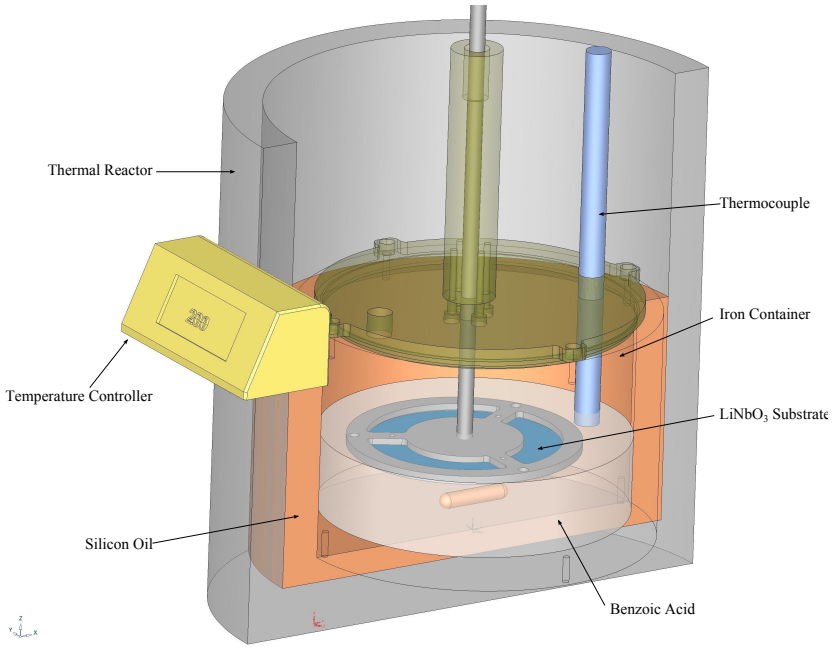

Figure 3.2: Proton Exchange set-up for waveguide fabrication.

Prism-coupling method

The optical characterization of waveguides consists in the determination of the refractive index profiles for several fabrication conditions. The PE process produces an increase of the extraordinary refractive index while decreases the ordinary index with respect to those of the un-exchanged $LiNbO_3$ substrate. Therefore, waveguide modes are of the TE type in *x*- and *y*- cut proton- exchanged lithium niobate and of the TM type in *z*- cut material. In order to find the mode effective indices, we employ the standard prism coupling technique [33]. A schematic of the experimental setup is shown in Fig. 3.3. One rutile prism (n_{er}=2.8719, n_{or}=2.5837) is pressed against the slab surface. A He-Ne laser beam emitting at a wavelength of 632.8nm hits the prism surface. Inside the prism the beam is totally reflected by the interface with the slab waveguide. The total

reflection in the prism is associated to an evanescent wave in the small air gap which is present at the interface between the slab waveguide and the prism. If the air gap is sufficiently small, the evanescent field can be coupled into the waveguide when the phase matching condition between the two fields is satisfied. This condition can be achieved by modifying the entrance angle of the laser beam. For that, a prism-coupling stage with (*x, y, z,* θ) movements is used. Once the coupling condition is satisfied, the field can propagate into the slab waveguide and basically no signal is measured by the photo detector (Fig. 3.3). By measuring the incident angle θ it is possible to calculate the effective index of the propagating mode through the relation:

$$N_m = n_r sin\left[\alpha_r - arcsin\left(\frac{sin\theta}{n_r}\right)\right] \tag{3.2}$$

where n_r is the rutile ordinary refractive index for TM modes or the extraordinary index for TE modes and α_r is the prism angle. The refractive index profiles throughout the guide depth are then reconstructed by the IWKB technique [34]. Moreover, to improve the precision, the surface increments Δn_e are determined as the average between the IWKB value and the value calculated using the Chiang method [35]. The reconstructed index profiles versus the depth are shown in Fig. 3.4 for different exchange conditions.

A 2D color map of the index variation across a 3 inches *z*-cut wafer is shown in Fig. 3.5. The measures have been performed on five different points over the surfaces, in order to check the homogeneity of the APE process. The variation of the refractive index increment over the entire surface can be addressed to the presence of a temperature gradient in the acid bath. The average refractive increment is about 0.0182 while the standard deviation is of the order of $6 \cdot 10^{-4}$.

X-ray diffraction analysis

To investigate the crystal structure after the PE process and confirm the results obtained from the prism coupling method, we recorded rocking

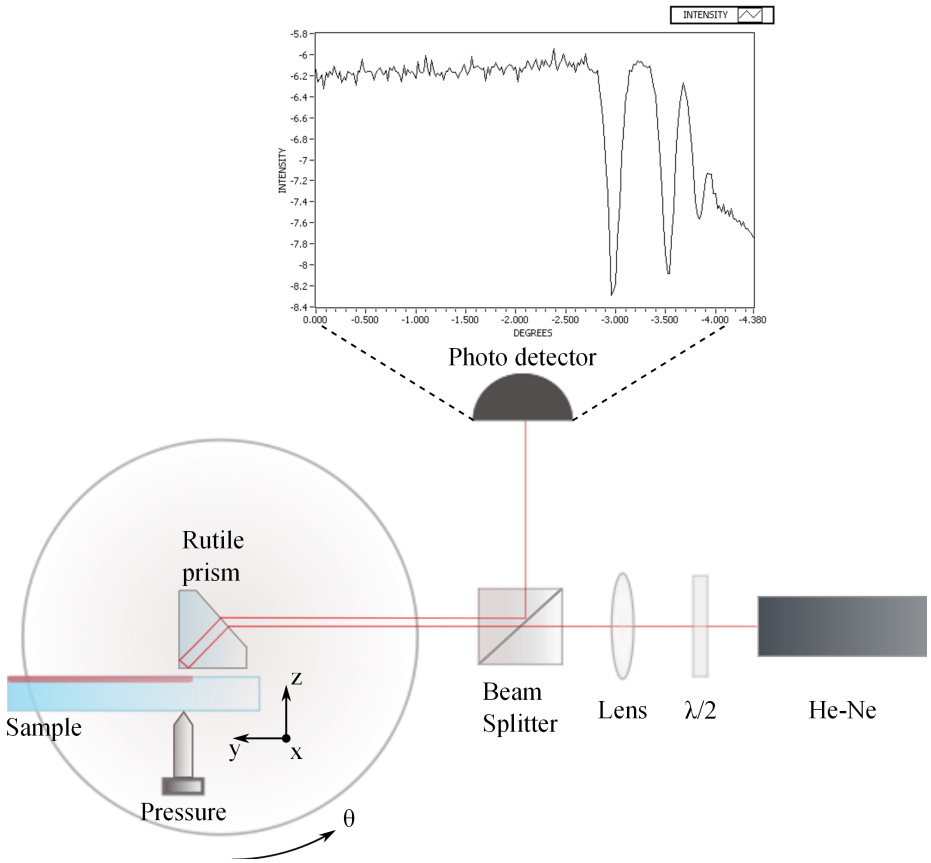

Figure 3.3: Experimental setup for the prism coupling method. The setup is completely automated by a GPIB controller. A recorded measurement for an annealed slab waveguide is also shown. It can be seen that the waveguide presents 3 modes at λ=633nm.

curves for different planes using a High Resolution X-Ray Diffractometer. Important information can be obtained from the observation of $\varepsilon_{33}^{"}$, the strain perpendicular to the substrate surface, which is directly deduced from the rocking curves, measuring the angular distance $\Delta\theta_{hkl}$ between the substrate peak and the exchanged layer peak on the rocking curve from the surface plane (hkl) through the relation:

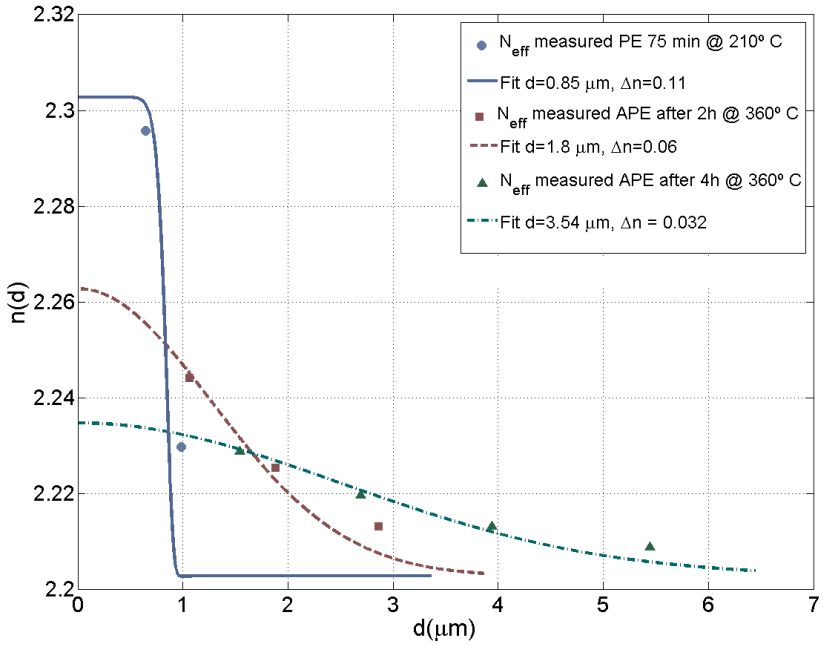

Figure 3.4: Measured indices for samples diffused at different times and temperatures and index profiles obtained by fitting with Gaussian functions.

$$\varepsilon_{33}^{"} = -\Delta\theta_{hkl} \cdot ctg\theta_{hkl} \tag{3.3}$$

where θ_{hkl} is the Bragg angle of the reflected surface plane for stress free-substrate. The rocking curves recorded with respect to (220) plane of z-cut samples obtained under different exchange and annealing conditions are presented in Fig. 3.6. From the position of the peaks on the rocking curves, corresponding to -100 arcsec, it can be deduced that the samples belongs to the α-phase of the crystal [28]. Because the distance between the $H_xLi_{1-x}NbO_3$ peak and the substrate peak (0 arcsec) corresponds to the magnitude of the strain, it is thus clear that the α-phase is characteri-

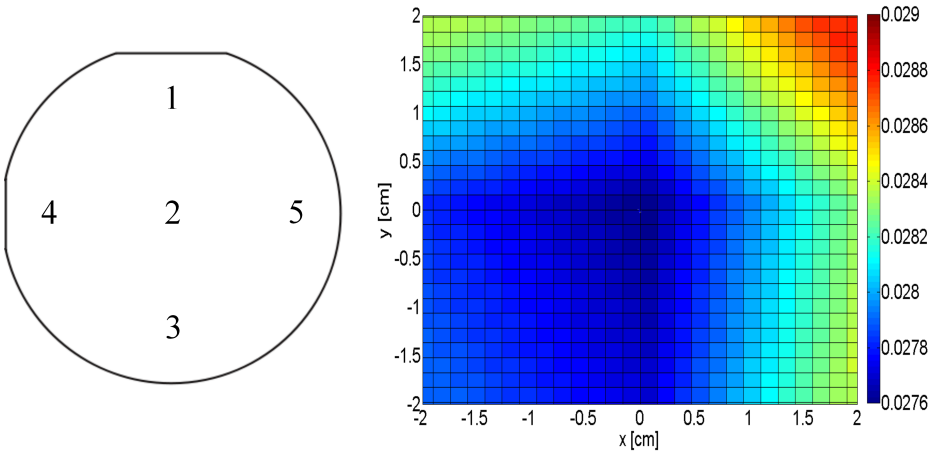

Figure 3.5: Refractive index variation in a 3 inch z-cut wafer.

zed by low deformation of the crystal lattice and therefore we expect low propagation losses and restored electro-optic coefficient.

3.1.3 Estimation of diffusion coefficients

Proton exchange being a diffusion process, the index profile depth, calculated by fitting with the specified function, should be a linear function of the square root of the exchange duration, according to equation:

$$d_a(T,t) = 2\sqrt{D_a(T,t)} \tag{3.4}$$

where T is the fabrication temperature (K), d_a is the guide depth (μm), t is the fabrication time (h), and $D_a(T)$ is the diffusion coefficient ($\mu m^2 h^{-1}$) at temperature T. In estimating the waveguide depths one should consider the combined process of lithium ions coming out of the substrate and protons going in. Therefore, $D_a(T)$ is an effective diffusion coefficient. Fig. 3.7 shows the relationship between waveguide depth and the square root of the exchange duration for z-cut waveguides which in our experiments was estimated to be D_{PE} (210°C) = 0.1092

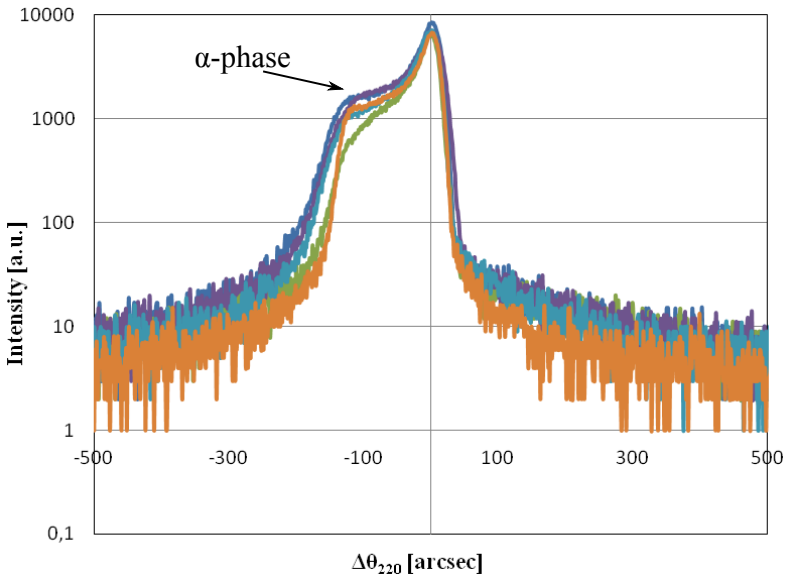

Figure 3.6: X-ray rocking curves for (220) reflection for 5 different samples. Fabrication conditions: PE in benzoic acid buffered with 1% of lithium benzoate, $T_{PE} = 210°C$, t_{PE} from 10 min to 75 min, annealing at $T_{APE} = 360°C$ for 10 h. It can be clearly seen that all the samples belong to the α-phase of the crystal.

$\mu m^2 h^{-1}$. The characterization of the subsequent annealing step consisted of the extraction of relations between the refractive index profile variations, caused by the thermal treatment after the initial exchange and the temperature and duration of the process. For that, several samples were fabricated in buffered benzoic acid at 210°C over a period ranging from 0.16h to 5h and then subjected to annealing at fixed temperature of 360°C. Considering the index variation proportional to the proton concentration [36] it is possible to determine the parameters of the guides that minimize Root Mean Square Error of the fit of the measurements with a Gaussian function. With the increase of the diffusion time, the RMSE decreases, confirming that the Gaussian function is a suitable fit for large diffusion depths.

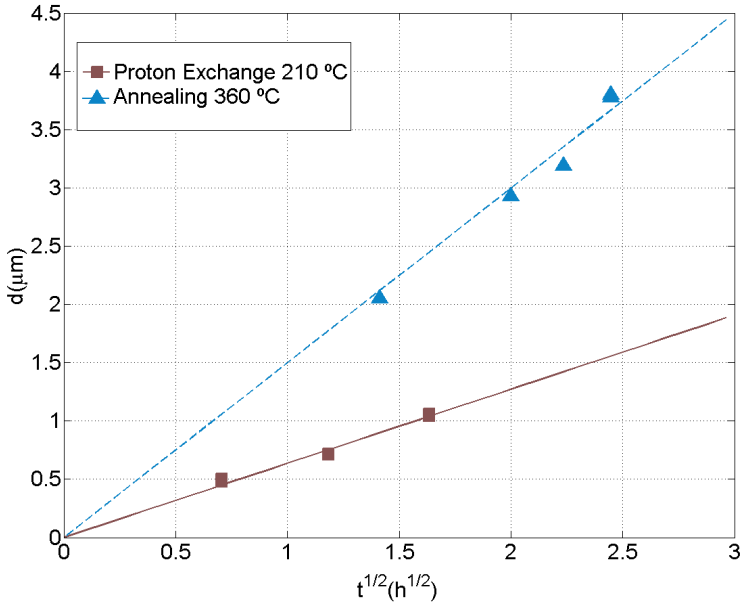

Figure 3.7: Profile depth as a function of the diffusion time for z-cut samples.

The anneal diffusion coefficient D_{APE} (360 °C) can be calculated using the expression 3.4. From the experiments it resulted to be 0.56 $\mu m^2/h$. While the experimental data fits the model reasonably well (Fig. 3.7), standard diffusion theory is eventually a poor approximation of the annealed process, especially in view of the fact that it occurs within multiple phases of the crystal and it does not consider the possible diffusion of *Li* in addition to that of *H* ions [14] and does not deal with the instability of PE waveguides. Recently, a new model has been proposed that take into account the mentioned inadequacies [32]. Since the diffusion coefficient D_{APE} is obtained from the optical measurements and so associated with the evolution of the index profile more than with the diffusion of *H*, it is interesting to notice that the found value is comparable with those described in literature for z-cut waveguides.

3.1.4 Channel waveguides fabrication

In practical applications, such as the fabrication of integrated modulators and sensors, the use of mono-mode channel waveguides is fundamental for high device performances. In most cases, theoretical analysis of their structure requires numerical simulations. A key characteristic of light propagating along the channel waveguide is its mode profile: the intensity distribution in the 2D cross section perpendicular to the propagation direction. The optical loss through a connection between a single mode channel waveguide and the optical fiber is mainly due to the mode-profile mismatch between the two. The channel mode profile is determined by the 2D index distribution across the waveguide, hence, strongly depends on the fabrication process. The refractive index profile can be expressed as:

$$n(x,z) = n_{sub} + \Delta n_e \left[f(x) g(z) \right] \tag{3.5}$$

where

$$f(x) = \frac{1}{2} \left[erf\left(\frac{w-x}{d_x} \right) + erf\left(\frac{w+x}{d_x} \right) \right] \tag{3.6}$$

and

$$g(z) = exp\left[\left(-\frac{z}{d} \right)^2 \right] \tag{3.7}$$

where n_{sub} is the extraordinary refractive index of $LiNbO_3$, Δn_e is the maximum index change due to proton exchange, $2w$ is the mask width and d_x and d are the diffusion lengths in the x- and z-directions, respectively from equation 3.6. The y-propagating single mode channel waveguides in z-cut $LiNbO_3$ for the telecom window has been fabricated following the method described previously. A metal mask (Al) having different slits, varying from 2.5 to 7 μm has been fabricated by photolithography and sputtering deposition. The process steps are shown in Fig. 3.8.

Waveguide mode profiles have been measured by imaging the near field patterns onto an infrared camera. An example of the measured width

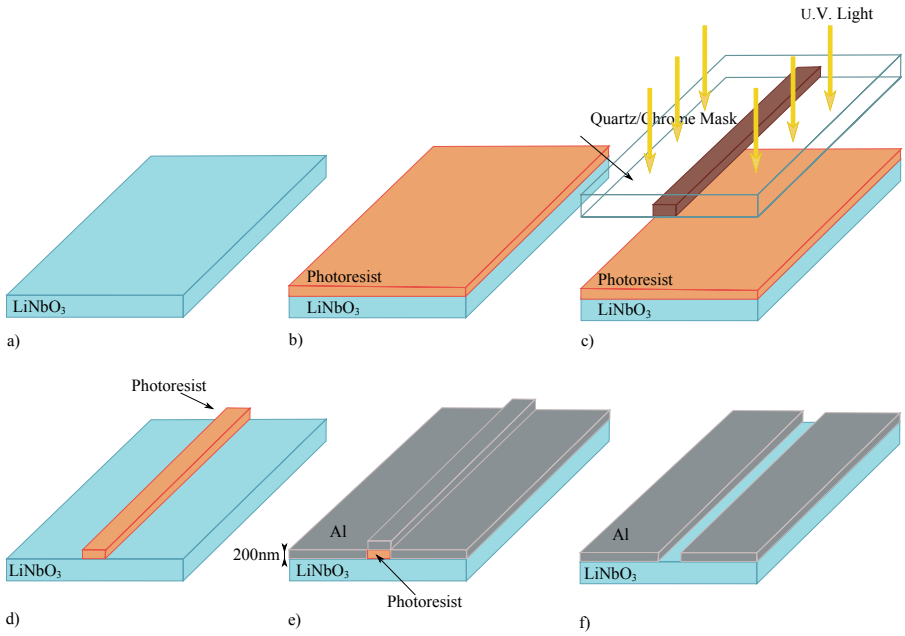

Figure 3.8: PE mask fabrication process. Example uses a $LiNbO_3$ and a positive photoresist system. Process steps include resist spinning, exposure, development, Al deposition and resist stripping.

and depth waveguide mode profile is shown in Fig. 3.9. The mode profile in the crystal plane is essentially Gaussian while in depth is asymmetric due to the large index difference between the waveguide and the cladding. By characterizing the waveguides fabricated it was possible to estimate the right diffusion parameters, which lead to have minimum propagation and insertion losses.

3.2 Domain engineering of $LiNbO_3$

Domain inversion in ferroelectrics is a well known phenomenon according to which the spontaneous polarization of a crystal is reversed by locally applying an electric field higher than the coercive field. Several

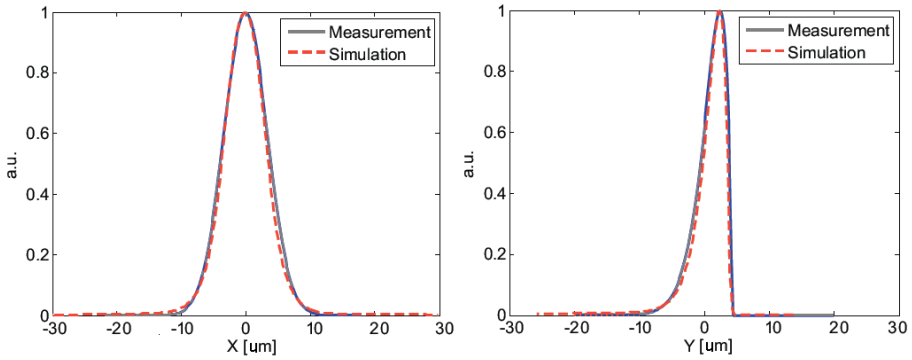

Figure 3.9: Measured optical mode profile in width and depth.

techniques have been studied in recent years to obtain domain inversion in ferroelectric crystals, mainly for nonlinear quasi-phase-matched frequency conversion. These techniques include for example electron-beam poling, [37, 38] electric-field poling, [39, 40] and high-voltage atomic force microscope [41]. Among those, electric field poling is a powerful and simple technique usually employed for fabricating periodic domain structures in ferroelectric crystals. It requires very simple facilities and is applicable to many nonlinear optical crystals with the possibility of being easily introduced in mass production. DI has different implementations even though the basic idea consist in patterning with the desired geometry one face of a $LiNbO_3$ wafer so that the patterned domains to be inverted can come into contact with a conductor - either deposited metal or liquid electrodes - and the other areas are electrically insulated - either by photo-resist or SiO_2 layer. A great number of domain structures have been formed using this technique. However, simple rectangular DI patterns can be employed to enhance modulator performance as described in chapter 4. Since the patterning of the poled areas is obtained through photolithographic imprint, it shares the same advantages and limitations. The experimental setup used to fabricate this type of device is depicted in Fig. 3.10. The system is really simple since it requires only a high voltage generator and some impedance. The electric field is applied all

over the patterned surface by liquid electrodes while the patterning is realized by opening a layer of evaporated SiO_2 or photo-resist. To ensure that the field is applied the charge corresponding to the area to be inverted s calculated. The charge, Q, is calculates using the expression:

$$Q = 2 \times P_s \times A \tag{3.8}$$

where P_s is the spontaneous polarization and A is the area.

To show the effectiveness of the technique, Fig. 3.11 reports a microscope picture of a DI grating where domains are revealed by differential etching in HF. The quality of the poling results (i.e. how precisely the inverted domains follow the desired pattern) depends on many factors, such as: surface flatness and polishing, sample cleanliness, quality of the insulator used and the patterning.

3.3 Room Temperature Direct Bonding

Direct bonding is a technique that allows to permanently join two pieces of the same or different materials with smooth and flat surfaces without any interstitial layer. This technique is commonly used in microsystems technology, where it is typically employed to bond two silicon wafers or a silicon wafer to a glass substrate. The first physical phenomenon that starts the bonding process is the adhesion of the two surfaces. After the contact is made, the chemically activated surfaces bond together due to Van der Waals forces, [42]. During bonding of different materials, the mismatch in thermal expansion coefficients (TEC) can cause significant thermal stress leading to the formation of cracks or defects [43]. For instance, since the TEC of $LiNbO_3$ is at least 3 times that of Si, the bonded substrate can fracture at temperatures above 150°C. Thus, bonding at low temperatures represents the best option when two or more substrates with high TEC mismatch are used, as it was recently demonstrated for $LiNbO_3$ using a room temperature surface activation method [44, 45]. Surface cleaning and pre-treatments are essential steps that determine the quality of the final bonding. Precise knowledge of the effects of cleaning and

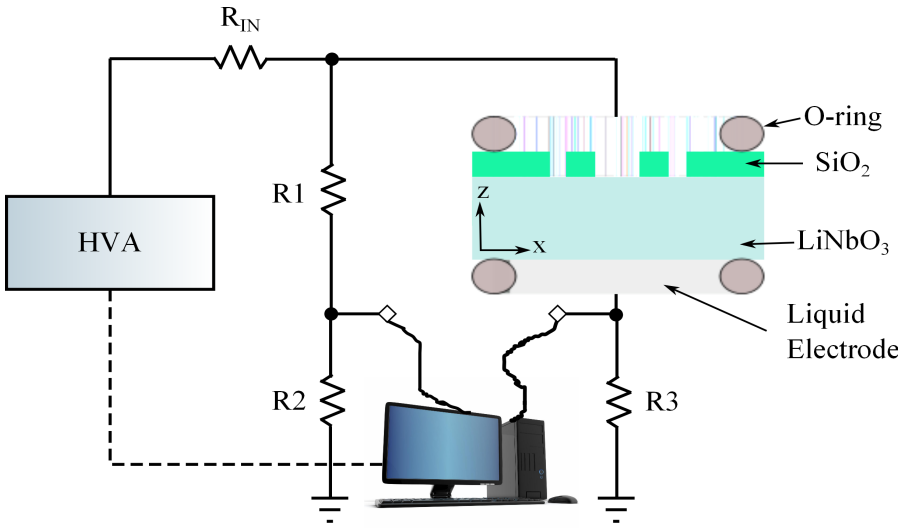

a)

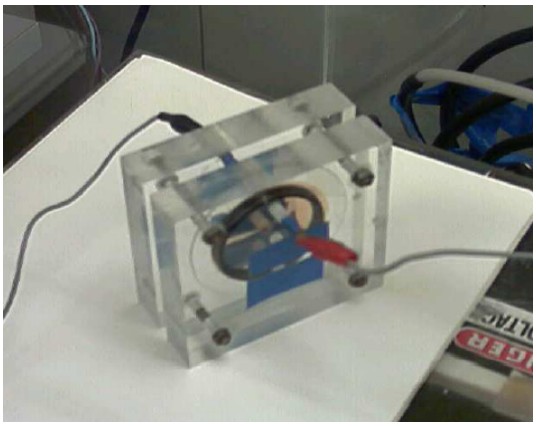

b)

Figure 3.10: (a) Schematic of electric field poling apparatus: HVA, high voltage amplifier, RIN series resistor, R1, R2, high voltage probes, R3, monitoring resistor, (b) poling Jig.

surface activation is crucial to control the surface free energy of the substrates in order to obtain high strength adhesive joints [46]. Current lit-

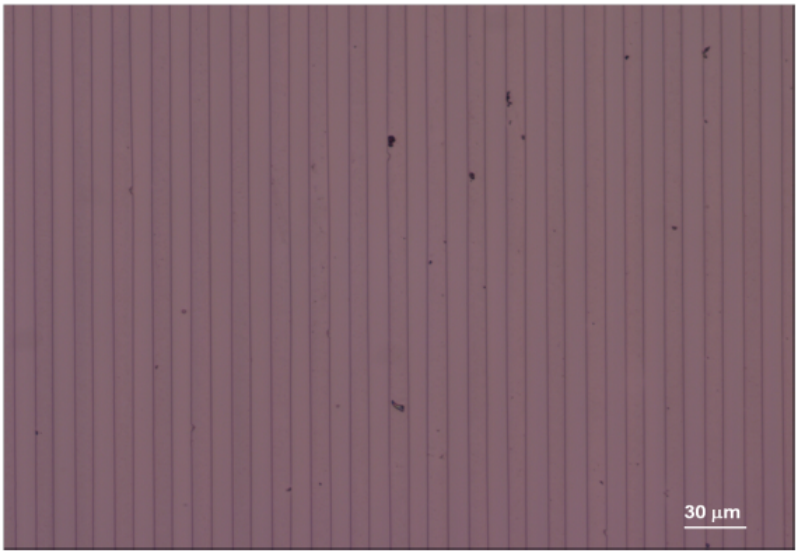

Figure 3.11: Microscope image of a sample of fabricated PPLN after etching.

erature doesn't report any systematic approach on the impact of cleaning and activation processes in the case of $LiNbO_3$. Moreover, this work also reports on the effect of plasma activation based on O_2 and Ar on $LiNbO_3$, Si and fused SiO_2 substrates. These studies have allowed to find the optimal parameters for a defect-free and strong room temperature bonding between different materials. An interesting technique based on UV laser illumination to activate the $LiNbO_3$ surface is presented in [47]. In this work, the attention has been focused on the effects on the surface free energy of other commonly used cleaning processes, that are well described in microsystems technology.

3.3.1 $LiNbO_3$ surface cleaning

The substrates used in these studies were 3 inch wafers of $LiNbO_3$, Si and fused SiO_2. The total thickness variation (TTV) of the substrates was less than 5 μm over the entire surface. The substrates with low TTV allow im-

proving the bonding quality by reducing the residual stress of the bonded samples. The 500 μm thick z-cut $LiNbO_3$ (Crystal Technology) and fused SiO_2 (Semiconductor Wafer) wafers were double side polished, while the 360 μm thick Si wafers (Montco Silicon) were single side polished. Table 3.1 describes the cleaning procedures and activation treatments while Table 3.2 reports the combinations of different cleaning procedures used in this work.

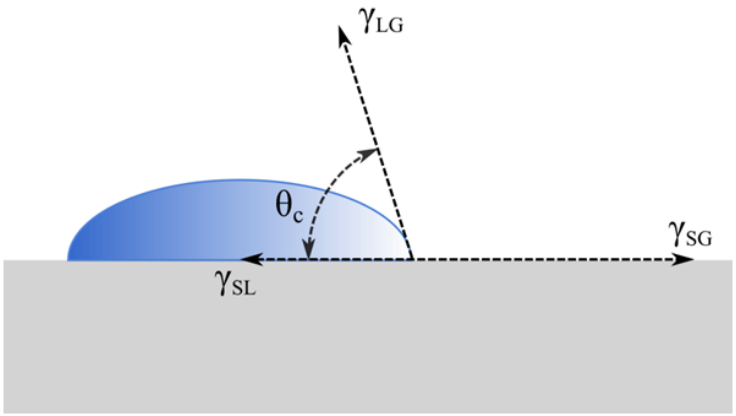

Figure 3.12: Contact angle measurement scheme.

The wettability of the sample surfaces was estimated by measuring the static contact angles of sessile drops of different probe liquids placed on the surface. An in-house built system was used while the measurement scheme is depicted in Fig. 3.12. The contact angle θ_c is defined as the angle between the substrate surface and the tangent to the drop profile at the line where the solid, liquid and vapor phases meet. The value of this angle is also a measure of the hydrophilic or hydrophobic character of the surface. The experiments were performed using two different probe liquids (Fischer Tinten Test) with surface tensions of 72 and 105 mN/m^{-1}, respectively. The volume of the dispensed liquid was controlled and fixed (5μL) for all the contact angle measurements, thus allowing an accuracy of $\pm 1^{\circ}$.

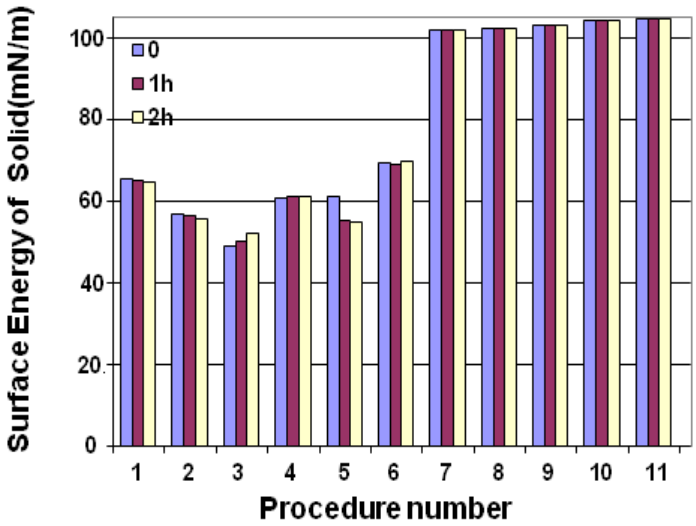

Figure 3.13: Surface free energy values for cleaning combinations listed in Table3.2

The wetting factor $\beta = cos\theta_c$ was estimated from the condition of equilibrium of forces on the boundary of three phases: solid state, liquid and gas (substrate, liquid drop and air) [42, 48]

$$\beta = cos\theta_c = \frac{\gamma_{SG} - \gamma_{SL}}{\gamma_{LG}} \tag{3.9}$$

and

$$\gamma_{SG} - \gamma_{SL} + \gamma_{LG} cos\theta_c = 0 \tag{3.10}$$

where γ_{SG} is the surface tension of the solid-gas boundary, γ_{LG} is the surface tension of the liquid-gas boundary and γ_{SL} is the surface tension on the liquid-solid boundary. Fig. 3.13 shows the results obtained for each cleaning combination.

The samples were kept in a dry box for different times after the treatments and then measured again. All the measurements were performed on both faces of the $LiNbO_3$ substrates and no relevant polarity dependence of the surface energy was found. One can see that properly stored sam-

Name	Chemical Treatment	Sonication	T(°)	time
Solvents	Acetone, Ethanol	YES	25	10 min/each
Piranha(A)	H_2SO_4 :H_2O_2 $(2:1)$	YES	60	10 min
Piranha(B)	NH_4OH:H_2O_2:H_2O $(1:1:5)$	YES	60	10 min
Micro Soap	Ultrasonic Soap (pH 8)	YES	25	10 min
DIW	DI Water Rinse	NO	25	10 min
NH_4OH	Ammonia Rinse	NO	25	2 min

Name	Plasma Treatment	Gas	time
Ar Plasma	Pressure: 35mTorr Flow:50sccm Power:15W RF, 800W ICP	Ar	15s, 30s, 60s
O_2 Plasma	Pressure: 35mTorr Flow:50sccm Power:15W RF, 800 W ICP	O_2	15s, 30s, 60s

Table 3.1: Chemical and plasma activation treatments for surface cleaning and activation.

No.	Solvents	DIW	Piranha(A)	DIW	Micro Soap	Piranha(B)	NH_4OH	DIW
1		X						
2	X							
3	X	X						
4	X	X			X			X
5	X	X				X		X
6	X	X				X	X	
7	X	X			X	X		X
8	X	X			X	X	X	
9	X	X	X					X
10	X	X	X	X	X	X		X
11	X	X	X	X	X	X	X	

Table 3.2: Cleaning combinations for $LiNbO_3$ substrate.

ples don't lose significantly their wettability at least in the first 2 hours after the treatment. A test liquid with a surface tension of 105 mN/m has been used in order to be more sensitive at higher surface energies. From Table 3.2, it can be seen that the values of the cleaning combinations 7 to 11 of are very similar. Thus, these processes are ideal candidates for the cleaning, allowing at the same time to prepare the surface in a high surface energy state.

3.3.2 Plasma activation

To determine the optimal plasma activation on $LiNbO_3$, Si and fused SiO_3 substrates, the samples were cleaned with organic solvents (procedure 2 of Table 3.2) and acid Piranha (procedure 9 of Table 3.2). Only for Si, an oxide removal in BOE $7 : 1$ $(NH_4F : HF)$ was performed before the plasma process. After the last rinsing with DI water and blow drying with nitrogen, the samples were left to reach the original value of surface energy storing them in a particle-free environment. For surface activation, an inductively coupled plasma (RIE-ICP) system (Plasmalab System 100, Oxford instrument) has been usedin combination with two different gases: O_2 and Ar. In the experiments, typical treatment conditions were 35mT pressure, 50 sccm flow rate, 15W source power, and 800W ICP power. Since a short treatment time is desirable to strengthen the bonding energies [38], the process time vas varied from 15s to 60s as shown in Table 3.1. Fig. 3.14 (a) and (b) reports the results of the surface energy measurements for the three substrates under different treatment conditions compared to their starting values (0 seconds). After plasma treatment the contact angle of these materials become smaller (higher surface energy) compared to those of untreated substrates showing a strong increase in their wettability. The three substrates treated for 30s with O_2 plasma present the lowest contact angle as compared to those treated with Ar. Apart from lower values of contact angles, O_2 plasma presents the advantage of producing a smoother surface with compared to Ar. For these reasons this process is the best candidate among those studied to obtain a strong bonding.

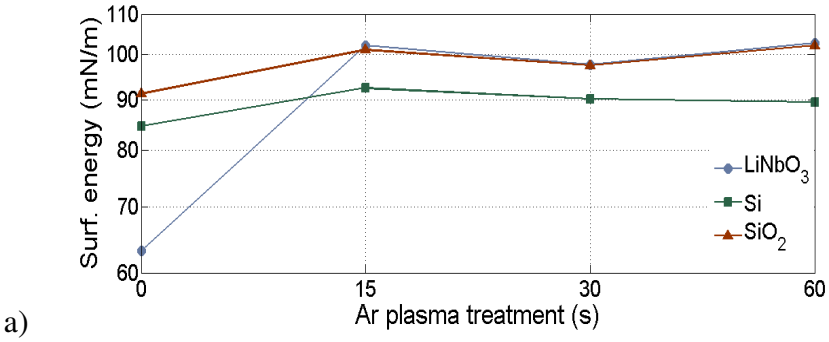

a)

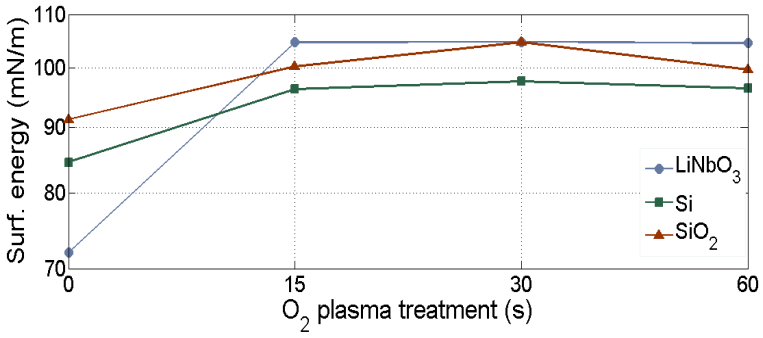

b)

Figure 3.14: Contact angle of $LiNbO_3$, Si and Fused SiO_2 treated by a) Ar plasma and b) O_2 plasma.

3.3.3 Bonding test and Lithium Niobate thinning

The results presented above indicate the optimal cleaning and plasma activation treatments for bonding. To test their effectiveness bonding between two $LiNbO_3$, $LiNbO_3$ and Si, $LiNbO_3$ and fused SiO_2 wafers was carried out. All the substrates were cleaned following procedure 10 in Table 3.2. After cleaning, the substrates were treated with 30s O_2 plasma and subsequently they were dipped in DI water for 20 min and blow dried with N_2. The bonding step was realized immediately after drying with no load force but just putting into contact the two substrates and gently pushing at the center of the sample. The bonding started from the contact point and propagated to all the samples. The bonded samples are shown

in figure Fig. 3.15 and no bubbles or cracks are visible at naked eyes for all of the samples. To inspect the bonding interface, the hybrid substrates were diced. The bonding was strong enough to allow cutting of the hybrid substrate for cross-section observation without formation of evident crack.

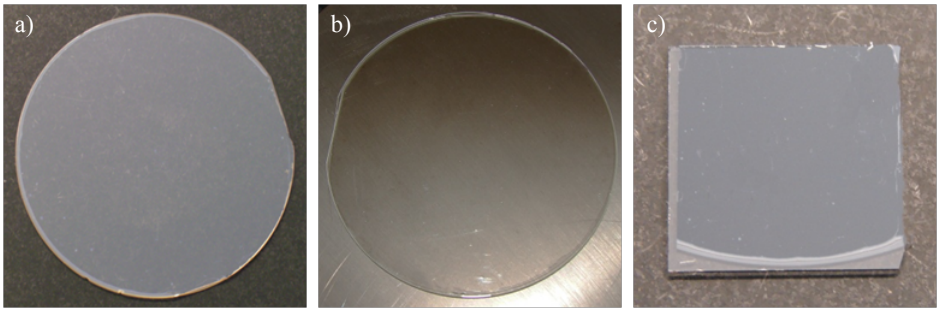

Figure 3.15: Bonding test of a) 3 inch z-cut $LiNbO_3$/$LiNbO_3$ wafers, b) 3 inch $LiNbO_3$/Fused SiO_2 and c) $LiNbO_3$/Si bonding after cutting with diamond saw.

The SEM images of the three bonded interfaces are shown in figures Fig. 3.16 a-c. On the cross-section, the interface is not distinguishable for $LiNbO_3$/$LiNbO_3$ (Fig. 3.16a) while it is visible for $LiNbO_3$/Si (Fig. 3.16b) and $LiNbO_3$/SiO_2 (Fig. 3.16c). The interfaces are sharp and no interstitial space or defect can be seen, proving the quality of the bonding process on the microscopic scale. After bonding and dicing, the $LiNbO_3$ on the $LiNbO_3$/$LiNbO_3$, and $LiNbO_3$/SiO_2 chips was thinned down using a tabletop polishing machine (PM5, Logitech). The specimens were mounted on a vacuum holder in order to avoid the use of any wax and ensure a major flatness of the polished surfaces. For bulk-thinning, a succession of 15μm, 9μm and 3μm alumina (Al_2O_3) slurries were used in conjunction with a cast iron plate. Alkaline colloidal silica suspension (SF1, Logitech) was used with a cloth pad for optical finish. The rotation velocity of the plates was varied from 20 rpm to 50 rpm while the down pressure of the sample holder from 100g to 800g. By adjusting the plate velocity, the holder pressure and the size of the abrasive slurries, it

was possible to control the removal rate of the $LiNbO_3$ layer and reduce its thickness from 500μm to 15μm without any noticeable damage for the surface Fig. 3.16 d shows the SEM image of the thin plate $LiNbO_3$ bonded to another $LiNbO_3$ thick plate.

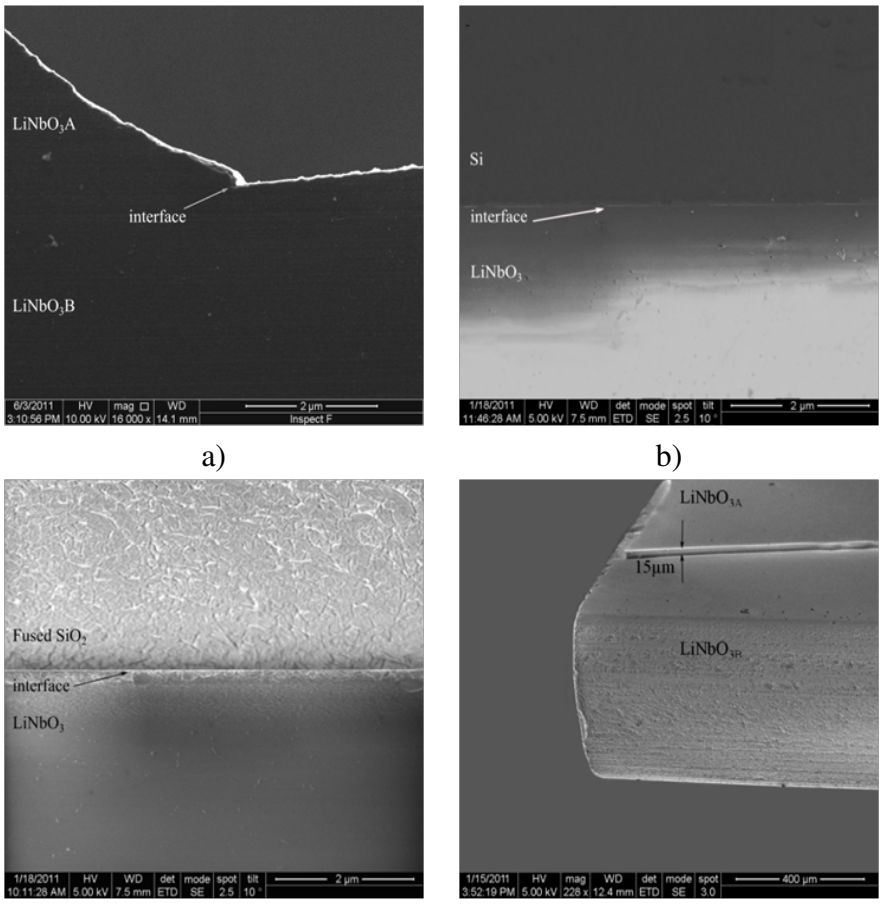

a) b)

c) d)

Figure 3.16: SEM cross sectional micrograph of a) $LiNbO_3$/$LiNbO_3$ bonding, b) $LiNbO_3$/Si bonding, c) $LiNbO_3$/SiO_2 bonding. D) Thin plate of $LiNbO_3$ bonded to another $LiNbO_3$ substrate.

Chapter 4

Ultra performing micro-structured modulators

4.1 Introduction

Over the past decade the demand for telecommunication services has strongly increased and the consequent requirement for ever larger bandwidth communication system has boomed accordingly. In this scenario, optical networks play a fundamental role as main carriers of information and are continuously growing in importance due to their increasing presence in last-mile connections and fiber-to-the-home (FTTH) links [49]. If the bandwidth demand of the users increase at home and premises, so does such demand for all the types of network, be it long-haul, metro or FTTH. Inside optical transmission systems, high speed optical modulators are one of the fundamental building blocks (see Fig. 4.1 for a typical scheme of an optical link). Among them, external Lithium Niobate ($LiNbO_3$) modulators are extremely effective [50], in particular for long haul and metro applications, as it is shown by their recent increasing commercial volume. Indeed, total worldwide revenue for digital dense wavelength division multiplexed (DWDM) transmission doubled over last year.

This is reflected by the $LiNbO_3$ modulators' market (Fig. 4.2) [51].

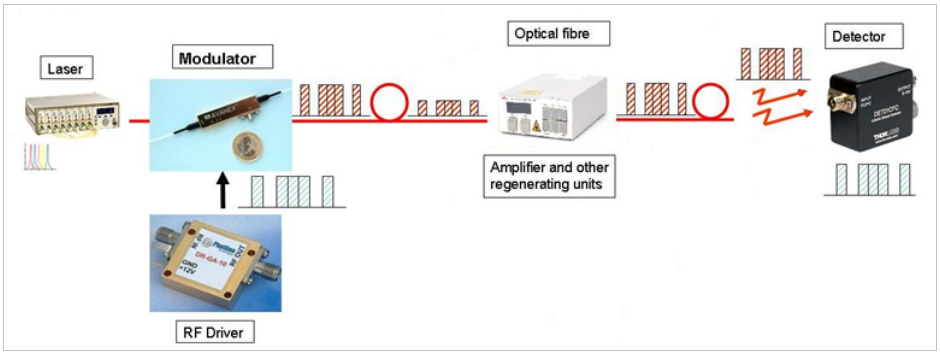

Figure 4.1: Schematic of an optical communication link showing the use of an integrated electro-optic $LiNbO_3$ modulator.

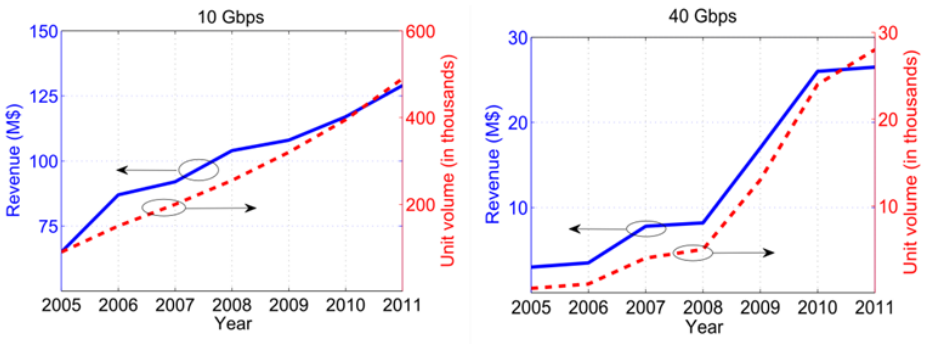

Figure 4.2: Trends in $LiNbO_3$ modulators market for digital telecommunications.

Note that data refer only to digital communications. These facts are well understood taking into account that $LiNbO_3$ modulator possesses very good performance in terms of extinction ratio, insertion loss, chirp feature and optical transparency - the latter particularly important taking into account the increased use of tunable laser sources. Moreover, with respect to modulators based on semiconductor or other materials, $LiNbO_3$ market share could even become larger if performance, integration and cost further improve. Among others, the required improvements should in-

clude, at the same time, high modulation efficiency (i.e. large modulation bandwidth at low driving voltage) and robust and economic large-scale fabrication process. Even though the use of velocity matched (VM) travelling wave electrodes configurations [50, 52] greatly increase the modulation bandwidth (BW), the potential of $LiNbO_3$ in terms of modulation efficiency has been far from being fully exploited. In fact, the frequency dependent microwave loss limits the bandwidth of VM modulators: the higher the frequency the higher the microwave loss. Thus, for a given length L, the effective modulation length reduces at high frequency, so does the efficiency. This makes BW inversely proportional to L, similarly to the switching voltage (V_π) that is needed to obtain a full swing along the modulation curve. Therefore a trade-off exists between V_π and BW and the ratio BW/V_π is used as a figure of merit. To improve the efficiency (increase of BW/V_π), better coupling between the microwave and optical fields is required. Different solutions have been proposed to this end. In particular, ridge and thin plate modulators can provide a step forward by enhancing the microwave field confinement thus increasing the overall electro-optic interaction [53, 54]. Besides these approaches, that require more additional fabrication steps with respect to standard ones, the exploitation of the polarizability (i. e. domain structure) of $LiNbO_3$ opens interesting scenarios in the micro-engineering of devices toward a higher efficiency. Domain inversion (DI) in ferroelectrics, such as $LiNbO_3$, has been widely exploited in all-optical processes, from quasi-phase-matched second harmonic generation to optical parametric oscillation and WDM frequency conversion[39, 55, 40]. So far its use in electro-optics has been mostly limited to quasi-velocity matching devices using periodic structures [56, 57] or to achieve a desired chirp value for high-frequency and broadband modulators [58]. More recently, domain engineering of z-cut $LiNbO_3$ structures has been proposed to produce large bandwidth and very low voltage modulators where the push-pull effect in the interferometric structure has been obtained by placing the waveguides in opposite-sign electrooptic coefficient regions (i.e. opposite-oriented domains) and under the same electric field [59]. This is in contrast with previous high frequency modulating structures in single domain crystals where the two

waveguides are placed under two distinct electrodes having different (usually opposite sign) voltages [50]. Further increase in efficiency for optical links can be achieved not only by improving the performance of modulators but also adopting new modulation formats. These type of formats like differential phase shift keying (DPSK) and differential quadrature phase shift keying (DQPSK)improve spectral efficiency (bits/s/Hz) reducing the cost of information transport. Modulators targeted for these novel communication formats can benefit from the micro- structuring techniques and design developed during this work.

4.2 Mach-Zehnder modulator

Light waves have many characteristics that can be modulated to carry information, as the intensity, phase, frequency and polarization. Among these, amplitude modulation is the most used for optical fiber communication systems due to the simplicity of envelope photo-detection. In the case of external amplitude modulators, the two most used mechanisms to create modulation are the electro-optic effect and the electro-absorption. Concerning electro-optic modulators, a tremendous variety of designs have been proposed over the last 30 years. In this work we will focus our attention on the most popular device for implementing optical intensity modulation: the travelling wave Mach-Zehnder Interferometric modulator (MZI).

4.2.1 Fundamentals of travelling wave modulators

The basic working principle of the Mach-Zehnder interferometer is illustrated in Fig. 4.3. An optical power $E = 2$ enters in a single mode dielectric optical waveguide which splits into two single mode waveguide branches. In each branch the optical field undergoes a phase shift $\Delta\phi$ which is opposite in phase for the two branches.

If the optical waves are in phase after propagating through the two arms, they combine as a single mode in the output Y-branch, which result

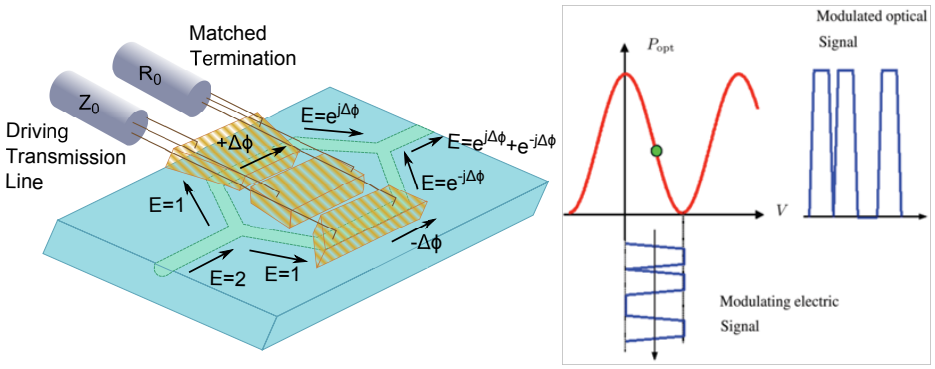

Figure 4.3: Schematics of a MZ interferometer and electrical-to-optical transfer function.

in a maximum intensity output; whereas if the optical waves are out of phase after propagating through the two arms, they combine as a higher order spatial mode, therefore most of the optical power becomes unguided and the output intensity is a minimum. The optical field amplitude at the output of the MZM can be express as:

$$E = e^{+j\Delta\phi} + e^{-j\Delta\phi} = 2cos\Delta\phi \tag{4.1}$$

which result in the optical power modulation curve plotted in Fig. 4.3. For travelling-wave modulators, the electrode, of length L, forms an extension of the driving transmission line and should have the same characteristic impedance as the signal generator and cable (see Fig. 4.3). Both light and microwaves propagate in the same direction. The bandwidth is not limited by the electrode capacitance but rather by the difference in velocity (velocity mismatch) between light and microwaves (MW), and by the microwave propagation loss. The velocity mismatch depends on the $LiNbO_3$ material and the thickness of the buffer layer in addition to the electrode structures. In order to consider the velocity mismatch, we can imagine a point of constant phase in the optical wave travelling through the modulator. If the modulator is short enough, or if the modulating frequency is low enough, the voltage applied to the waveguide (and, therefore, the change in its refractive index) will be the same during the time

that the point of constant phase needs to travel across the whole active length. But if the frequency is high enough, so that the MW period is comparable, or even smaller, to the transit time of the light, our point of constant-phase might experience different refractive indices during its trip through the active length. In this case, the effective modulation voltage will be an average depending on the difference between the velocities of the optical mode and the MW mode. Therefore, the modulation efficiency will be decreased. Let us imagine a microwave propagating through a MW waveguide in the positive z direction. The effective voltage seen at position z ($0 \leq z \leq L$) along the modulator by photons that enter the active region ($z = 0$) at the time t0 is given by:

$$V(z, t_0) = V_0 sin 2\pi f_m \left[\left(\frac{\Delta n}{c} - t_0 \right) - \phi_0 \right] \tag{4.2}$$

where V_0 is the amplitude of the wave, $\Delta n = n_m - n_{opt}$ is the mismatch between the refraction indices of the micro (n_m) and the optical (n_{opt}) waves, f_m is the microwave frequency corresponding to the wavenumber $k_m = 2\pi n_m / \lambda_m$ and ϕ_0 accounts for a phase mismatch between optical and modulating waves. From equation 4.2, it is clear that the amplitude $V(z)$ will be constant for a certain phase constant point of the optical wave when the index mismatch is zero. Otherwise, a different value of Δn will give an oscillating behaviour of V along the interaction length L, that will induce an average accumulated phase-shift. The total elecro-optically induced phase shift $\Delta\phi$ for photons incident a $t = t_0$ is:

$$\Delta\phi(t_0) = \frac{\pi n_{opt}^3}{\lambda} r \frac{\Gamma}{G} \int_0^L V(z) dz \tag{4.3}$$

In equation 4.3 the coefficient Γ is the overlap integral between the optical and microwave electric fields, defined as [52]:

$$\Gamma = \frac{G}{V_0} \frac{\int E_m \cdot |E_{opt}|^2 \, dS}{\int |E_{opt}|^2 \, dS} \tag{4.4}$$

with G representing the spatial gap between the electrodes, E_m and E_{opt} the microwave and optical fields integrated over the modulator cross

section. By inserting 4.2 into 4.3 we can calculate the phase-shift experienced by the optical wave as a function of the modulation frequency and the relative phase between optical and modulating waves:

$$\Delta\phi = \frac{\pi n_{opt}^3}{\lambda} r \frac{\Gamma}{G} L V_0 \frac{sin(\theta)}{\theta} sin(\theta - \phi) \tag{4.5}$$

where the variable θ is given by:

$$\theta = \frac{\pi f_m \Delta n L}{c} \tag{4.6}$$

In 4.5 we can see that the phase shift is a function of the modulating frequency and assume the form given by the term $sin(\theta)/\theta$. The frequency where $\Delta\theta$ is reduced to $1/2$ of its maximum value at $f = 0$ occurs when $\theta = 1.9$. This is known as the 3dB optical bandwidth and is given by:

$$\Delta f(3dB_{opt}) = \frac{1.9c}{\pi \Delta n L} \tag{4.7}$$

The frequency, instead, where $\Delta\theta$ is reduced to $\sqrt{1/2}$ of its maximum value occurs when $\theta = 1.9$. This is known as the electrical bandwidth and is given by:

$$\Delta f(3dB_{el}) = \frac{1.4c}{\pi \Delta n L} \tag{4.8}$$

Either 4.7 or 4.8 refers to as bandwidth, but since different definitions exist in literature, it is important to be specific. The frequency response of the modulated optical output is known as the optical response. In the calculation of the bandwidth of the optical response one as to take into account the impedance, the losses mismatch and the velocity mismatch [60] as already described above. The characteristic impedance of the transmission line (Z) is given by the relation between the voltage and current traveling through the line and it is of special importance as it will determine the reflections of the MW signal. MW sources and cables are usually matched to 50Ω impedance. If we try to connect these 50Ω devices to a

waveguide having different characteristic impedance, the voltage signal will experience a reflection at the boundary between both given by [61]:

$$R = \frac{Z_2 - Z_1}{Z_2 + Z_1} \tag{4.9}$$

where Z_1 is the impedance of the waveguide before the transition and Z_2 is the impedance of the waveguide behind the transition. If the impedance of the waveguide is far from being matched to the generator, a significant amount of power can be reflected, which might become harmful for the generator itself. Besides, if the waveguide impedance is not matched to the load impedance, the reflected power will generate a standing wave inside the waveguide, which will distort the signal and decrease the modulation efficiency of the device. Obviously, the higher the modulation frequency is, the shorter the correspondent wavelength becomes and, therefore, the more significant these reflections and standing waves are. For these reasons, it is important to design the modulator electrodes in such a way that they provide characteristic impedance as close as possible to 50Ω. Typically, values between 40 and 50Ω can be reached by carefully choosing the geometry and the material of the electrode structure. Another factor that determines the frequency response is represented by the electrical loss generated both in the conductive and dielectric materials. In [62] it has been demonstrated that the dielectric losses are negligible below 20 GHz. Above this frequency they become more significant, although they are usually one order of magnitude smaller than conductor losses. The attenuation constant due to the conductor loss can be written as [63]:

$$\alpha_c(f) = \frac{1}{2}\frac{R(f)}{Z} \tag{4.10}$$

where $R(f)$ is the series resistance per unit length of the transmission line. This resistance can be calculated by using the Wheeler's incremental rule that requires that the conductor thickness is about four times larger than the skin depth:

$$R(f) = 2\epsilon_0 R_S(\frac{\partial}{\partial G} - \frac{\partial}{\partial W} - \frac{\partial}{\partial t})\frac{1}{C_0} \tag{4.11}$$

where G is the gap between the electrodes, W and t, the width and the thickness respectively. C_0 is the electrode capacitance when all dielectrics are replaces by air and R_s is the surface resistance of the conductor, given by:

$$R_s = \pi f \mu_0 \delta \tag{4.12}$$

with f being the frequency and δ the skin depth, that can be expressed as:

$$\delta = \sqrt{\frac{1}{\pi f \mu_0 \sigma_c}} \tag{4.13}$$

where σ_c is the electrode conductivity. The value of derivatives in equation 4.11 depends on the electrode geometry but we can see from equation 4.10 to 4.12 that the conductor loss is proportional to the square root of the frequency. Then we can write a simplified equation for the conductor loss as follow:

$$\alpha_c(f) = \alpha_{c0}\sqrt{f} \tag{4.14}$$

where α_{c0} is the attenuation coefficient normalized at 1 GHz. The dielectric losses, instead, are considered linearly dependent on the modulation frequency. Therefore we can write the total frequency dependent loss as:

$$\alpha(f) = \alpha_{c0}\sqrt{f} + (\alpha_{dL} + \alpha_{dS})f \tag{4.15}$$

where α_{dL} and α_{dS} are the dielectric losses in the $LiNbO_3$ and SiO_2 substrates [64], respectively. The frequency response can be then calculated as function of the phase shift at DC, $\Delta\phi(DC)$, and at a frequency f $\Delta\phi(f)$, as [60]:

$$m(f) = \left|\frac{\Delta\phi(f)}{\Delta\phi(DC)}\right| = e^{-\frac{\alpha L}{2}}\sqrt{\frac{sinh^2(\frac{\alpha L}{2}) + sinh^2(\frac{\zeta L}{2})}{(\frac{\alpha L}{2})^2 + (\frac{\zeta L}{2})^2}} \tag{4.16}$$

with $\zeta = 2\pi(n_m - n_{opt})/c$ and c being the speed of light in vacuum. Using equation 4.3 and 4.16 we can derive the expression for the switching voltage - corresponding to a phase change of π and producing a theoretical zero optical output:

$$V_\pi = \frac{\lambda G}{2n_{opt}^3 Lr\Gamma} \tag{4.17}$$

The expressions 4.7, 4.8 and 4.17 clearly shows the inverse dependence on the length of the modulator for bandwidth and driving voltage. In order to increase the modulator efficiency the ratio BW/V_π has to be increased. A direct way to obtain this is to increase the overlap integral Γ. To this end, the solution we propose is to locate the arms of the interferometers under a narrower and more efficient electrode (Domain Inverted push-pull configuration).

4.3 State of the art

The need for higher bandwidth to manage the increasing amount of information, that every day is sent into the optical networks, has driven the research to device designs able to reach modulation bandwidths of the order of 40 Gb/s and even 100 Gb/s. Nevertheless, the design of a broad band device, with the current technology, leads to higher driving voltages to work, with a subsequent increase in the drivignsystem costs. Therefore, in order to develop reasonable high speed modulators, they must work also with lower voltages so that inexpensive driving electronics (for example, SiGe based) can be used. As already said above, lowering the driving voltage and extending the bandwidth of an integrated electro-optic modulator (EOM) compete with each other, so tradeoffs must be searched. Various modulator structures have been developed in order to improve modulator efficiency. Recently, the use of ridge waveguide modulators has been widely explored in order to reduce the optical mode size and to decrease the effective refractive index of the modulating microwave. This is possible because part of the $LiNbO_3$ around the waveguide is substituted by a

low index medium as air and/or SiO_2, which implies a reduction of the average dielectric constant of the material surrounding the electrodes. The effect of the ridge also implies that electrodes do not need to be as thick as in planar structures (typically in the range of 20 μm) in order to get the matching conditions. The product $V_\pi \cdot L$ predicted for these devices was in the order of 8 to 9 V·cm compared to a typical value of 12 V·cm for standard modulators [65]. Moreover, it was also predicted that the ridge allows smaller bending radius in waveguides without increasing losses, thus improving the integration level of photonic devices [66]. Fabricated ridge structures in MZ modulators have shown bandwidths in the order of 40 GHz with driving voltages as low as 3V [67, 68]. Apart from ridge modulator, another way of enhancing the field confinement is given by thin plate modulators [69]. For those, the EO crystal is uniformly thinned down to dimensions of the order of 10 μm, by precise lapping and polishing, after an appropriate bonding on a low dielectric constant substrate (e.g. SiO_2), that is used to decrease the effective microwave index. Therefore, the modulating electric field is subjected to a higher confinement and forced to be parallel to the crystal z-axis. Note that, contrary to the ridge and domain inversion geometries in z-cut crystal, the thin plate geometry requires an x-cut crystal. Consequently, the position of the optical waveguides with respect to the electrodes changes. Waveguide fabrication relies on traditional techniques like Ti-indiffusion and no SiO_2 buffer is needed due to the configuration of electrodes required for x-cut $LiNbO_3$ modulators. While both ridge and thin plate modulators work on the optical and/or RF field confinement, DI aims at improving the coupling by allowing simpler electrode configurations. This technique allows the use of opposite electro-optic coefficients in each waveguide of a Mach-Zehnder structure in such a way that the same electrode can provide the same electric field for both and still induce a push-pull operation. This provides new freedom degrees in the fabrication of electrodes, so that their MW properties can be tailored in order to get better velocity and impedance matching. In Table 4.1 we report the current state-of-the-art product and publication work.

	Bit Rate (Gb/s)	Modulation format	L (mm)	Δ f (GHz)	V_π (V)
State of the art commercial	10	NRZ	35-43	≥ 10	≤ 6
		Duobinary, DQPSK	50-58	≥ 8	≤ 4
	40	NRZ	45-63	≥ 30	≤ 6
			75-83	≥ 30	≤ 3.5
		Duobinary, DQPSK	75-83	≥ 30	≤ 3.5
State of the art pubblications	Ridge [68]		60	40	5
	Domain Inversion [59]		40	10	≤ 3
	Thin Plate [70]		30 (folded structure)	20	≤ 3

Table 4.1: State of the art commercial products and published work.

4.4 Ultra Low Voltage Modulator: Device Design

This work has been realized with the collaboration of Avanex Corporation (now Oclaro inc.).

4.4.1 Device Design

The cross section of the proposed modulator highlighting the working principle is shown in Fig. 4.5. Note that there is a silica based buffer layer between the hot electrode and lithium niobate crystal. This layer ensures at the same time low optical loss by keeping the evanescent optical field low in the lossy metal electrodes and velocity matching between the traveling optical and microwave fields.

The key modulators parameters (V_π, α, n_m, Z_0) were calculated, using a commercial FEM solver (Comsol) [71, 72], as a function of the geometric parameters (see Fig. 4.5). Here, *G* is the electrode gap, *W* is the width of the central electrode, *t* and τ the electrode and the buffer layer thickness, respectively. Fig. 4.6 presents the results for the modulator parameters as a function of the central electrode width *W* and the electrode

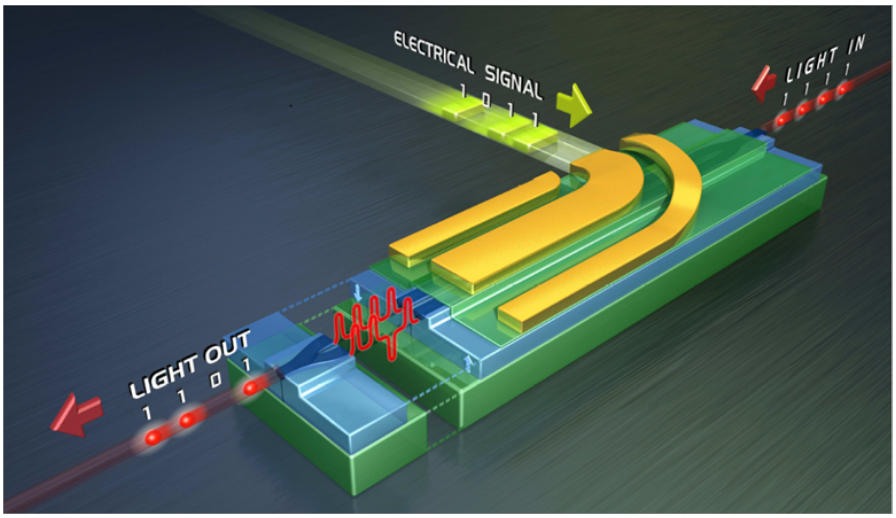

Figure 4.4: Mach-Zehnder exploiting domain inversion for ultra low voltage operation.

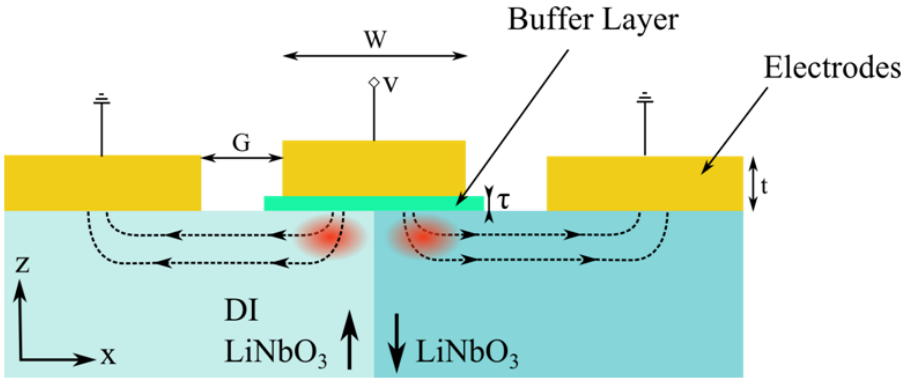

Figure 4.5: Cross section of the Domain Inverted z-cut $LiNbOO_3$ modulator.

gap G. We can observe that the microwave index is still high. In order to maximize the bandwidth of the modulator, it is necessary to match the device's microwave effective index to that of the optical effective index

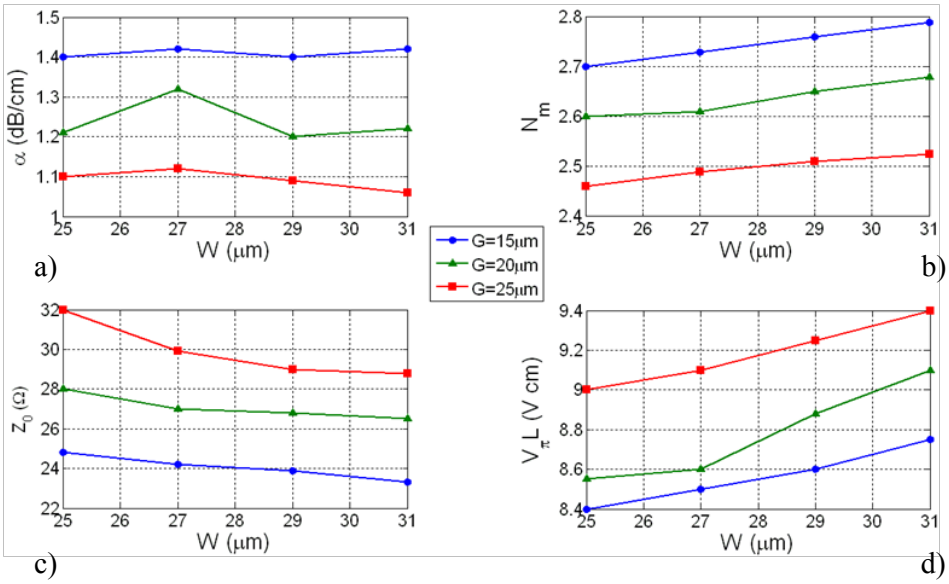

Figure 4.6: Calculated modulator characteristics as a function of the electrode width W, taking the electrode gap G as parameter. (a) Losses, (b) microwave effective index,c) characteristic impedance, (d) voltage-length product.

($n_{opt} = 2.14$ @ $\lambda = 1.55\mu$m).

It has been shown by previous researches [73, 65] that adjusting the buffer layer thickness and or the electrode height have considerable effect on the modulator features. Fig. 4.7 show the simulation results for the modulator characteristics as a function of the buffer layer thickness τ and the electrode height t. It is clear that the thicker the buffer layer the lower the microwave effective index is, but at the same time there is an increment of the driving voltage. The second criterion to maximize the bandwidth of the modulator is that the impedance of the device should match that of the signal generator, which is usually fixed at 50Ω. It can be observed in Fig. 4.7(d) that the increment of the electrode thickness produces a decrement of the characteristic impedance of the modulator, that needs to be taken into account in the design and fabrication

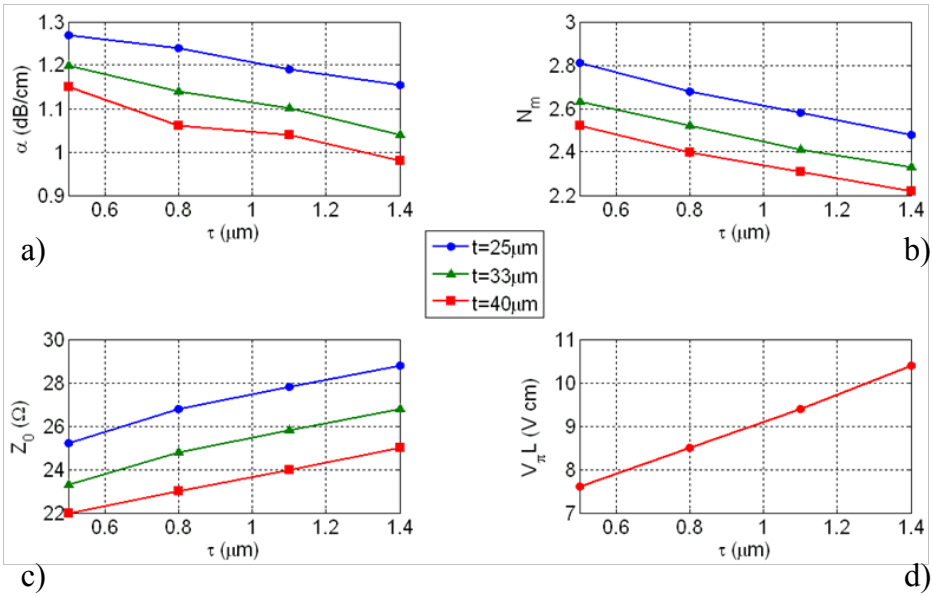

Figure 4.7: Calculated modulator characteristics for the proposed design as a function of the buffer layer thickness τ and taking the electrode high t as parameter. (a) Losses, (b) microwave effective index, (c) characteristic impedance, (d) voltage-length product.

of the electrode transitions. With respect to previous structures of coplanar waveguide (CPW) modulator [58], the proposed layout offers several advantages, summarized in Table 4.2.

Driving voltages (for similar device length) are close to those offered by dual drive structures (two waveguides under two hot electrodes driven by opposite sign voltages), with the advantage of being single drive, hence in the absence of any synchronization issue between two microwave lines. On the other hand the typical single-drive structure in single-domain z-cut has one of the two waveguides under the ground electrode, which induces a lower electro-optic effect due to field spreading compared to the other waveguide under the narrower hot electrode. The result is that the typical driving voltage is about 1.5 times that of a dual-drive structure and 1.4

Structure	Vπ· L (V·)cm	Γ	Chirp(α)	RF drive
$LiNbO_3$ physical limit	≈ 3.6	1	0	Single
Standard CPW [50]	≈ 12	0.3	$\neq 0$	Dual
Dual drive CPW [50]	≈ 8	0.45	Arbitrary	Single
CPW with longitudinal DI [58]	≈ 12	0.3	≈ 0	Single
DI push-pull [4]	≈ 9	0.4	0	Single
Ridge [54, 66]	≈ 6	0.6	≈ 0	Single
Thin plate [69, 74]	≈ 9	0.4	≈ 0	Single

Table 4.2: Comparison of the performances of different configurations.

times that of the proposed geometry.

Device Fabrication

As an experimental demonstration of this type of modulator, a single-drive Mach-Zehnder interferometer was designed and fabricated. The active length of the device was ≈ 40 mm. Ti in-diffusion waveguides were fabricated on a $0.5-$mm thick $LiNbO_3$ crystal. A high-voltage ($>$10kV) pulsed poling (see section 3.2) was performed in order to obtain cross sectional inverted domains (Fig.4.8). After DI, the modulator chip underwent to standard fabrication processes, e.g. silica buffer layer deposition, electroplated thick electrodes (Fig. 4.9), end-faces lapping and polishing. Fig. 4.10 shows the microwave reflection coefficient ($|S11|$) and the corresponding EO frequency response ($|S21|$). From the figure one can see that the electrical reflection is always below -10 dB and the -3 dB EO bandwidth is 13.5 GHz. The corresponding switching voltage is $\sim$2V (measured at 1 kHz). Therefore the modulator could easily be driven with significant extinction by a low-cost Si-Ge driver, which typically provide less than 3V at 10 Gb/s. Fig. 4.11 reports the system measurement setup and the eye diagram obtained for the low-voltage modulator fabricated employing a Inphi 1015EA driver.

The eye opening shows a performance suitable for standard optical communication at 10 Gb/s, including an extinction ratio of 13.65 dB and

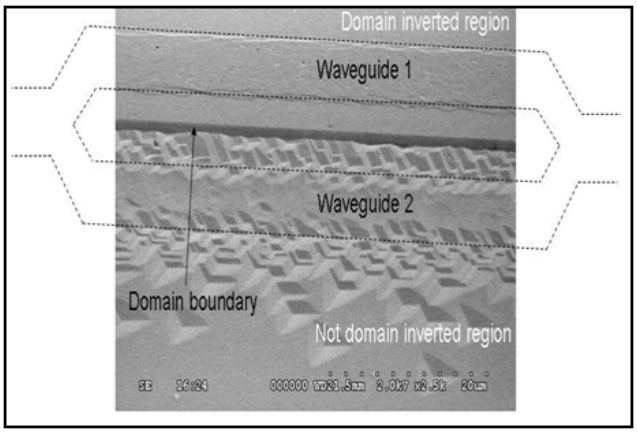

Figure 4.8: Opposite oriented domains in a DI modulator revealed by differential HF etching. z-domains are etched while $z+$ remain intact.

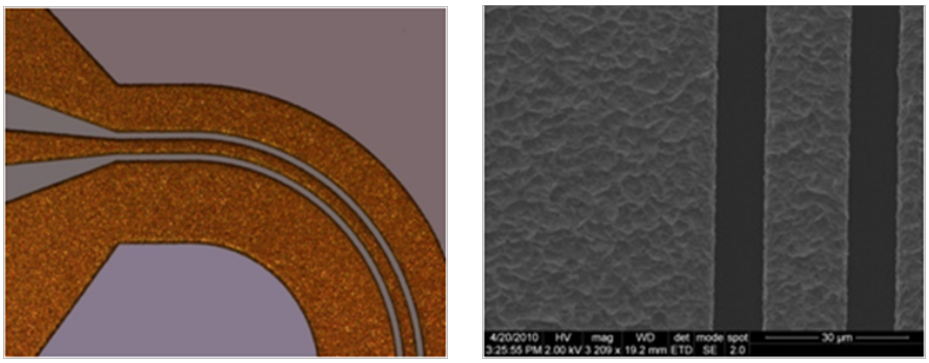

a) b)

Figure 4.9: Thick electroplated electrodes: (a) microscope image, (b) SEM image.

overall optical losses $<$ 2dB at a wavelength of 1550 nm.

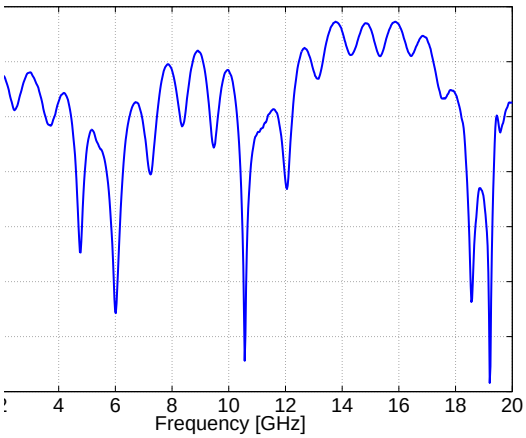

a)

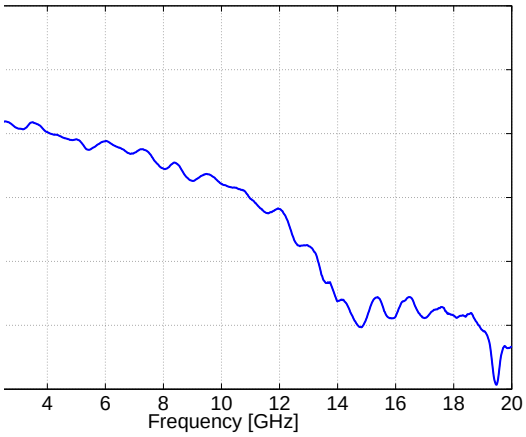

b)

Figure 4.10: (a) DI modulator electrical reflection ($|S11|$) and (b) electro-optic response ($|S21|$).

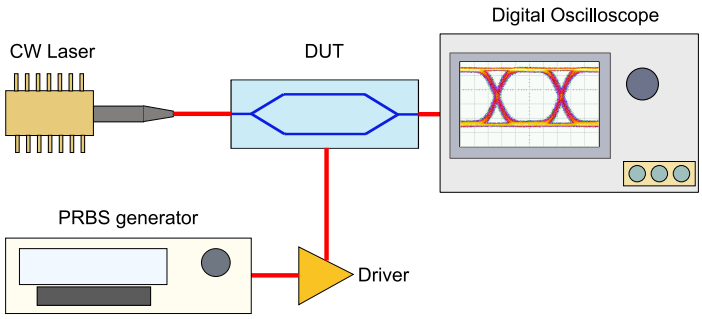

a)

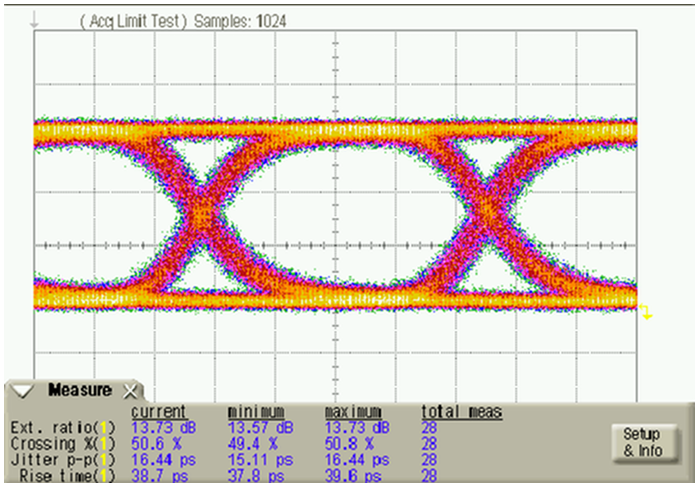

b)

Figure 4.11: Test setup (a) and eye diagram measures showing wide opening at 10 Gb/s (b).

4.5 Advanced Applications

4.5.1 New Modulation Formats

LN optical intensity modulators are key components in current long-haul WDM high-bit-rate optical communications systems. Nevertheless, novel optical modulators using alternative modulation formats and new archi-

tectures are being actively studied in order to match the requirements of next generation systems. On the one hand, these systems will require cost efficiency and adaptability to new environments, such as access networks. On the other hand, a higher capacity over long distance links and core networks will be necessary, primarily due to video applications. Therefore, after years of technology development, the 40 Gb/s is now moving to a generalized deployment phase. Various modulation formats are today employed for 40 Gb/s transmission, with main focus on DPSK and DQPSK, both relying on phase modulation in place of the conventional amplitude modulation. In the DPSK modulation format the information is phase encoded, with an optical phase switch occurring between different bits. Most often, a Mach-Zehnder modulator is employed, where a modulation over 2V causes the phase transitions to occur between two neighboring maxima. In this way, the two states exhibit same (full) amplitude, but they show opposite phase. Since modulation occurs over $2V_\pi$, low driving voltage is essential in order to decrease the power consumption of the complete system. While DPSK is a binary format (i.e. generates one bit per symbol), with DQPSK two symbols per bit are encoded (quaternary format). This allows for considerably better spectral efficiency and brings significant advantage in terms of tolerance to chromatic dispersion and, particularly, to Polarization Mode Dispersion (PMD). To realize the DQPSK modulation, the optical modulator is a key element. This format is generally achieved by employing a nested Mach-Zehnder device, where two MZ modulators are included in a larger interferometer (see scheme in Fig. 4.12). The inner modulators are to be modulated over $2V_\pi$, but at half rate with respect to DPSK. Reported devices are able to deliver 80 Gb/s DQPSK signals using a double drive signal with an amplitude of 6.5V [75, 76]. Similar $LiNbO_3$ devices are being studied also to perform simultaneous transmission of baseband and radio signals on a single optical wavelength. Due to the fast increase of high data rate demands of wireless and wired networks during the last years, it is desirable to merge both into a single shared infrastructure in order to save costs. One possibility is to modulate and transmit RF and FTTH baseband signals using one external modulator. It has been proposed to use a

nested MZ interferometric structure in $LiNbO_3$ for this purpose. In this structure, the RF modulation is implemented in double-side-band carrier-suppressed (DSBCS) amplitude modulation format with a capacity of 622 Mb/s; whereas the baseband signal at 1.25 Gb/s modulated and transmitted using the carrier wave of the same wavelength [77]. Single side-band (SSB) modulation format is also especially useful in optical fiber communication systems. This format requires a narrower operating bandwidth, which makes it adequate for high density wavelength multiplexing. It is also advantageous for long-haul fiber transmission due to less nonlinear optical effects, because of the reduced optical power. One proposed device for this modulation consists of a nested MZ interferometer that works as four parallel phase modulators, driven by signals which are $\pi/2$ shifted [78]. Another approach for SSB modulation employs a single MZ

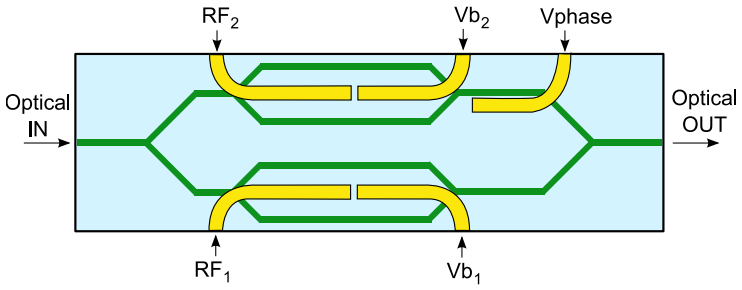

Figure 4.12: Scheme of a DQPSK modulator based on a nested MZ with two indipendent RF inputs (RF1 and RF2) and bias (Vb_1 and Vb_2). A phase shift is applied by the voltage Vphase to set the working point.

interferometer combined with domain inversion (DI) and a resonant electrode. This modulator has a narrow operating bandwidth because of the resonance effect, with a center frequency of 15 GHz. However, the required modulation power is rather small compared to the traveling wave modulators and it is useful for radio-over-fiber (ROF) applications [79]. Designs with a three-branch waveguide interferometer have been recently applied to single-sideband carrier- suppressed (SSBCS) modulation and optical frequency shifting operating at a frequency of 15 GHz. Arbitrary

control of the phase of optical modulation was also obtained by using the DI engineering. These devices are able to notably contribute to ROF systems and long-haul optical fiber communications due to the optimum use of the transmission bandwidth. Moreover, optical frequency shifting is very attractive in precision laser spectroscopy, quantum optics, and optical measurement systems [80].

4.5.2 Integration with tunable lasers and electronics

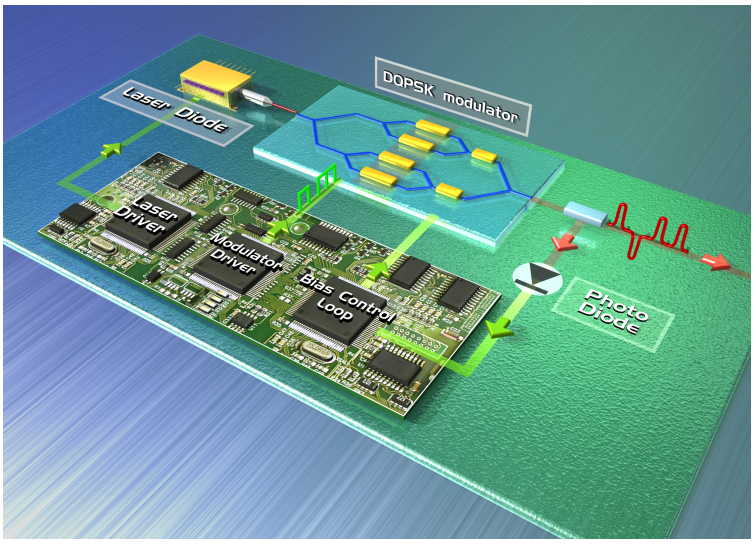

Figure 4.13: Scheme of a DQPSK integrated modulator board comprising also laser source, bias control electronics and driver.

Although reduction in driving voltage can lead to more compact modulators and to an overall cost reduction, packaging costs still account for the majority of device cost. To address this issue there has been in the last years an increasing interest towards integration. The possibility of including several components in the same package also enables more efficient interconnection between the parts and better inter-operability. Lithium niobate modulators lend themselves to integration at several levels. On

one hand they need an electrical input driving signal with amplitude of few volts, which is made available by using an RF amplifier. Integrating the driver amplifier with the $LiNbO_3$ modulator brings a number of advantages. First of all, the design of the modulator and of the driver may be optimized for optimal mutual match including e.g. bandwidth optimization and impedance matching. Moreover, the driver design may be optimized so that the output driver voltage is consistent with modulator requirements with the goal of minimizing power consumption. In this respect, lowering the driving voltage brings a substantial advantage. In addition, the electrical interconnections between driver and modulator may be reduced in number (driver can be wire bonded to the lithium niobate device) and optimized in performances with advantages in terms of reduced loss and electrical reflections, and lower cost. For example, by avoiding the use of the conventional RF connectors between driver and modulator, a cost reduction of few tens dollars per device is achieved. Tunability is also key in today's optical networks. The reason for the interest into tunable wavelengths is twofold. Firstly, tunable sources reduce the inventory as a single part may be employed for any transmission channel as opposed the need for one part number per channel. Secondly, tunable sources pave the way towards reconfigurable networks which allow for extended flexibility in terms of wavelength management and traffic routing, with the eventual advantage of more efficient operation and ultimately reduced operating cost. Also in this respect, lithium niobate modulators find their perfect application thanks to the material transparency across C+L band, in contrast to e.g. electro-absorption modulators which generally limit their operating wavelength range to few channels. Integration of tunable laser with lithium niobate modulator is another trend in today's telecom market where integrated tunable laser-modulator assemblies are already commercially available (e.g. JDSU [81]). Besides reducing costs, a key benefit of laser-modulator integration lies in the reduced space occupancy with respect to the discrete approach. This facilitates the development of small form factor line-cards and transponders, in line with today's general effort aiming at reducing optical interface dimensions.

Chapter 5

Integrated electric field sensor for high voltage measurement

5.1 Introduction

Over the last few years, the need for intense electromagnetic field sensing technology has widely increased, playing a critical role in various scientific and technical areas, especially in the power industry and in electromagnetic compatibility measurements. Various studies have been carried out concerning electric field emission from transmission lines and the effects on people living or working close to these sources. Nowadays, the assessment of the electromagnetic compatibility of electric devices is needed to satisfy stringent emission requirements. For more efficient and reliable operation of ultra high voltage power systems, the electric field strength, in high voltage machines must be accurately measured. In electrostatic applications, it is mainly DC electric field which is applicable. The presence of electrostatic charges is a major concern in the process industry where a build-up of the charge could lead to hazards to operators handling material or equipment or to a possible explosion or fire. In microelectronic industry, the measurement of electric fields is important in the manufacture of silicon devices as stray charge can destroy sensitive circuits. In medicine, it was found that complex electronic devices

may interfere with electromagnetic fields. Even devices implanted in human bodies such as pacemaker may be influenced by surrounding fields. Furthermore, electric, magnetic and electromagnetic fields interact with biological systems. In medicine the interaction can be employed beneficially for diagnosis and therapy but can be harmful as well. Conventional electric field meters typically use conductive parts, which can interfere with the field to be measured, and are very sensitive to electromagnetic noise. Moreover, frequency bandwidth limitations and 50Ω characteristic impedance in the case of RF waveguide based sensors limit the scope of applicability of such technology. Electro-optic (EO) devices present several intrinsic advantages compared to their electronic counterparts such as noise immunity, feasibility of electrode-free operation and consequently the possibility of operating even in harsh or dangerous environments.

5.2 Electric Field Optical Sensors: State of the art

At the beginning of the 1970's, researchers started to work on optical methods for voltage and current measurement in high voltage environment [82, 83, 84], as an attractive alternative to conventional electric field meters, e.g. potential transducers (PT) or current transformers (CT). Most optical sensors developed in the 1970's used bulk electro-optic or magneto-optic crystals and were interrogated using free space links (Fig. 5.1). New materials such as bismuth silicon oxide (BSO) and bismuth germanium oxide (BGO) became available. In [85] the authors realized the advantages of these isotropic cubic crystals and in 1980 demonstrated a high intensity electric field sensor based on BSO crystal. Compared to uniaxial crystals (crystals with a rotational index ellipsoid and natural birefringence), such as Lithium Niobate ($LiNbO_3$), Lithium Tantalate ($LiTaO_3$) and potassium dihydrogen phosphate (KDP) group of crystals, the isotropic BSO and BGO crystals do not possess the natural birefringence or pyroelectricity which significantly influences temperature stability. Thus a remarkable temperature stability of $\pm 3\%$ was achieved over

the range from 15°C to 70°C. The electric field was measured in the range from 15 to 200kV/m with linearity better than 1%. This sensor was improved by the same research group later in 1982 [86]. It was found that the temperature dependence of the crystal optical activity can be decreased by properly choosing the length of the crystal. This improved the temperature stability to $\pm 0.2\%$ over the temperature range from 15°C to 70°C. The rapid development of electro-optic and fiber optic technologies has brought to make compact field sensors using integrated optics technology. Compared to bulk electro-optic sensors, integrated devices can offer some advantages like size reduction and simplicity of design with no need for lenses, quarter-wave plate and polarizers [87, 88]. Since the piezoelectric resonances can be shifted up to higher frequencies by decreasing size of devices, the integrated optics based sensors can work as a broad band device.

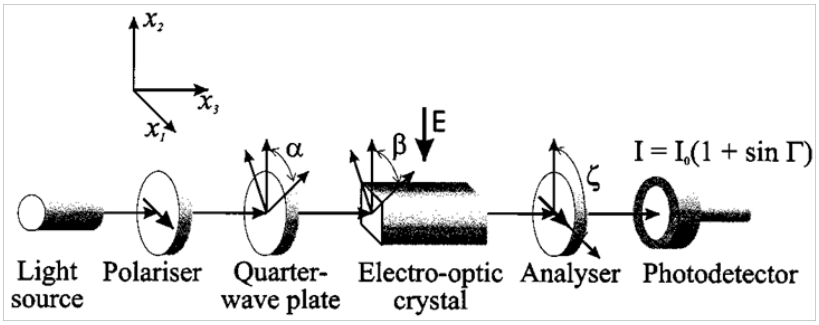

Figure 5.1: Bulk Electro-optic Sensor [89].

So far, several configurations of EO sensors based on $LiNbO_3$ have been reported, mostly based on waveguide interferometers [90] or bulk polarization/phase rotation in a piezoelectric crystal [91, 92]. The latter approach requires phase noise reduction control techniques that are typically expensive to implement and may raise long-term stability issues. On the contrary, waveguide-based sensors directly convert the electric field value into an optical power variation, thus simplifying the interrogation system and potentially lowering the cost. In this context, Mach-

Zehnder interferometers (MZIs) are usually employed for their high sensitivity. However, they typically require additional metal electrodes and controlled biasing to work properly [93, 94]. To overcome some limitations, schemes without any conductive parts based on ferroelectric poling of the two interferometer arms have been proposed [95, 96]. Moreover, especially for MZI, maximum measurable field intensities are typically below the fields present in some installations, like electric plants or railways electric network. In these systems, very bulky sensors need to be employed [97]. Alternative designs are based on Bragg grating in $LiNbO_3$ [98]. In the past years, cut-off devices have already been proposed in $LiNbO_3$. In particular, the use of waveguides at cutoff was proposed for modulation in the field of optical communications [99, 100, 101] and sensing [102]. The use of $LiNbO_3$ electro-optic sensors is also attractive for wide-band sensing schemes, based on the high frequency response of such devices, reaching potentially up to several GHz. Sensing wide-band electric fields is currently a potential application in optoelectronic instrumentation, aiming to measure static and dynamic electric fields in electric power equipment, generation and distribution of electrical power, telecommunication equipment and facilities, medical applications, etc.

5.3 Objectives of this work

The aim of this research is to investigate the possibility of precise measurement of wide-band high electric fields using a passive, all dielectric and Electro Magnetic Interference (EMI) immune sensor. The sensor should use the linear electro-optic effect in $LiNbO_3$. A novel approach is proposed for electric field sensing. It is based on an annealed proton-exchange waveguide at cut-off and on micro-structured domain engineered ferroelectric crystal. Moreover, the device should be simple, low cost and without the drawbacks of interferometric and metal cover structures. These features should make it suited for use in harsh conditions - e.g. power stations and transmission lines - without any danger for the operator or risk of damage of the sensor head.

5.4 Considerations

The literature review revealed that the most common optical techniques for electric field measurements are based on the electro-optic and piezo-electric effects. It was shown that techniques based on Mach-Zehnder interferometer-schemes can be very sensitive to DC and low frequency field, however, their temperature stability is poor and they require a bias control to work properly. On the other hand, probes based on the electro-optic effects may have very good temperature stability. Their sensitivity is, however, lower. Taking into account the importance of the sensor stability to environmental changes, size of the sensor, disturbance of the measured field and complexity of the output signal processing design, the linear electro-optic effect has been chosen for the electric field sensor to be realized.

5.5 Effect of the internal space charge

One of the most important criteria for building a DC field sensor is the requirement of a high resistivity of the electro-optic crystal and an elimination of the photoconductivity effect in the crystal. When a crystal of a finite resistivity is exposed to a static electric field, the free charge carriers start drifting along the electric field lines and accumulate on the crystal boundaries. The accumulated space charge generates an electric field with orientation opposite to the original internal field. Therefore, the resultant field, which is a superposition of the original field and the field of accumulated space charge, continuously decreases. The speed of this process depends on the density of free charge carriers which is proportional to the crystal conductivity [103]. The macroscopic internal field $E_{int}(t)$ in a crystal exposed to a static external field $E_{ext}(t)$ decreases exponentially as:

$$E_{int}(t) = E_{int0}e^{\frac{t}{\tau}} = E_{int0}e^{\frac{\sigma}{t\epsilon_r\epsilon_0}} \tag{5.1}$$

where ϵ_r, ϵ_0 are the crystal relative permittivity and permittivity of

vacuum respectively, σ is the crystal conductivity and

$$\tau = \frac{\epsilon_r \epsilon_0}{\sigma} \tag{5.2}$$

is the charge relaxation time constant. Since the electro-optic effect is caused by the internal electric field, the sensor output does not correspond to the measured static field but to the decaying internal field. It is evident that if the crystal is not to be rotated, the conductivity of the electro-optic crystal needs to be considered in the first place. Its low value can make the crystal unsuitable for low frequency and DC field sensing. Being $LiNbO_3$ an insulator, its conductivity depends on thermal excitation of free charge carriers, and on the concentration of lattice defects. Another source of free charge carriers inside crystals is represented by the photoconductivity effect. In this case the excitation energy necessary to generate the carriers is supplied by a flux of photons with energies $h\nu$, where ν stands for frequency of light and h for the Plank constant. In intrinsic materials, the photon energy must be enough to excite electrons from valence band to the conduction band. The wavelength λ_c of the light at which the photon energy is equal to the band gap energy defines intrinsic absorption edge. At wavelengths $\lambda < \lambda_c$, the laser radiation is strongly absorbed in the crystal. This strong absorption is accompanied by increase in conductivity due to the photoconductivity effect. The critical wavelength represents a limit for the wavelength of optical sources used in the sensor [104]. The relaxation time constant τ, is used to estimate the effect of crystal conductivity on an electro-optic sensor at DC and low frequencies. Application of the Laplace transformation on a system characterized by time constant τ as in 5.2 gives the cut-off frequency of $f_{3dB} = 1/2\pi\tau$, at which the sensor response is decreased by 3dB. Table 5.1 [103] shows the conductivity of $LiNbO_3$ compared with selected cubic crystals, together with the critical wavelength λ_c and the time relaxation constant τ.

The low values of time constants imply that crystals like gallium arsenide (GaAs), gallium phosphide (GaP) and zinc selenide (ZnSe) are theoretically not suitable for DC and low frequency applications. ZnS, ZnTe and CdTe have relatively high resistivity but they are still unsuitable for DC applications. They can be used for low frequency applications

	$LiNbO_3$	GaAs	GaP	ZnS	ZnSe	ZnTe	$Bi_4Ge_3O_{12}$	BSO	BGO
symmetry	3m	43m	43m	43m	43m	43m	43m	23	23
λ_c[nm]	350	920	552	345	480	549	-	394	394
σ[S/m]	1E-16	1E-5	-	1E-8	1E-6	1E-7	1E-13	1E-9	2E-12
ϵ_r	85	13.2	10	8.3	9.1	10.1	16	40	56
f_{3dB}	2E-8	14469	-	11	198	18	1E-4	0.56	6E-4
τ[s]	7E16	1E-5	-	1E-2	8E-4	9E-3	1380	0.28	248

Table 5.1: Comparison among $LiNbO_3$ and selected electro-optic crystals. Point group symmetry, critical wavelength λ_c, specific conductivity σ, relative permittivity ϵ_r and charge relaxation time constant τ.

because of their relatively low limit frequencies but the decay of the DC internal electric field due to the conductivity effect is still very fast. On the contrary, $LiNbO_3$ has high enough resistivity, which makes it suitable for DC and low frequency measurements as well as wide band operations.

5.6 Device Design

The previous section reviewed the material properties and it was shown that $LiNbO_3$ is an appropriate crystal suitable for wide-band electric field sensing. This section presents the proposed device design, which is sketched in Fig. 5.1 [105]. An annealed proton exchange (APE) waveguide fabricated in z-cut $LiNbO_3$ is centered in a domain inverted region. On the application of an external electric field parallel to the z axis of the device, the refractive index in the central inverted domain decreases while it increases in the external domains.

Thus, the optical mode will broaden so that, after a sufficient propagation length, a loss is produced due to a mode-profile mismatch of the guided modes between active and passive regions. The index difference change between positive and negative domains is given by:

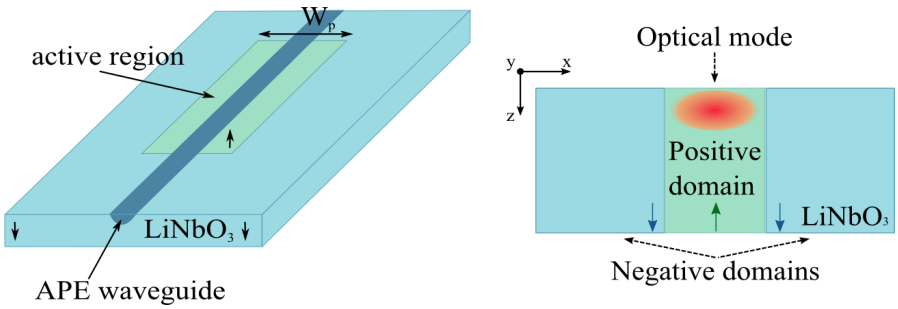

Figure 5.2: *Top view* and cross-section schematics of the electric field sensor. APE waveguide is centered in the domain-inverted region of width W_p.

$$\Delta n_{\pm} = 2 \cdot \frac{n_e^3}{2} r_{33} E \tag{5.3}$$

where E is the intensity of the external electric field along the z-axis, $n_e = 2.14$ and $r_{33} = 30.8$ pm/V are the refractive index and the electro-optic coefficient along the z-axis, respectively, [106]. Limiting the external field E below the coercive field of $LiNbO_3$ (E_c= 21.4 MV/m), from equation 5.3 an index change ($\Delta n_{\pm}$) of 6.037×10^{-3} can be calculated for $E = 20$ MV/m. Taking into account the configuration and limitation of the experimental characterization set-up described hereafter (see Fig. 5.6), the behavior of the devices were numerically simulated for different waveguides and poled region parameters. The device waveguides were formed by APE technique (section 3.1), which leads to an increase of the refractive index in the exchanged region [24]. The y-propagating channel waveguides in z-cut $LiNbO_3$ had different width, (ranging from 3-7μm) in order to be near cut-off at the optical wavelength of 1.55 μm, and to give the adequate dynamic range for high electric field detection. The increased refractive index contour is given by:

$$n(x,z) = n_{sub} + \Delta n_e \left[f(x) g(z) \right] \tag{5.4}$$

where

$$f(x) = \frac{1}{2}\left[erf\left(\frac{w-x}{d_x}\right) + erf\left(\frac{w+x}{d_x}\right)\right] \tag{5.5}$$

and

$$g(z) = exp\left[\left(-\frac{z}{d}\right)^2\right] \tag{5.6}$$

where n_{sub} is the extraordinary refractive index of $LiNbO_3$, Δn_e is the maximum index change due to proton exchange, $2w$ is the mask width and d_x and d are the diffusion lengths in the x and z directions, respectively. The behavior of the sensor was studied, via a beam propagation method (BPM) simulation software, along with different waveguide widths and depths, while varying the width of the central poled region (Wp= 6, 10, 15, 20 μm) for the set of channel waveguides considered above. The numerical simulations indicated that the optimum parameters in order to obtain high sensitivity for strong electric fields correspond to a poling region of 10 μm width and 3.5 μm wide waveguide (Fig. 5.2 and Fig. 5.3).

5.7 Device Fabrication

The devices, having a 20mm overall length and poled (active) region ranging from 2.5 to 10mm, were fabricated starting from domain inversion by electric field poling. A 3.3 μm-thick layer of resist AZ4533 was spun on the z- face and used as an insulator layer after patterning and hard-baking at 140°C for 1 hour. The inverted domains were then revealed via differential etching in hydrofluoric acid for alignment purposes. The after-etching height difference between z+ and z- domains was around 90 nm. Fig. 5.5 shows the poled domains and illustrates the position of the waveguides in their center. According to the simulations, the etching step didn't affect the optical mode even in the presence of an electric field. A 200-nm-thick aluminum mask layer was patterned on the substrate and deposited via lift-off process using a lithography mask containing sets

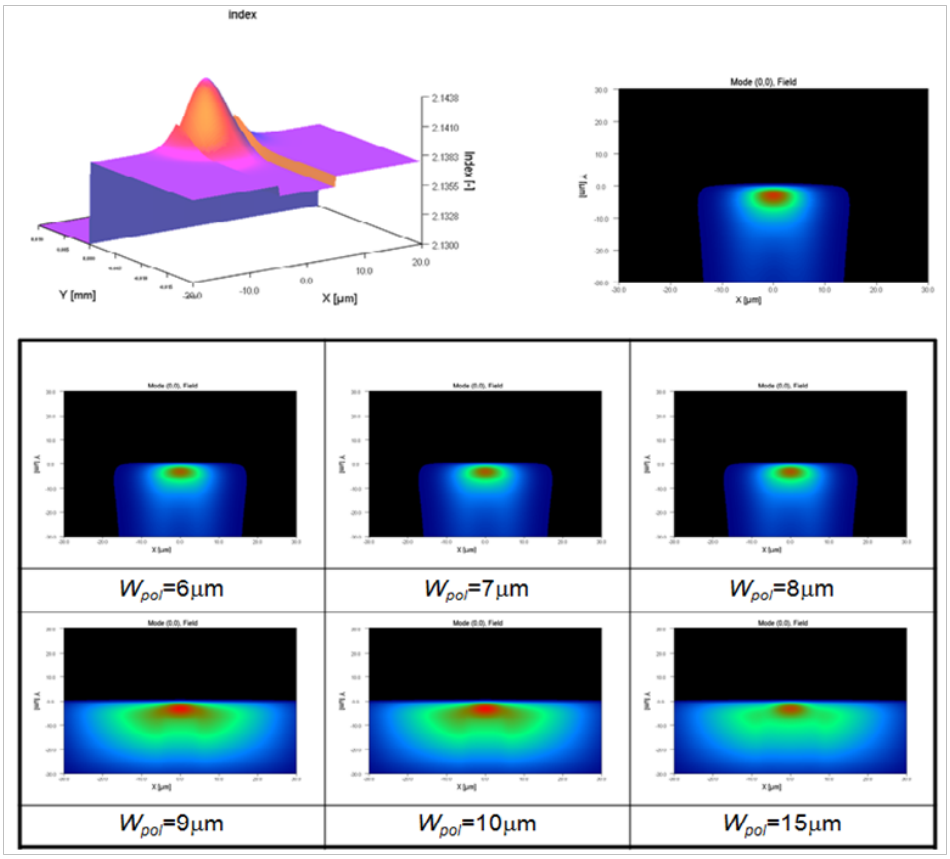

Figure 5.3: BPM simulations of the optical mode intensity for a 3.5μm width waveguide for different domain region width W_p.

of channel waveguides that were aligned with the center of the inverted regions. The samples were then immersed for 30 min at 210°C in benzoic acid buffered with 1% of lithium benzoate and then annealed in air for 11 hours at 360°C. This procedure produce the formation of α-phase proton exchange (PE: $LiNbO_3$) waveguides with extraordinary index step $\Delta n_e \approx 0.02$ on the surface and smooth Fermi-like profiles with effective depths in the 4-5 μm range. The aluminum mask was then removed, the samples diced and the faces were end polished.

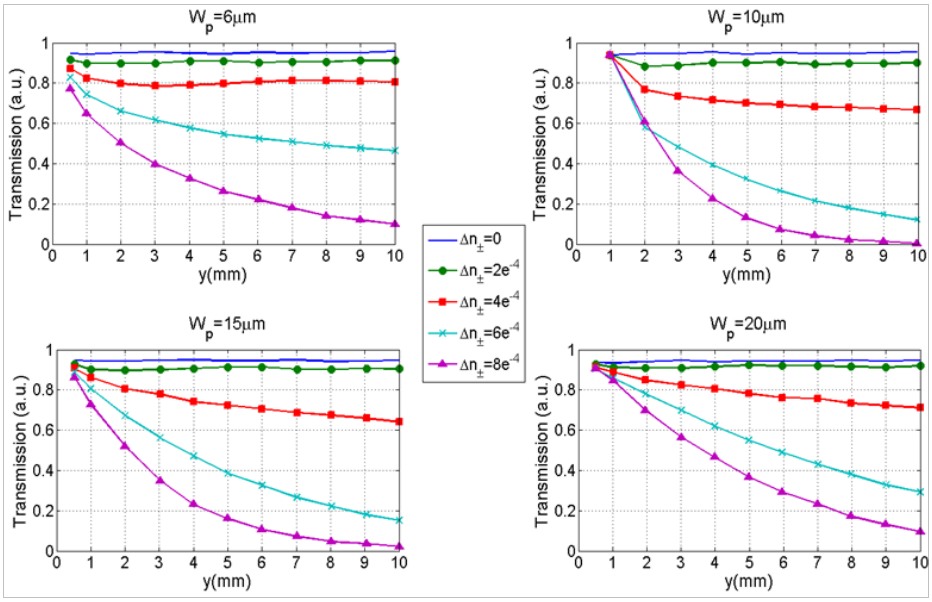

Figure 5.4: BPM simulation of the transmission power versus the length of the active region for different domain region width W_p taking $\Delta n\pm$ as parameter.

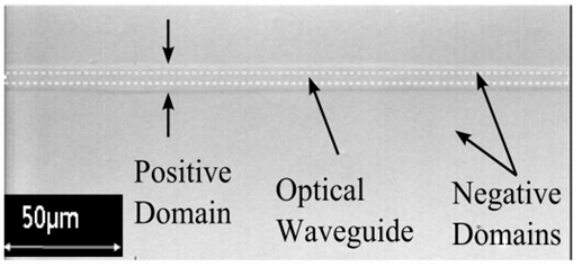

Figure 5.5: SEM image showing the domain inverted regions revealed by HF differential etching and position of the optical waveguides.

5.8 Device Characterization

5.8.1 Low Frequency measurement

Firstly, the device with 10 mm poled region was tested at low frequency using the experimental set-up shown in Fig.5.6(left). The sensor behavior was characterized without and with the presence of air-$LiNbO_3$ interface. In the first case, a silica buffer layer was deposited on top of the waveguide and the sample was then held between two electrode plates. The light from a 1mW tunable laser centered at a wavelength (λ) of 1.55μm was coupled into the sensor through a standard fiber. A polarization controller allowed choosing the correct light polarization in order to excite the TM mode of the channel waveguide. The electric field was then applied to the capacitor by a high-voltage amplifier.

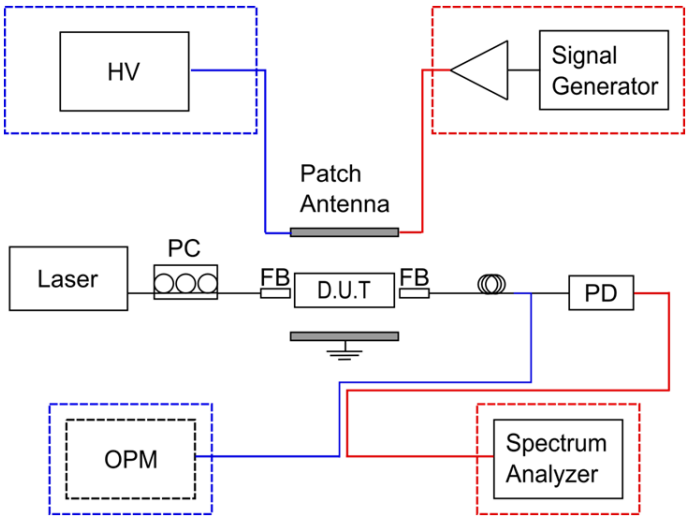

Figure 5.6: Block diagram of the test set up. Left (blue): DC test configuration. HV, high voltage amplifier, OPM, optical power meter. Right (red): High frequency configuration. HP Signal Generator, Hamamatsu Spectrum Analyzer. PC, polarization controller, FB, fiber block, PD, photo detector.

In this setup the sensor was aligned with its poling axis parallel to the linearly polarized electric field. Fig.5.7 shows the optical transmission change as a function of the internal field in the $LiNbO_3$ waveguide region, together with simulations obtained for different poling region widths. It can be seen that there is a good agreement between measured and calculated values and up to a maximum field (limited by the set-up) of 2.6 MV/m. The optical power meter used for the measurements was an ILX Lightwave FMP-8210 (resolution $\pm$0.001dB), which allows to stably measure optical power increments of $\pm$0.01 dB. From these parameters

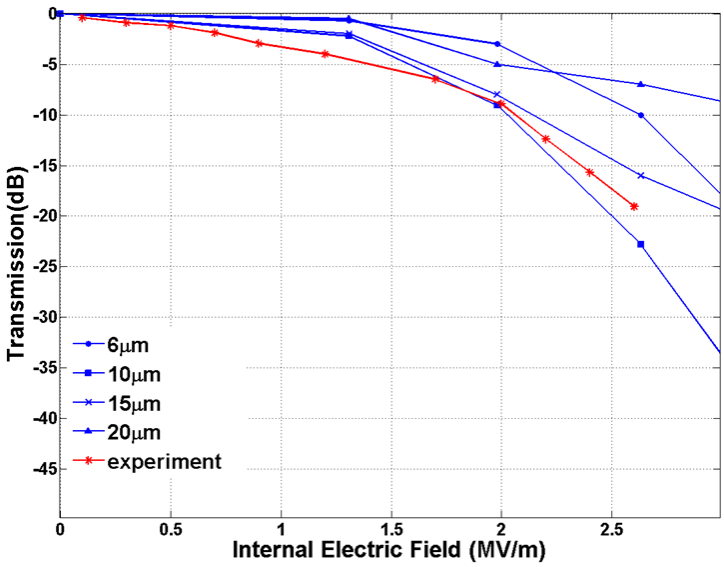

Figure 5.7: Experimental results (red) of DC measurement compared to the simulated behavior of the device (blue) for different poling region widths for a waveguide of 3.5 μm. The active (poled) length is 10mm.

and the collected data, a minimum detectable DC field of about 20kV/m can be estimated. In order to understand the possible influence of fringe effects given by the parallel plate setup, the dependence of the sensor's response on the length of the poled regions was also tested. As shown

in Fig.5.8, the sensitivity monotonically depends on the length. This feature gives the possibility to tailor the device sensitivity to different electric field ranges, in order to fulfill the various requirements that might arise in different types of applications.

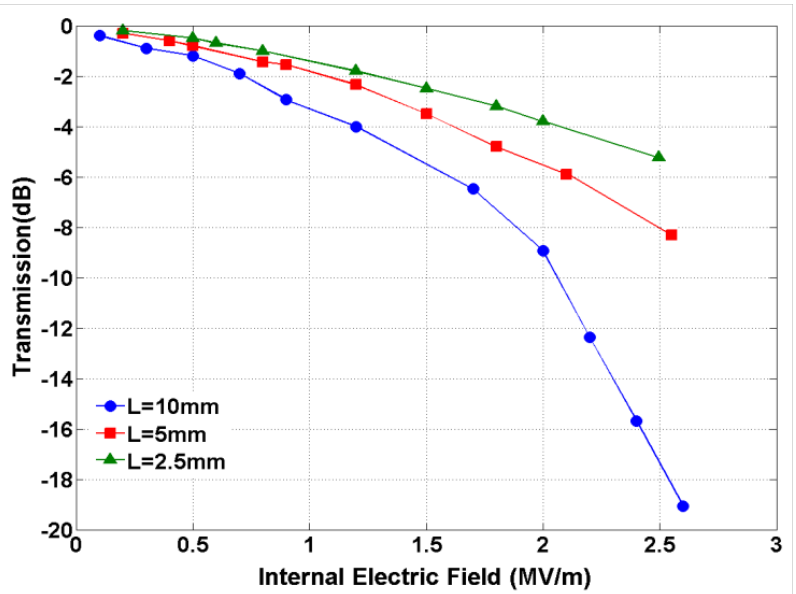

Figure 5.8: Optical transmission vs. internal electric field for three different lengths of active region.

Sensor Calibration

When the optical waveguide is used as a dielectric sensor, no electrodes are associated with the crystal and the electric field is present in the dielectric environment (most commonly air, n = 1), surrounding the $LiNbO_3$ crystal. As already said above, at very low frequency (below 1 kHz), the interface between air and $LiNbO_3$ may play an important role due to the low surface conductivity of the substrate and its high permittivity. For this reason, the device was tested in the presence of an air gap and com-

pared it with the previous results where the metal electrodes were in contact with the $LiNbO_3$ chip, apart from a 50nm thick silica buffer layer. Fig.5.9 presents the experimental set-up used. The electric field was generated by applying a high voltage to a set of parallel metallic plates. The electro-optic sensor was placed between the plates, but not in contact with them, as an air layer of thickness (d_{air}) separates the upper plate from the $LiNbO_3$ crystal of thickness (d_{LiNbO_3}). As the plates were wide enough (50 mm) and the optical waveguide is 3.5 μm wide, the sensed electric field was considered uniform in the waveguide. As illustrated in Fig.5.9, the electric field in the air E_{air}, finds a boundary condition on the surface of the electro-optic sensor. The discontinuity is determined by the permittivity of the air ($\varepsilon_{air} = 1$) and of the crystal ($\varepsilon_{LiNbO_3} \sim 35$), respectively.

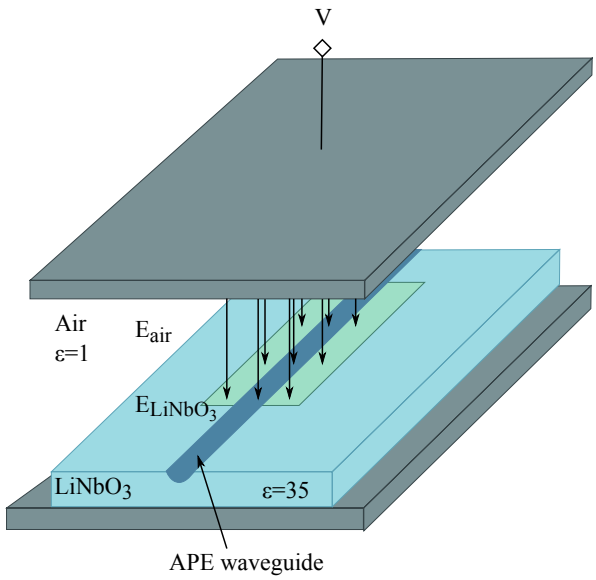

Figure 5.9: Dielectric Electric Field Sensor.

$LiNbO_3$ crystal as $V = V_{air} + V_{LiNbO_3}$. The electric field across the electro-optic crystal is:

$$E_{LiNbO_3} = \frac{V_{LiNbO_3}}{d_{LiNbO_3}} \tag{5.7}$$

As the electric field is perpendicular to the crystal surface and considering the boundary conditions between two dielectric media, the relationship between the normal electric fields is:

$$\varepsilon_{air} E_{air} = \varepsilon_{LiNbO_3} E_{LiNbO_3} \tag{5.8}$$

In the optical waveguide, the sensed electric field E_{LiNbO_3} is given as:

$$E_{LiNbO_3} = \frac{\varepsilon_{air}}{\varepsilon_{LiNbO_3}} E_{air} \tag{5.9}$$

The sensed electric field is ~ 35 times weaker than the electric field in the air layer over the sensor surface. The measurement performed for an air gap d_{air}=50μm is shown in Fig.5.10. The sensitivity of the device, scaled with respect to the calculated internal field, is increased in the presence of an air gap, thus indicating the presence of interface effects, possibly surface charges that partly compensate the induced bound charges in the dielectric ($LiNbO_3$) region. In other words, the screening makes the *real* internal field larger than the *calculated* one.

For this reason, in a practical case, a calibration prior to the measurement of the field is needed, similarly to what is reported in [103, 89].

5.8.2 High Frequency measurement

The high-frequency testing setup is schematically shown in Fig. 5.6(right). The optical interconnections and laser source are identical to the ones used in the DC measurements, while the electric setup has been designed to measure frequencies around 1 GHz. The receiving part included a wideband photo detector (Thorlabs PDA8GS with BW of 8GHz) coupled to a low noise RF amplifier (Mini-Circuits 40dB gain with BW of 1100 MHz) and an RF Spectrum Analyzer. The RF signal was supplied by an HP8642 signal generator and radiated by a micro strip patch antenna designed to have the fundamental resonance at 1.1GHz. Elimination of RF spurious peaks in elements such as the laser and the photo receiver was ensured by shielding the components and separating them from the RF source by tens of meters.

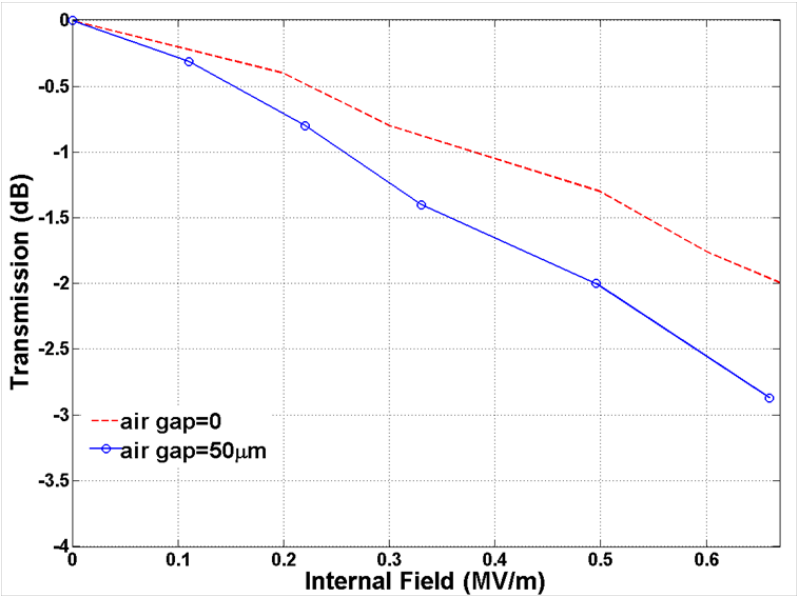

Figure 5.10: Effect on the measurements of air gap between electrodes.

A typical spectrum of detected RF is shown in Fig.5.11, showing a clear peak at 1.1 GHz for an electric field E=14kV/m. The dependence of the modulated light intensity on the applied electric field intensity is plotted in Fig.5.12. It can be seen that the device exhibits a linear dynamic range greater than 60 dB, with a responsivity equal to 0.96 dBm/dBm. A minimum detectable electric field of 19V/m (rms) is obtained with resolution bandwidth of 100Hz, and a span of 20 kHz. Due to limitations of the signal generator and the setup, the strongest electric field we were able to measure was 23.6 kV/m. Higher frequencies could not be tested due to BW limitation of the power amplifier.

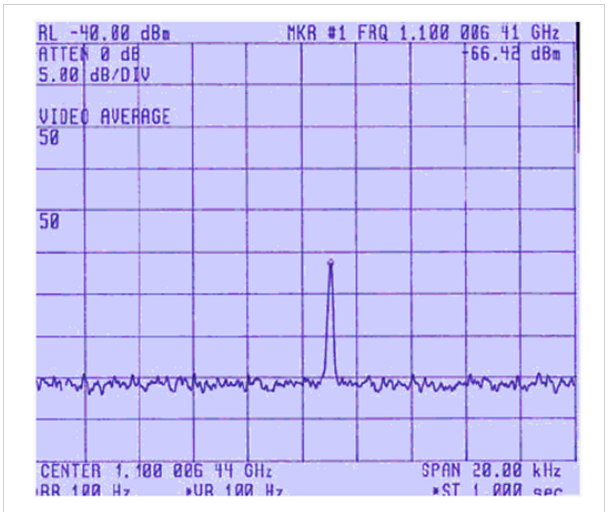

Figure 5.11: Photodiode response for an electric field oscillating at 1.1 GHz. RF spectrum for E=14kV/m. A clear peak is shown.

5.9 Application of room temperature bonding to high-voltage optical sensing

In this section we demonstrate the application potentials of the bonding technique proposed in section 3.3 [107], for the fabrication of a high-voltage field sensor. The scheme of the proposed device is sketched in Fig. 5.13. An APE y-propagating waveguide in z-cut $LiNbO_3$ is designed to be near cutoff at the working wavelength (λ=1550 nm) and centered in a domain inverted region of width Wp=10 μm. The waveguide has a width of 3.5 μm and a depth of around 4 μm, where the vertical profile is assumed to be half-Gaussian with a refractive index increment of around 0.02. Another lithium niobate substrate is afterward bonded on top of the waveguide.

The application of an external electric field parallel to the z-axis of the device causes an increment in the refractive index in the central inverted domain, while a decrease in the external domains. The oppositely domain

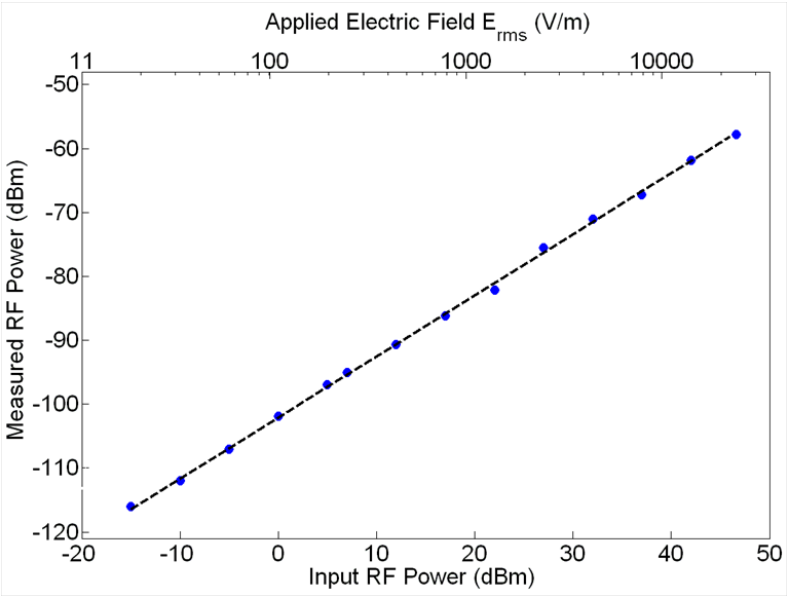

Figure 5.12: Dependence of detected RF peak power against applied field.

inverted regions on the side of the waveguide are limited longitudinally. The device, having a 20 mm overall length and side poled (active) region of 10 mm, has been fabricated following the steps described in section 4.7. Subsequently, another 500 μm thick $LiNbO_3$ substrate was bonded on top of the waveguides by means of the surface activation method described in the chapter 3.3. The sample was then diced and the faces were end polished. We tested the electro-optic device response at low frequency using the experimental setup shown in Fig.5.6(left). Aluminum electrodes were deposited on the top and bottom surfaces to provide an accurate and measurable electric field across the substrate during the tests. From the measurements, it was found that no significant optical losses are introduced by the bonding process. Moreover, an insertion loss of about 1.5 dB per facet was measured. Fig.5.13 shows the measured optical transmission change as a function of the applied electric field in the $LiNbO_3$ waveguide, compared to the fabricated unbounded sensor response described

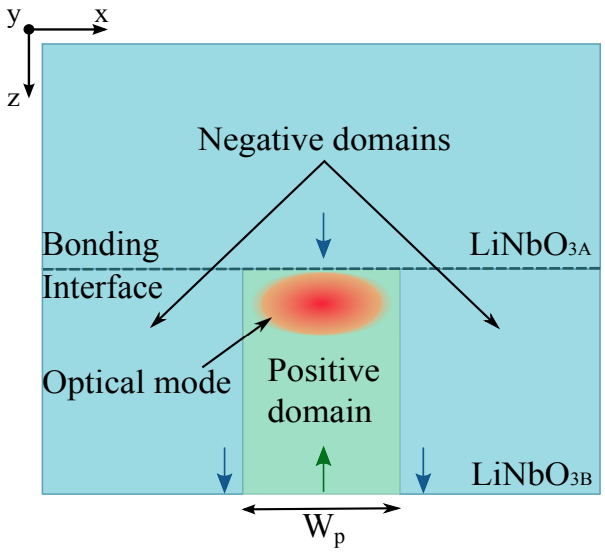

Figure 5.13: Cross-section of the proposed electric field sensor. The APE waveguide is centered in a domain inverted region of width W_p = 10μm, with lateral regions of opposite domains. A LiNbO3 substrate with domain orientation as that of the waveguide is bonded on top through the technique described in chapter 2.

above. It can be seen that the sensitivity improves and we were able to estimate a minimum detectable field of 14 kV/m. The maximum detectable field in the experiments was limited by the measurement setup although in principle it could be as high as the coercive field of $LiNbO_3$. Taking into account that the electric field across the electro-optic crystal is given by:

$$E = \frac{V}{d} \tag{5.10}$$

where V is the voltage applied to the parallel plates of the capacitor and d is the $LiNbO_3$ thickness; it is possible to increase the sensing range by thinning down the substrate layer. Bonding of the device on other substrates (like SiO_2) and subsequent thinning down could reduce the ca-

pacitance of the overall device and make it suitable for RF electric field testing.

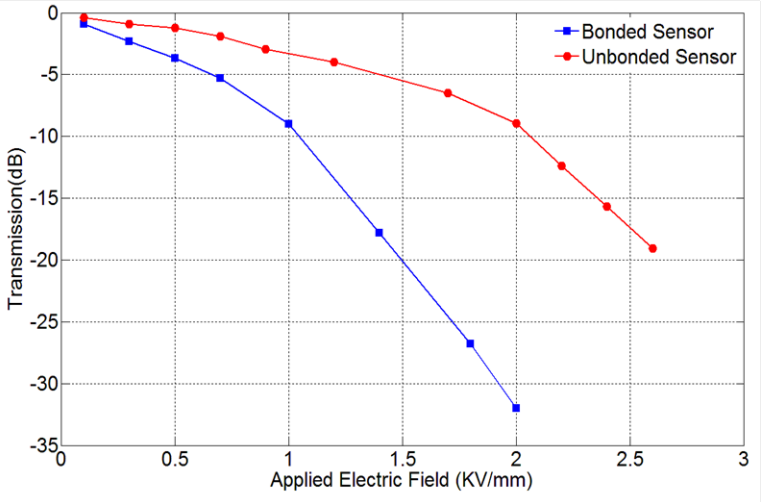

Figure 5.14: Experimental results of DC-measurement for the bonded electric field sensor compared to the unbounded optical sensor. Both devices are formed by a cut-off waveguide of 3.5 μm width and an active (poled) length of 10 mm.

5.10 Summary

It has been demonstrated that Lithium Niobate can be used as a sensing element in DC field sensor. Sensing schemes based on MZ interferometer can be really accurate with the drawback of a bias control to work properly. Two new devices have been fabricated through the micro-fabrication techniques developed during this work. Device features allow operating the sensors without the use of any metal antenna, making them suitable for use in power stations and transmission lines.

Chapter 6

Conclusions

The aim of this work has been the development and exploitation of micro-nano fabrication techniques for next generation integrated devices in Lithium Niobate for optical communication and sensing. This thesis was motivated by mid-term market trends in optical communication and sensing, as described in the introduction and fueled also via industrial collaborations that the group has been having with two leading companies, Avanex Corporation (now Oclaro Inc.) and ABB.

6.1 Main achievements

6.1.1 Development of micro-nano fabrication techniques

In the first part of this thesis, the main properties of $LiNbO_3$ have been discussed. The material presents an attractive combination of properties and allows several waveguide fabrication techniques, such as proton exchange (PE) and titanium in-diffusion.

- A new method for PE waveguide fabrication over 3 inch z-cut $LiNbO_3$ wafers was presented. Particular attention has been paid to the set-up design in order to guarantee a good homogeneity over the entire substrate area. The standard deviation of the refractive index

increment was of the order of $6 \cdot 10^{-4}$. Therefore, the procedure was used in the design of low-loss waveguide based devices.

- Poling of lithium niobate crystals (PPLN) by means of an electric field was developed, now available over up to 4" substrate. Fine tuning of poling structures with high resolution ($< 1\mu$m) has played a central role in current research and it has made possible the development of several devices where the domain boundaries were very close to the waveguides.

- A novel method to obtain room temperature bonding of $LiNbO_3$ to $LiNbO_3$, $LiNbO_3$ to Si and $LiNbO_3$ to fused SiO_2 was developed. The effect on the $LiNbO_3$ surface free energy of chemical cleaning and plasma activation treatments was systematically investigated. The results allowed an optimal procedure to obtain strong bonding at room temperature. The high strength of the bonding was confirmed by the fact that the hybrid materials could withstand mechanical dicing, with the $LiNbO_3$ layer lapped and optically polished down to 10 μm thickness, without any sign of damage. Both bonding and thinning processes for hybrid materials are enabling technologies for a new generation of high performing and compact integrated optical devices.

6.1.2 Low voltage DI waveguide modulator in $LiNbO_3$

A micro-structured electro-optic waveguide $LiNbO_3$ modulator was demonstrated in the thesis. It is based on the use of domain inversion in order to enhance the electro-optical bandwidth - driving voltage ratio (BW/V_π figure of merit). The work investigated the impact of using domain inversion engineering for transversal modulator section. It was experimentally demonstrated the feasibility of a modulator with a switching voltage of ~ 2 V and a bandwidth of 15 GHz, suitable for inexpensive ultra-low-voltage Si-Ge drivers. Besides, system measurements demonstrated the good performance in terms of extinction ratio (> 13dB) and

wide opening that make the device suitable for 10 Gb/s optical fiber transmission.

6.1.3 Electrode-free sensor in *z*-cut $LiNbO_3$ waveguide

An all-optical electric field sensor in $LiNbO_3$ based on a waveguide near cut-off and domain inversion was demonstrated. The device was fabricated through electric field poling and proton exchange waveguide formation. Moreover, the proposed device allows operation without any electrically conductive material on the chip nor in its surroundings. In the experiments, it was possible to measure electric field strengths as high as 2.6 MV/m at low frequencies. The device has been also tested at 1.1 GHz and an electric field with intensities ranging from 19 V/m to 23 kV/m was measured. The resulting linear dynamic range was greater than 60 dB. The sensitivity of the device can be adjusted-decreased or increased-to fulfill specific application requirements in terms of detectable field ranges by tailoring the waveguide parameters. A straightforward improvement of the sensitivity can be achieved by reducing the effective index of the waveguide by means of the annealing. It has been shown that the use of bonding technique is an effective mean to increase sensor sensitivity at DC. A domain inverted bonded sensor was characterized and it was able to measure field as high as 2 kV mm^{-1} at extremely low frequency. Furthermore, thanks to the insensitivity of the sensors to fields perpendicular to the z-axis of the crystal, three dimensional full-vectorial measurements can be readily obtained by mounting three sensors in orthogonal directions. These features make the devices suitable for the use in high electric field and harsh conditions, e.g. power stations and transmission lines, without any danger for the operator.

6.2 Future Outlook

6.2.1 Optical modulator

As a future development, $LiNbO_3$ modulators can use micro-structuring to cope with the challenges of the new modulation formats like DQPSK and SSB that are directed to an increase of spectral efficiency in the modulation which is particularly important when moving to tenths of Gb/s networks. New modulators structures like ridge, thin plate (Fig.6.1) and domain inverted can be effective while their fabrication processes (etching, polishing, bonding and electric field poling) are easily scalable to large mass production. Moreover, the integration of new materials, e.g. new polymers as buffered layers, could further reduce fabrication costs even more as they only require spin coating process to be deposited instead of conventional deposition process (e-beam and sputtering deposition).

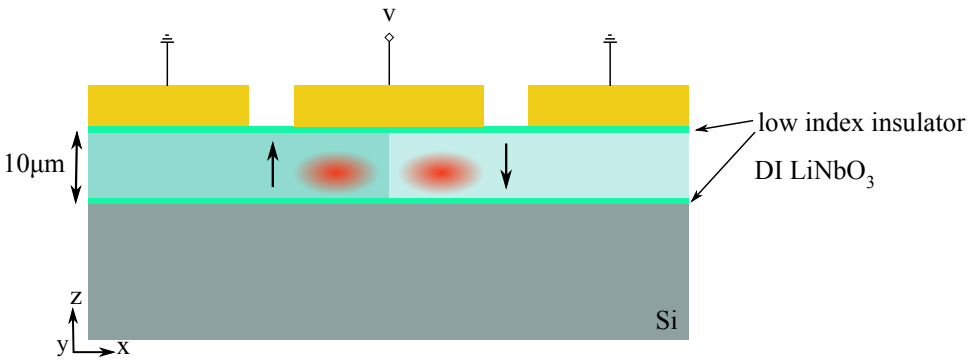

Figure 6.1: Thin plate DI bonded $LiNbO_3$ modulator. The modulator is bonded on top of a Si substrate. This configuration could be easily integrated with tunable laser and electronics thus reducing overall set-up costs.

6.2.2 Optical sensor

The first step, in order to advance with respect to the work presented in the thesis, should be field testing of the devices developed so far. Laboratory test are not sufficient to ensure the successful application of these devices in the environment where they are to be employed. Most importantly, long term stability and environmental test need to be performed in order to take into account the effects of possible space charged environment and humidity. The temperature stability of the sensor should also be tested. Temperature compensation of Lithium Niobate is a real challenge and a temperature compensation system for the device might be necessary. The detection system needs also be improved. An improvement can be achieved by intensity modulating the laser source, for example using a mechanical chopper or direct modulation of the laser diode current, and the subtraction scheme in conjunction with a lock-in amplifier. Further $LiNbO_3$ thinning and the use of a different material substrate could allow increasing the sensitivity even further, to fulfill other specific application requirements.

Bibliography

[1] G. Epps, "System power challenges," Tech. Rep., CISCO, 2006.

[2] Lightwave Venture/OIDA, "http://www.oida.org/," Tech. Rep.

[3] "http://www.creol.ucf.edu," Tech. Rep.

[4] D. Janner, D. Tulli, M. Garcia Granda, and V. Pruneri, "Micro-structured integrated electro-optic $LiNbO_3$ modulators," *Laser & Photon. Rev.*, vol. 3, pp. 301–313, 2009.

[5] C.Y.J. Ying, A.C. Muir, Valdivia C.E., H. Steigerwald, C. L. Sones, R.W. Eason, E. Soergel, and S. Mailis, "Light-mediated ferroelectric domain engineering and micro-structuring of lithium niobate crystals," *Laser & Photon. Rev.*, 2011.

[6] B. T. Matthias and J.P. Remaika, ," *Phys. Rev.*, vol. 76, pp. 1886–1887, 1948.

[7] K. K. Wong, *Properties of Lithium Niobate*, INSPEC, London, 2002.

[8] *http://www.physics.rutgers.edu/∼karin/601*.

[9] Inc. Crystal Technology, "Lithium niobate optical crystals," Tech. Rep.

[10] M. Fujimura and T. Suhara, *Waveguide Nonlinear Optic Devices*, Springer, 2003.

[11] A. Yariv and P. Yeh, *Optical Waves in Crystals*, Wiley, 1984.

[12] T. Tamir, *Guided-Wave Optoelectronics*, Springer-Verlag, 1990.

[13] J. R. Carruthers, I. P. Kaminow, and L. W. Stulz, "Diffusion kinetics and optical waveguiding properties of outdiffused layers in lithium niobate and lithium tantalate," *Applied Optics*, vol. 13, pp. 2333–2342, 1974.

[14] R. V. Schmidt and I. P. Kaminow, "Metal-diffused optical waveguides in $LiNbO_3$," *Appl. Phys. Lett.*, vol. 25, pp. 458–460, 1974.

[15] J.L. Jackel, C.E. Rice, and J.J. Veselka, "Proton exchange for high index waveguides in $LiNbO_3$," *Appl. Phys. Lett.*, vol. 41, pp. 607–608, 1982.

[16] Y. Kondo, S. Miyaguchi, A. Onoe, and Y. Fujii, "Quantitatively measured photorefractive sensititvity of proton exchanged lithium niobate, proton exchanged magnesium oxide doped lithium niobate, and ion exchaned potassium titanyl phosphate waveguides," *Appl. Opt.*, vol. 33, pp. 3348–3352, 1994.

[17] A. Loni, *An experimental study of proton exchanged lithium niobate optical waveguides*, Ph.D. thesis, Univ. of Glasgow, 1987.

[18] E. Y. B. Pun, "Proton exchange technology for integrated optics application," *Integrated Optics and Optoelectronics*, vol. CR45, pp. 44–70.

[19] M. Lawrence, "Lithium niobate integrated optics," *Rep. Prog. Phys.*, vol. 56, pp. 363–429, 1993.

[20] J.L. Jackel, C.E. Rice, and J. J. Veselka, "Compositional control in proton exchanged $LiNbO_3$," *Electron. Lett.*, vol. 19, pp. 387–388, 1983.

[21] V. A. Fedorov and Yu. N. Korkishko, "Structural phase diagram of $H_xLi_1 - xNbO_3$ waveguides: The correlation between optical and structural properties," *IEEE J. Selected Qquantum Electronics*, vol. 2, pp. 2, 1996.

[22] D Castaldini, *Study, fabrication and characterization of segmented waveguides for advanced photonic components on Lithium Niobate*, Ph.D. thesis, Università di Bologna, 2006.

[23] S.T. Vohra and A.R. Mickelson, "Diffusion characteristic and waveguiding properties of proton exchanged and annealed $LiNbO_3$ channels waveguides," *J. Appl. Phys.*, vol. 66, pp. 5161–5174, 1989.

[24] M. L. Bortz and M. M. Fejer, "Annealed proton-exchanged $LiNbO_3$ waveguides," *Opt. Lett.*, vol. 16, pp. 23, 91.

[25] P. G. Suchoski, T. K. Findakly, and F. J. Leonberger, "Stable low-loss protonexchanged $LiNbO_3$ waveguide devices with no electro-optic degradation," *Optics Letters*, vol. 13, pp. 1050–1052, 1988.

[26] Yu. N. Korkishko and V. A. Fedorov, "Dependences of the refractive indices on the proton concentration in H:$LiNbO_3$ waveguides," *Tech. Phys.*, vol. 44, pp. 307–315, 1999.

[27] A. Loni, G. Hay, and R. M. De La Rue, "Proton-Exchanged $LiNbO_3$ Waveguides: The Effects of Post-Exchange Annealing and Buffered Melts as Determined by Infrared Spectroscopy, Optical Waveguide Measurements, and Hydrogen Isotopic Exchange Reactions," *Journal of Lightwave Technology*, vol. 7, pp. 911–919, 1989.

[28] Yu. N. Korkishko and V. A. Fedorov, *Ion exchange in single crystals for integrated optics and optoelectronics*, Cambridge Int. Sci. Pub., 1999.

[29] I.V. Il'ichev, A.S. Kozlov, P.V. Gaenko, and A.V. Shamrai, "Optimisation of the proton-exchange technology for fabricating channel waveguides in lithium niobate crystals," *Quantum Electronics*, vol. 39, pp. 98–104, 2009.

[30] J. M. M.M. de Almeida, "Design methology of annealed H+ waveguides in ferroelectric $LiNbO_3$," *Optical Engineering*, vol. 46, pp. 064601, 2007.

[31] S. T. Vohra and A. R. Mickelson, "The effects of finite melt volume on proton exchanged lithium niobate," *Journal of Lightwave Technology*, vol. 6, pp. 1848–1853, 1988.

[32] R. V. Roussev, *OPTICAL-FREQUENCY MIXERS IN PERIODICALLY POLED LITHIUM NIOBATE: MATERIALS, MODELING AND CHARACTERIZATION*, Ph.D. thesis, STANFORD UNIVERSITY, 2006.

[33] R. Ulrich and R. Torge, "Measurement of Thin Film Parameters with a Prism Coupler," *Applied Optics*, vol. 12, pp. 2901–2908, 1973.

[34] J. M. White and P. F. Heidrich, "Optical waveguide refractive index profiles determined from measurement of mode indices: a simple analysis," *APPLIED OPTICS*, vol. 15, pp. 151–155, 1976.

[35] K. S. Chiang, "Construction of Refractive-Index Profiles of Planar Dielectric Waveguides from the Distribution of Effective Indexes," *Journal of Lightwave Technology*, vol. LT-3, pp. 385–391, 1985.

[36] J. M. Zavada, H.C. Casey, C.H. Chen, and A. Loni, "Correlation of refractive index profiles in annealed proton exchanged $LiNbO_3$ waveguides," *Appl. Phys. Lett.*, vol. 62, pp. 2769–2771, 1993.

[37] M. Yamada and K. Kishima, ," *Electronics Letters 27*, vol. 10, pp. 828–829, 1991.

[38] Y. Glickman, E. Winebrand, A. Arie, and G. Rosenman, ," *Applied Physics Letters*, vol. 88(1), pp. 011103, 2006.

[39] M. Yamada, N. Nada, M. Saitoh, and Watanabe K., "First-order quasi-phase matched $LiNbO_3$ waveguide periodically poled by applying an external field for efficient blue second-harmonic generation," *Applied Physics Letters*, vol. 62(5), pp. 435–436, 1993.

[40] L. E. Myers, R.C. Eckardt, M.M. Fejer, R. L. Byer, W. R. Bosenberg, and J.W. Pierce, ," *J. Opt. Soc. Am. B*, vol. 12(11), pp. 2102–2116, 1995.

[41] G. Rosenman, P. Urenski, A. Agronin, Y. Rosenwaks, and M. Molotskii, ," *Applied Physics Letters*, vol. 82(1), pp. 103–105, 2003.

[42] J Dziuban, *Bonding in Microsystem Technology*, Springer, 2006.

[43] H Takagi, R Maeda, N Hosoda, and T Suga, "Room-temperature bonding of lithium niobate and silicon wafers by argon-beam surface activation.," *Appl. Phys. Lett.*, vol. 74, pp. 2387, 1999.

[44] M Howlader, T Suga, and M Kim, "Room temperature bonding of silicon and lithium niobate," *Appl. Phys. Lett.*, vol. 89, pp. 031914, 2006.

[45] H Takagi, R Maeda, and T Suga, "Room-temperature wafer bonding of Si to $LiNbO_3$, $LiTaO_3$ and $Gd_3Ga_5O_{12}$ by Ar-beam surface activation," *J. Micromech. Microeng.*, vol. 11, pp. 348–352, 2001.

[46] A Plöbl and G Kräuter, *Materials Science and Engineering*, 1999.

[47] A. C. Muir, S. Mailis, and R. W. Eason, "Ultraviolet laser-induced submicron spatially resolved superhydrophilicityon single crystal lithium niobate surfaces," *J. Appl. Phys.*, vol. 101, pp. 104916, 2007.

[48] P. De Gennes, "Wetting:statistics and dynamics," *Rev. Mod. Phys.*, vol. 57, pp. 3, 1985.

[49] *http://www.fcc.gov/oet/tutorial/ftth tutorial-8-7-03.ppt*.

[50] E. L. Wooten, K. M. Kissa, A. Yi-Yan, E. J. Murphy, D. A. Lafaw, P. F. Hallemeier, D. Maack, D.V. Attanasio, D. J. Fritz, G. J. McBrien, and D. E. Bossi, ," *IEEE J. of Select. Topics in Quant. Elec.*, vol. 6 (1), pp. 69–82, 2000.

[51] Internal survey Tech. rep., *Market trends for digital modulators*, 2007.

[52] R.C. Alferness, "Waveguide electro-optic modulators," *Microwave Theory and Techniques*, vol. 82, pp. 1121–1137, 1982.

[53] K. Aoki, J. Kondo, A. Kondo, T. Ejiri, T. Mori, Y. Mizuno, M. Imaeda, O. Mitomi, and M. Minakat, "Single-drive x-cut thin-sheet $LiNbO_3$ optical modulator with chirp adjusted using asymmetric cpw electrode," *Journal of Lightwave Technology*, vol. 24, pp. 2233–7, 1982.

[54] M. Garcia Granda and H. Hu, ," in *OptoEL MOI-13*, 2007.

[55] V. Pruneri, R. Koch, P.G. Kazansky, W.A. Clarkson, P. S. J. Russell, and D. C. Hanna, ," *Opt. Lett.*, vol. 20(23), pp. 2375, 1995.

[56] J.H. Schaffner, ," *US 5278924*, 1994.

[57] Y. Lu, M. Xiao, and G. J. Salamo, "Wide-bandwidth high-frequency electro-optic modulator based on periodically poled $LiNbO_3$," *Appl. Phys. Lett.*, vol. 78, pp. 1338–43, 2001.

[58] N. Courjal, H. Porte, J. Hauden, P. Mollier, and N. Grossard, "Modeling and optimization of low chirp $LiNbO_3$ Mach-Zehnder modulators with an inverted ferroelectric domain section," *Journal of Lightwave Technology*, vol. 22, pp. 1338–43, 2004.

[59] F. Lucchi, M. Belmonte, S. Balsamo, M. Villa, S Giurgola, P. Vergani, and V. Pruneri, "Very low voltage single drive domain inverted $LiNbO_3$ integrated electro-optic modulator," *Opt. Express*, vol. 15, pp. 10739–43, 2007.

[60] William. S. C. Chang, Ed., *RF Photonic Technology in Optical Fiber Links*, Cambridge, 2002.

[61] P.P. Karmel, G. D. Colef, and R. L. Camisa, *Introduction to Electromagnetic and Microwave Engineering.*, Wiley-Interscience, 1998.

[62] K. Noguchi, H. Miyazawa, and O. Mitomi, "Frequency-dependent propagation characteristics of coplanar waveguide electrode on 100 ghz Ti:$LiNbO_3$ optical modulator," *Electron. Lett.*, vol. 34, pp. 19980284, 1998.

[63] K.C. Gupta, R. Garg, I. Bahl, and P. Bhartia, *Microstrip Lines and Slotlines*, Artech House, 1996.

[64] B M. A. Rahman and S. Haxha, "Optimization of microwave properties for ultrahigh-speed etched and unetched lithium niobate electrooptic modulators," *Journal of Lightwave Technology*, vol. 20, pp. 1856–1862, 2002.

[65] O. Mitomi, K. Noguchi, and H. Miyazawa, "Design of ultra-broad-band $LiNbO_3$ optical modulators with ridge structure," *IEEE Transactions on Microwave Theory and Techniques*, vol. 43, pp. 2203–2207, 1995.

[66] N. Anwar, S. S. A. Obaya, S. Haxha, C. Themistos, B M. A. Rahman, and K. T. V. Grattan, "The effect of fabrication parameters on a ridge Mach-Zehnder interferometric (MZI) modulator," *Journal of Lightwave Technology*, vol. 20, pp. 826–33, 2002.

[67] W. K. Burns, M. M. Howerton, R. P. Moeller, R. Krahenbuhl, R.W. McElhanon, and A. S. Greenblatt, "Modeling of broad-band

traveling-wave optical intensity modulators," *Journal of Lightwave Technology*, vol. 17, pp. 2551–2555, 1999.

[68] M. M. Howerton, R.P. Moeller, A.S. Greenblatt, and R. Krahenbuhl, "Fully packaged, broad-band $LiNbO_3$ modulator with low drive voltage," *IEEE Photonics Technology Letters*, vol. 12, pp. 792–794, 2000.

[69] K. Aoki, A. Kondo, T. Ejiri, T. Mori, Y. Mizuno, M. Imaeda, O. Mitomi, and M. Minakata, "Single-drive x-cut thin sheet $LiNbO_3$ optical modulator with chirp adjusted using asymmetric cpw electrode," *Journal of Lightwave Technology*, vol. 24, pp. 2233–2237, 2006.

[70] K. Aoki, J. Kondo, Y. Iwata, A. Hamajima, T. Ejiri, O. Mitomi, and M. Minakata, "High-speed x-cut thin sheet $LiNbO_3$ optical modulator with folded structure," *Journal of Lightwave Technology*, vol. 25, pp. 1805–1810, 2007.

[71] T. Gorman and S. Haxha, "Design optimization of z-cut lithium niobate electrooptic modulator with profiled metal electrodes and waveguides," *Journal of Lightwave Technology*, vol. 25, pp. 3722–3729, 2007.

[72] M. Koshiba, Y. Tsuji, and M. Nishio, "Finite-element modeling of broad-band traveling-wave optical modulators," *Journal of Microwave Theo. Trans.*, vol. 47, pp. 1627–1633, 1999.

[73] S. Haxha, B M. A. Rahman, and K. T. V. Grattan, "Bandwidth estimation for ultra-high-speed lithium niobate modulator," *Appl. Opt.*, vol. 15, pp. 2674–2682, 2003.

[74] P. Rabiei and W. H. Steier, ," *Appl.Phys. Lett.*, vol. 86, pp. 161115, 2005.

[75] M. Doi, N. Hashimoto, T. Hasegawa, T. Tanaka, and K. Tanaka, "40 gb/s low-drive-voltage $LiNbO_3$ optical modulator for DQPSK

modulation format," in *Proceedings of the Conference on Optical Fiber Communication and the National Fiber Optic Engineers Conference OFC/NFOEC*, 2007.

[76] T. Kawanishi, T. Sakamoto, T. Miyazaki, M. Izutsu, K. Higuma, and J. Ichikawa, "80 Gb/s DQPSK modulator," *Proceedings of the Conference on Optical Fiber Communication and the National Fiber Optic Engineers Conference OFC/NFOEC 2007*, pp. 1–3, 2007.

[77] C. T. Lin, C. F. Peng, P. C. Peng, J. Chen, W. R. Peng, B. S. Chiou, and S. Chi, "Simultaneous modulation and transmission of ftth baseband and radio signals on a single wavelength," in *Proceedings of the Conference on Optical Fiber Communication and the National Fiber Optic Engineers Conference OFC/NFOEC*, 2007.

[78] S. Shimotsu, S. Oikawa, T. Saitou, N. Mitsugi, K. Kubodera, and M. Kawanishi, T.and Isutsu, ," *IEEE Photonics Technol. Lett.*, vol. 13, pp. 364–366, 2001.

[79] H. Murata, D. Nakata, K. Ono, and Y. Okamura, "Electrooptic single-sideband modulator using resonant electrodes and polarization-reversed structure," in *Proceedings of the (CLEO) Lasers and Electro-Optics Conference on, Baltimore*, 2005.

[80] H. Murata, M. Anjiki, and Y. Okamura, "Optical suppressed-carrier single side-band modulator-optical frequency shifter utilizing three-branch waveguide interferometer and polarization-reversed structure," in *Proceedings of the 36th European Microwave Conference, Manchester*, 2006.

[81] *http://www.jdsu.com/products/optical-communications/products/tunable-transmission-modules/transpondertunable-cl-band-10gbs-msa-7100-series.html.*

[82] G.A. Massey, D.C. Erickson, and R.A. Kaldec, "Electromagnetic field components: Their measurement using linear electrooptic and magnetooptic effects," *Appl. Opt.*, vol. 14, pp. 2712–2719, 1975.

[83] A.J. Rogers, "Optical technique for measurement of current at high voltage," 1973, vol. 120, pp. 261–267.

[84] R.E. Hebner, R.A. Malewsky, and E.C. Cassidy, Eds., *Optical Methods of Electrical Measurements at high Voltage Levels*, vol. 65. Proc.IEEE, 1976.

[85] Y. Hamasaki, H. Gotoh, M. Katoh, and S. Takeuchi, "Opsef: an optical sensor for measurement of high electric field intensity," *Electron. Lett.*, vol. 16, pp. 406–407, 1980.

[86] Y. Kuhara, Y. Hamasaki, A. Kawakami, Y. Murakami, M. Tatsumi, H. Takimoto, K. Tada, and T. Mitsui, "BSO/fibre optic voltmeter with excellent temperature stability," *Electron. Lett.*, vol. 18, pp. 1055–1056, 1982.

[87] N.A.F. Jaeger and L. Young, "High voltage sensor employing an integrated optic mach-zehnder interferometer in conjuction with a capacitive divider," *Journal of Lightwave Technology*, vol. LT-7, pp. 229–235, 1989.

[88] D.J. Smith, H.W. Dommel, and L. Young, "Integrated optic voltage sensor," *Sci. Council British Columbia, Canada, Grant. Rep.*, 1983.

[89] F. Cecelja, M. Bordovsky, and W. Balachandran, "Lithium niobate sensor for measurement of dc electric fields," *IEEE Trans. on Instr. and Measur.*, vol. 50, pp. 465–469, 2001.

[90] T.H. Lee, F.T. Hwang, W.T. Shay, and C. T. Lee, "Electromagnetic field sensor using mach-zehnder waveguide modulator," *Microwave and Optical Technology Letters*, vol. 48, pp. 1897–1899, 2006.

[91] Garzarella, "Optical electro-optic sensor configuration for phase noise limited, remote field sensong applications," *Appl . Phys. Lett.*, vol. 94, pp. 221113, 2009.

[92] G. Gaborit and L. Duvilaret, ," Grenoble, 2005, ECIO.

[93] C.H. Bulmer, "Sensitive, highly linear lithium niobate interferometers for electromagnetic field sensing," *Appl. Phys. Lett.*, vol. 53, pp. 2368–2370, 1988.

[94] N. Kuwabara and K. Tajima, "Development and analysis of electric field sensor using $LiNbO_3$ optical modulator," *IEEE Trans. EMC*, vol. 34, pp. 391–396, 1992.

[95] D.H. Nagshi, J.T. Boyd, H.E. Jackson, S. Sriram, A. Kingsley, and J. Latess, "An integrated photonic mach-zehnder interferometer with no electrodes for sensing electric fields," *Journal of Lightwave Technology*, vol. 12, pp. 1092–1098, 1994.

[96] S. Sriram and A. Kingsley, "Sensitivity enhancements to photonic electric field sensor," *SRICO*.

[97] P. Chavez, F. Rahmatian, and N. Jaeger, "230kv optical voltage transducer using distributed electric field sensor system," *Transmission and Distribution Conference and Exposition, IEEE/PES*, 2001.

[98] D. Runde, S. Brunken, C.E. Rüter, and D. Kip, "Integrated optical electric field sensor based on a bragg grating in lithium niobate," *Appl . Phys. B*, pp. 91–95, 2007.

[99] A. Neyer and W. Sohler, ""high speed cutoff modulator using a Ti-Diffused $LiNbO_3$ channel waveguide," *Appl . Phys. Lett.*, vol. 35, pp. 256–258, 1979.

[100] P.R. Ashley and W.S. Chang, "Improved mode extinction modulator using a Ti in-diffused $LiNbO_3$ channel waveguide," *Appl . Phys. Lett.*, vol. 45, pp. 840–842, 1984.

[101] R. Chen and C.S. Tsai, "Thermally annealed single-mode proton-exchanged channel waveguide cutoff modulator," *Opt. Lett.*, vol. 11, pp. 546–548, 1986.

[102] S-S Lee, M-C Oh, S-Y Shin, and K-H Keh, "Integrated optical voltage sensor using a z-cut $LiNbO_3$ cutoff modulator," *Phot. Tech. Lett.*, vol. 5, pp. 9, 1993.

[103] M. Bordovsky, *Electro-optic electric field sensor for DC and extra-low-frequency measurement*, Ph.D. thesis, Department of Manufacturing and Engineering Systems, Brunel University, West London, 1998.

[104] T. Volk and M. Wöhlecke, *Lithium Niobate*, Springer Series in Material Science, 2008.

[105] D. Tulli, D. Janner, M. Garcia Granda, R. Ricken, and V. Pruneri, "Electrode-free optical sensor for high voltage using a domain-inverted $LiNbO_3$ waveguide near cut-off," *Appl . Phys. B*, vol. 103, pp. 399–403, 2011.

[106] A. Yariv, *Introduction to Optical Electronics*, Rinehart and Winston, 1971.

[107] D. Tulli, D. Janner, and V. Pruneri, "Room temperature direct bonding of $LiNbO_3$ crystal layers and its application to high-voltage optical sensing," *J. Micromech. Microeng.*, vol. 21, pp. 085025, 2011.